Experiments and Monte Carlo Analysis for the Optical Properties of the Scintillator in SNO+

by

Xu Liu

A thesis submitted to the
Department of Physics, Engineering Physics and Astronomy
in conformity with the requirements for
the degree of Master of Science

Queen's University
Kingston, Ontario, Canada
September 2010

Abstract

The SNO+ experiment will be the SNO detector filled with a neodymium-loaded liquid scintillator instead of heavy water. SNO+ will be used to detect neutrinos of much lower energy. Also, SNO+ will conduct a search for neutrinoless double beta decay with ^{150}Nd. The Nd-loaded scintillator in SNO+ will be made from linear alkylbenzene (LAB). Both the LAB solvent and the Nd loading are new developments. The optical properties of this scintillator and information about radioactive backgrounds should be studied.

A calibration source known as the scintillator bucket was deployed in the water-filled SNO detector in order to study some optical properties of Nd-loaded scintillator, raw LAB scintillator and distilled LAB scintillator. Using a neutron source attached to the bucket to produce events with known energy, with a model of the scintillator bucket simulated by an analysis tool called RAT, the light yield of the scintillator could be determined by comparing data measurements with simulations. This allowed the light yield, one of the main optical properties of the scintillator, to be measured and that value to be corrected in the Monte Carlo.

The bucket was deployed both at the centre of the detector and at the bottom. After subtracting backgrounds from radon introduced in the scintillator during preparation and filling, constraints on the amount of ^{210}Po were obtained. Estimates on

the ^{40}K content of the Nd-loaded scintillator were obtained by analyzing the radon-subtracted background spectra. By comparing the background spectra with the bucket deployed at the bottom of the acrylic vessel with spectra from the bucket at the centre, it was possible to estimate the ^{40}K content of the acrylic vessel.

Acknowledgments

First, I would like to express the utmost gratitude to my supervisor, Dr. Mark Chen of the Department of Physics at Queens University, for his support, guidance and friendship. Many thanks to him for giving me the opportunity to finish the degree. I appreciate his patience and carefulness for both my research and thesis. His expertise in this area provided me with a wealth of knowledge and precious experiences.

I would also like to appreciate to Dr. Stephane Courteau for his help and friendship. Thanks to Usman Mushtaq, the student advisor of SGPS and Cathy Touzel, the counselor of HCDS. Without your help, I would not finish my degree.

Thanks to Helen Mary O'Keeffe, whose assistance, expertise in the research and encouragement help me a lot. Thanks to Bei Cai for your encouragement and the help. Also many thanks to Alex Wright, Jeanne Wilson Hawke, Christine Kraus and everyone in SNO group for your assistance and friendship of not only my work but also my life in Queen's University. Thank you so much for making my life here so memorable.

Table of Contents

List of Tables

List of Figures

Chapter 1

Introduction

1.1 Neutrino Physics

Neutrino physics is currently an interesting subject because of recent discoveries of neutrino oscillations and neutrino mass. In the Standard Model of elementary particle physics, neutrinos were assumed to have zero mass. But the observations of neutrino oscillations show the existence of small neutrino masses. Thus, a study of neutrino physics is essential for advancing beyond the Standard Model of particle physics.

Neutrinos were first postulated by Wolfgang Pauli in 1930 to preserve conservation of energy in beta decay. Neutrinos were first detected in 1956 by Clyde Cowan and Frederick Reines [1] at the Savannah River nuclear power plant. They used a detector containing cadmium chloride and neutrinos were detected via the inverse beta decay reaction. Neutrinos which travel at almost the speed of light, have no electric charge. There are three flavours of neutrinos corresponding to the three different flavours of charged leptons: electron neutrinos, muon neutrinos and tau neutrinos. If neutrinos have mass, it is possible for them to convert from one flavour to another by a process

called neutrino oscillation.

1.2 Neutrino Oscillation

Neutrino oscillations were first proposed by Gribov and Pontecorvo [2]. They are caused by a mismatch between the mass eigenstates of ν_1, ν_2, and ν_3 and flavour eigenstates of ν_e, ν_μ and ν_τ. The relationship between the mass and flavour eigenstates is

$$|\nu_i >= \sum_{\alpha}^{i} U_{\alpha i} |\nu_\alpha > \tag{1.1}$$

where $|\nu_i >$ is a mass eigenstate (i = 1, 2, 3) and $|\nu_\alpha >$ is a flavour eigenstates ($\alpha = e, \mu, \tau$). $U_{\alpha i}$ is The PMNS matrix $U_{\alpha i}$ can be parameterized as shown below [3],

$$\begin{aligned}
\hat{U} &\equiv \begin{pmatrix} U_{e1} & U_{e2} & U_{e3} \\ U_{\mu 1} & U_{\mu 2} & U_{\mu 3} \\ U_{\tau 1} & U_{\tau 2} & U_{\tau 3} \end{pmatrix} \\
&= \begin{pmatrix} 1 & 0 & 0 \\ 0 & c_{23} & s_{23} \\ 0 & -s_{23} & c_{23} \end{pmatrix} \times \begin{pmatrix} c_{13} & 0 & s_{13}e^{-i\delta} \\ 0 & 1 & 0 \\ -s_{13}e^{i\delta} & 0 & c_{13} \end{pmatrix} \times \begin{pmatrix} c_{12} & s_{12} & 0 \\ -s_{12} & c_{12} & 0 \\ 0 & 0 & 1 \end{pmatrix} \\
&= \begin{pmatrix} c_{12}c_{13} & s_{12}c_{13} & s_{13}e^{-i\delta} \\ -s_{12}c_{23} - c_{12}s_{23}s_{13}e^{i\delta} & c_{12}c_{23} - s_{12}s_{23}s_{13}e^{i\delta} & s_{23}c_{13} \\ s_{12}s_{23} - c_{12}c_{23}s_{13}e^{i\delta} & -c_{12}s_{23} - s_{12}c_{23}s_{13}e^{i\delta} & c_{23}c_{13} \end{pmatrix} \begin{pmatrix} e^{\frac{i\alpha_1}{2}} & 0 & 0 \\ 0 & e^{\frac{i\alpha_2}{2}} & 0 \\ 0 & 0 & 1 \end{pmatrix}
\end{aligned} \tag{1.2}$$

where $s_{ij} \equiv \sin\theta_{ij}$ and $c_{ij} \equiv \cos\theta_{ij}$. δ is the CP-violating phase and α_1, α_2 are Majorana phases [4].

There are six neutrino oscillation parameters: three mixing angles θ_{12}, θ_{13}, θ_{23}; two independent mass-squared differences Δm^2_{12} and Δm^2_{23}, where $\Delta m^2_{ij} = m^2_i - m^2_j$; CP-violating phase δ. Majorana phases α_1, α_2 can't be measured through neutrino oscillations.

Through previous solar neutrino experiments and atmospheric neutrino experiments, four parameters have been measured and one other was constrained. SNO [5, 6] combined with KamLAND [7] have measured the values of Δm^2_{12} and θ_{12}. Atmospheric neutrino experiments combined with Super-Kamiokande [8] and long-baseline neutrino oscillation experiments such as K2K [9] and MINOS [10] have measured the absolute value of Δm^2_{32} and the value of θ_{23}. The CHOOZ reactor neutrino experiment [11] constrained the value of θ_{13}. SNO combined with KamLAND have also constrained the value of θ_{13} [12]. However, the precise values of θ_{13}, δ and the sign of Δm^2_{32} are unknown and need to be studied.

1.2.1 Atmospheric Neutrinos

The first piece of evidence for neutrino oscillations came from atmospheric neutrinos observed by Super-Kamiokande. Atmospheric neutrinos are produced by the collision of cosmic rays with atomic nuclei in the Earth's atmosphere. This collision creates a shower of hadrons with many pions in the primary interaction. These pions then decay to a neutrino and a muon which decays to an electron, an electron neutrino a muon neutrino finally. Figure 1.1 illustrates the production of atmospheric neutrinos. According to these reactions, an expected ratio of the muon neutrino flux to the electron neutrino is about 2 with an estimated uncertainty of 5% [8]. And the zenith angle distribution of the neutrinos should be symmetrical upwards and downwards.

Atmospheric neutrinos were detected by Super-Kamiokande, a large water Cherenkov detector located 1 km underground. A smaller ratio of the muon neutrinos to electron neutrinos than expected was observed. And a strong asymmetry in the shape of the zenith angle distribution for muon neutrinos was observed while no significant asymmetry for electron neutrinos. Both indicate the conversion from ν_μ to ν_τ via neutrino oscillations.

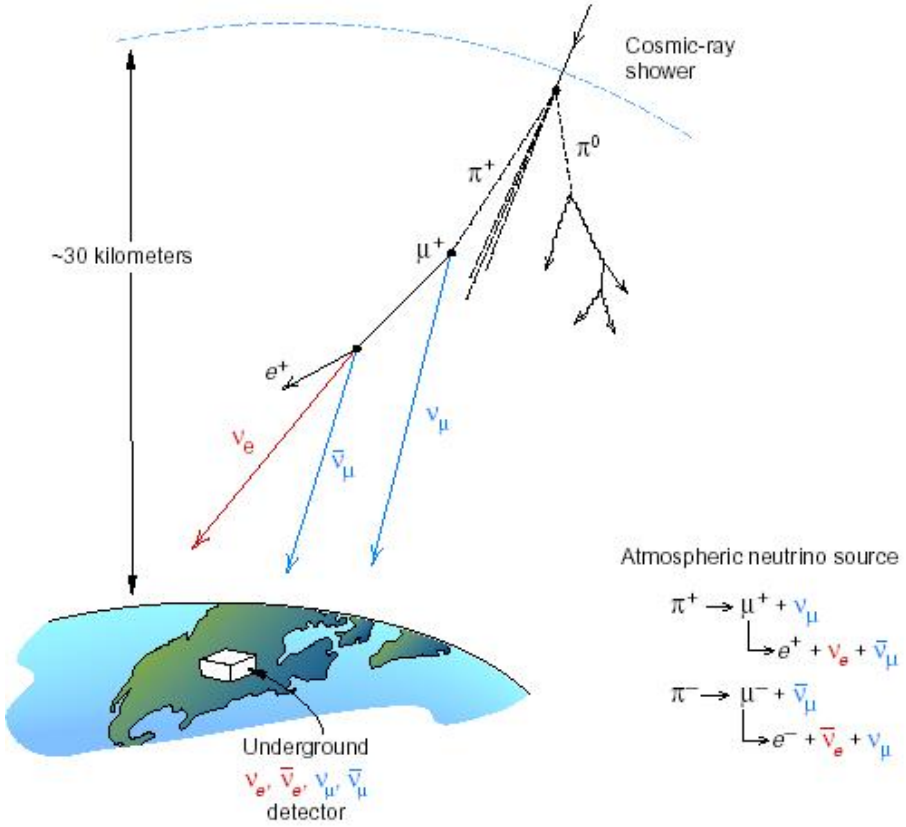

Figure 1.1: The production of atmospheric neutrinos [13]. The pion showers decay to electrons, electron neutrinos and muon neutrinos which are detected by detectors underground.

1.2.2 Solar Neutrinos

Solar neutrinos are produced by fusion reactions [14] in the Sun which create neutrinos and energy. This energy is released as light and heat, and travels from the centre of the Sun to its surface before traveling to the Earth. The neutrinos rarely interact in the Sun's interior. They propagate from the Sun's interior to the surface and then escape to the Earth at almost the speed of light. Approximately 3% of the energy radiated by the Sun is through solar neutrinos, resulting in a flux of approximately of 10^{11} neutrinos per square centimeter per second at the surface of the Earth [15]. Therefore, this large amount of solar neutrinos can be used to inspect the centre of the Sun, as well the oscillation parameters of solar neutrinos themselves.

There are two mechanisms for solar neutrino production, which fuse four protons into a helium nucleus ${}^4_2\mathrm{He}$: the CNO cycle and the p-p chain. The CNO cycle involves carbon, nitrogen and oxygen nuclei and the proton-proton chain involves nuclei of helium, lithium, beryllium and boron. These are shown in Figure 1.2.

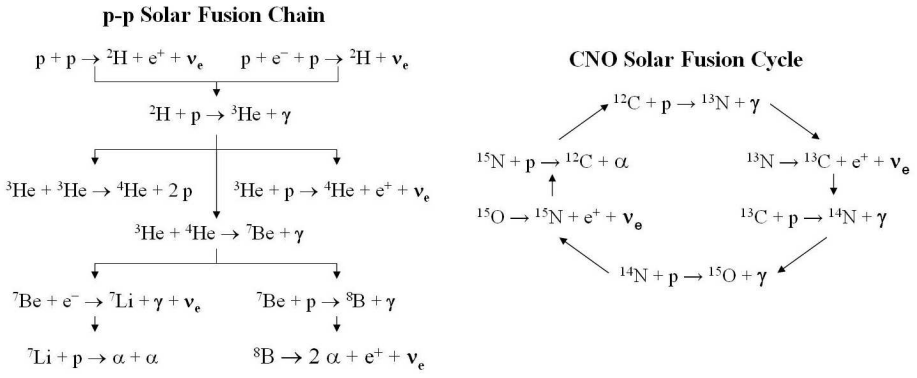

Figure 1.2: The p-p chain and CNO cycle [16]. Solar neutrinos are produces by these two mechanisms.

The first evidence of solar neutrino oscillation came from the Homestake experiment [17] and was confirmed later by Kamiokande and Super-K [18]. The measurements of solar neutrino fluxes were lower than calculated by solar models. That was the Solar Neutrino Problem (SNP). One possible solution to the SNP is neutrino oscillation. Only electron neutrinos are produced by the Sun from the two mechanisms above. If neutrino oscillations take place or the electron neutrinos change flavour, but the detector is only sensitive to electron neutrinos, the measured flux would be lower. The Sudbury Neutrino Observatory (SNO) [19] was built to be not only sensitive to electron neutrinos but also neutrinos of all flavours. The results from SNO demonstrated the existence of oscillations in solar neutrinos and solved the Solar Neutrino Problem.

1.2.3 Sudbury Neutrino Observatory

The Sudbury Neutrino Observatory (SNO) [19] is an underground science observatory focusing on non-accelerator particle physics. It is located 2039 m (∼6800 feet) underground in the Vale Inco Creighton Mine near Sudbury, Ontario, Canada. This 2 km of rock overburden is equivalent to roughly 6000 m water [19], which shields the experiment from cosmic rays. This depth offers a very low cosmic ray background for the SNO experiment. The principal scientific objective of SNO was to explore solar neutrino oscillations.

Figure 1.3: An artist's illustration of the SNO detector.

The SNO detector is a water Cherenkov detector designed to detector solar neutrinos, which is shown in Figure 1.3. Inside the barrel-shaped cavity, the detector consists of a 12 meter diameter spherical acrylic vessel filled with 1000 tonnes of heavy water in the centre and an 18 meter diameter spherical photomultiplier support structure (PSUP) surrounding the acrylic vessel. Approximately 1700 tonnes ultra pure light water shields the acrylic vessel from the PSUP and a further 5300 tonnes is between the PSUP and rock to shield from radioactive backgrounds. There are about 9500 PMTs mounted in the PSUP which face towards the centre of the acrylic vessel. The suspension ropes hold the acrylic vessel up because the density of heavy water is larger than the light water. A detailed description of the detector is given in [19].

The SNO detector is able to detect all flavours of neutrinos by using heavy water

(D_2O) [20]. All the neutrinos detected are from the decay of ^8B in the Sun. Through the interactions of neutrinos with deuterium nuclei, the total flux of electron neutrinos and the flux of all flavours of neutrinos can be measured.

The charged current (CC) reaction is sensitive to electron neutrinos only. The initial ν_e interacts with d (the deuterium nucleus), producing two p and e^-. This reaction is detected by the Cherenkov light produced by the e^-.

$$\nu_e + d \rightarrow p + p + e^- \tag{1.3}$$

The neutral current (NC) reaction is sensitive to all flavours of neutrinos,

$$\nu_x + d \rightarrow \nu_x + n + p, \tag{1.4}$$

where x is any flavour of neutrinos. This reaction is detected indirectly, via neutron capture in three ways:

$$^2H + n \rightarrow {}^3H, \qquad D_2O \quad phase \tag{1.5}$$

where NC flux and CC flux were separated by energy, radial and direction distributions;

$$^{35}Cl + n \rightarrow {}^{36}Cl, \qquad Salt(NaCl) \quad phase \tag{1.6}$$

where the energy release and efficiency are higher than the D_2O phase;

$$^3He + n \rightarrow {}^3H + p, \qquad NCD \quad phase \tag{1.7}$$

where neutrons were captured by ^{3}He proportional counters mounted in the AV so that the CC flux and NC flux can be measured in different systems.

If all the neutrinos detected by SNO are electron neutrinos, the flux of CC reaction should be the same as the flux of NC reaction. But from the measured results of the three phases, the flux of electron neutrino was approximately 30% of the total neutrino

flux. The neutrino oscillations including effects of neutrinos propagating through dense matter in the Sun [21] explain the flavour deficit observed by SNO and thus solved the Solar Neutrino Problem. Meanwhile the experimental results from SNO combined with other solar neutrino experimental results constrain neutrino oscillation parameters.

1.3 Neutrinoless Double Beta Decay

One of the most interesting questions in neutrino physics is whether neutrinos are Majorana [22] or Dirac particles. A particle is a Dirac particle if it is distinct from its own anti-particle. Most familiar particles are Dirac. A Majorana particle acts as its own anti-particle. Studying the neutrinoless double beta decay process might prove that neutrinos are Majorana particles.

Double beta decay can occur in $2\nu\beta\beta$ decay:

$$(A, Z) \rightarrow (A, Z + 2) + 2e^{-} + 2\bar{\nu}_e. \tag{1.8}$$

If neutrinos are Majorana particles, the Majorana charge conjugation nature of neutrinos will cause them to annihilate each other which results in a process of no neutrinos being emitted. This is the neutrinoless double beta decay ($0\nu\beta\beta$):

$$(A, Z) \rightarrow (A, Z + 2) + 2e^{-}. \tag{1.9}$$

which violates lepton number conversation. The $0\nu\beta\beta$ decay involves changing two neutrons into two protons with the emission of two electrons and exchanges of virtual particles such as massive Majorana neutrinos. The $0\nu\beta\beta$ decay can occur only if neutrinos are massive Majorana particles [23].

The absolute neutrino mass scale and the Majorana phases α_1, α_2 can't be obtained in the neutrino oscillation experiments. But these parameters affect the decay rate of neutrinoless double beta decay. The half-life ($T_{1/2}$) of the $0\nu\beta\beta$ decay is

$$[T^{0\nu}_{1/2}]^{-1} = G^{0\nu}|M^{0\nu}|^2 < m_{\beta\beta} >^2 \tag{1.10}$$

where $G^{0\nu}$ is the calculable phase space factor; $M^{0\nu}$ are the nuclear matrix elements; $< m_{\beta\beta} >$ is the effective Majorana neutrino mass.

$$< m_{\beta\beta} >= |\sum_i |U_{ei}|^2 m_i e^{i\alpha_i}| \tag{1.11}$$

where U_{ei} are the elements of the PMNS neutrino mixing matrix; m_i is the mass of the Majorana neutrino ν_i; α_i is the Majorana phase, i=1, 2, 3 [24].

So, the observation of the $0\nu\beta\beta$ decay can demonstrate that neutrinos are Majorana particles. The neutrinoless double beta decay only happen if neutrinos are Majorana particles and the decay rate is related to the absolute neutrino mass though the Majorana phases and unknown value of θ_{13} make this more complicated.

The signature of $0\nu\beta\beta$ decay is a peak at the Q-value of the decay while $2\nu\beta\beta$ decay have a continuous kinetic energy spectrum ranging from 0 to the Q-value of the decay. Because there might be backgrounds added to the counts of $0\nu\beta\beta$ decay peak, low radioactive backgrounds are needed. To demonstrate the peak is actually due to $0\nu\beta\beta$ decay, both the energy resolution and the radioactive backgrounds should be studied. Because of the small amount of electron pairs produced by neutrinoless double beta decay, a large scale detector for more statistics and a low radioactive background are needed.

1.4 Introduction of SNO+

To observe the neutrinoless double beta decay, the old SNO detector will be filled with a liquid scintillator instead of heavy water; the new experiment is called SNO+. That liquid scintillator is an organic liquid which produces light when it interacts with a charged particle. The amount of light produced by a liquid scintillator is much greater than the light produced by the Cherenkov process (in water). The radioactive background in the scintillator is also lower than in water. So SNO+ can be used to detect neutrinos of much lower energy than those that were detectable by SNO. The scintillator in the SNO+ experiment will use linear alkylbenzene (LAB), which has a higher light yield and long attenuation length. In addition, it is safe, inexpensive and also seems to be compatible with acrylic. Because it is a new scintillator, its optical properties need to be studied. The acrylic vessel, photomultiplier tubes (PMT), and PMT support structure (PSUP) will be inherited from SNO. Because the density of LAB is smaller than that of light water, the acrylic vessel will need to be held down by a rope net, as shown in Figure 1.4.

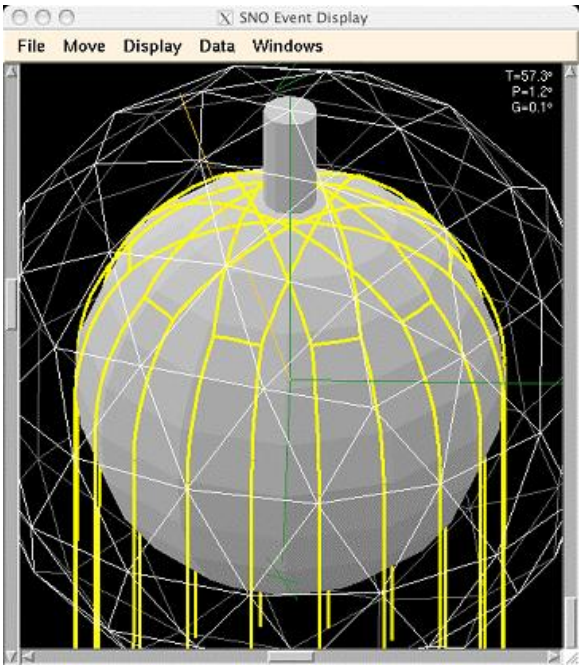

Figure 1.4: Drawing of the rope hold down net for the SNO+ [25].

To search for neutrinoless double beta decay, neodymium-150 (^{150}Nd) will be loaded into the scintillator. The natural abundance of ^{150}Nd is 5.6% which is suitable when SNO+ is filled with 780 tonnes of Nd-loaded scintillator. That means a 1% Nd-loaded scintillator would have 437 kg of ^{150}Nd. The ^{150}Nd $2\nu\beta\beta$ decay is

$$^{150}Nd \rightarrow {}^{150}Sm + 2e + 2\nu \tag{1.12}$$

where the ^{150}Nd $2\nu\beta\beta$ decay has a half-life of $(9.11 \pm 0.63) \times 10^{18}$ year [26].

The ^{150}Nd $0\nu\beta\beta$ decay is

$$^{150}Nd \rightarrow {}^{150}Sm + 2e \tag{1.13}$$

where in neutrinoless double beta decay all the decay energy is carried by the two electrons. Then, all the sum of their energies is the Q-value for the decay, which is 3.37 MeV. Figure 1.5 is a plot of the double beta decay signals and expected background

levels in SNO+.

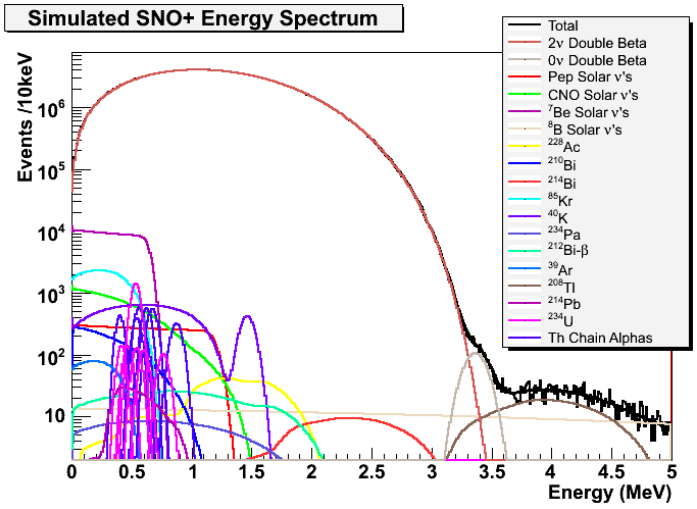

Figure 1.5: Simulated energy spectrum of SNO+ double beta decay and the radioactive background [16]. The neutrinoless double beta decay signal was calculated and plotted for a neutrino mass of 150 meV.

In Figure 1.5, the spectrum from $2\nu\beta\beta$ is the dominant rate at lower energies and the peak at the Q-value is from neutrinoless double beta decay. In this figure, the expected radioactive background is also simulated. In the concerned energy range from 3.0 MeV to 3.7 MeV, the activities of ^{214}Bi and ^{208}TI are the major radioactive backgrounds and need to be studied.

The ^{150}Nd has a high Q-value and a large atomic number which make the $0\nu\beta\beta$ decay phase space factor $G^{0\nu}$ the largest of all isotopes for $0\nu\beta\beta$ decay. The $0\nu\beta\beta$ decay rate for ^{150}Nd is proportional to the $G^{0\nu}$ so it is the fastest one of all isotopes. That is why ^{150}Nd is chosen for SNO+. Also, because SNO+ will utilize a large amount of isotope, the potential for a large number of neutrinoless double beta decay events allows for sensitivity to the effective Majorana neutrino mass to be very

good, as low as 100 meV. Nd-loaded liquid scintillator is a new scintillator. So the characterization of optical properties and backgrounds is important and need to be studied.

In addition, SNO+ can also explore other neutrino physics topics like lower energy solar neutrinos, geo-neutrinos, supernova neutrinos and reactor antineutrinos.

1.5 Organization of Thesis

Through neutrinoless double beta decay, not only neutrinos as massive Majorana particles can be demonstrated, but also the effective process is sensitive to the absolute neutrino mass scale. A liquid scintillator detector called SNO+ is being built by converting the original detector of SNO for this objective. A Nd-loaded LAB scintillator will be filled in the detector which is new. Thus, the optical properties of the scintillator and backgrounds especially for the Nd-loaded scintillator which have an effect on the sensitivity of the experiment should be studied. Simulation of the scintillator and the radioactive background in Monte Carlo can predict the sensitivity of the neutrino experiment.

The optical properties of the LAB and the Nd-loaded liquid scintillator are very important in modeling the scintillation process in Monte Carlo simulation. So in Chapter 2, a new analysis tool—RAT and how it works are described briefly. The parameters of the optical properties implemented in RAT are discussed. The radioactive backgrounds of the detector are also discussed in Chapter 2. The main backgrounds in SNO+ are from alpha, beta and gamma emissions of the ^{238}U decay chain, ^{232}Th decay chain and ^{40}K and the radioactive backgrounds can be separated into internal and external backgrounds. To investigate several important optical properties of the

scintillator and the backgrounds of the detector, a scintillator test source known as the scintillator bucket was deployed in the SNO detector. At the same time, the model of the scintillator bucket was simulated in RAT. The construction of the scintillator bucket and measurement details are described in Chapter 3 as well as the simulated model of the scintillator bucket. By comparing the data from measurements and simulations, the optical properties in simulation can be adjusted and the model can be improved, shown in Chapter 4. An attempt to better understand backgrounds for the SNO+ experiment was made by analyzing data from the scintillator bucket source; these analysis are described in Chapter 5. The last chapter will present the conclusions.

Chapter 2

Scintillator and Background

To search for neutrinoless double beta decay, a neodymium-loaded liquid scintillator will be used in the SNO+ detector. It is necessary to study optical properties like emission, absorption and light yield of the scintillator and model the optical properties to simulate the scintillation process so that the response of the SNO+ detector will be better understood. In addition, understanding radioactive backgrounds is very important. The quantity of radioactive background for the neodymium-loaded scintillator is interesting since it has not been used before. These two topics, scintillator optical properties for simulation and radioactive backgrounds, are the focus of my research work and this thesis.

2.1 Nd-Loaded Liquid Scintillator

A scintillator is a material which emits light when charged particles (ionizing radiation) pass through it and excite the material, with the subsequent de-excitation being the origin of the light emission. A liquid scintillator is typically a mixture of

an aromatic solvent (compound that contains a benzene ring) and a fluor dissolved in the solvent. The fluor should have a high quantum fluorescence yield and is added at a concentration sufficient for efficient non-radiative transfer of excitation energy from the solvent to the fluor. A secondary wavelength shifter is sometimes added to the mixture to shift the wavelength of emission to match the sensitive range of a particular photomultiplier tube (PMT) used to detect the scintillation light. If the emission spectrum from the fluor matches well the PMT spectral response, a secondary wavelength shifter is not necessary.

In SNO+, linear alkylbenzene (LAB) will be used as the solvent and diphenyloxazole (PPO) with 2 g/L concentration will be used as a fluor. LAB was selected for use in SNO+ because it is chemically mild and compatible with acrylic. Because of this, it can be used undiluted and thus has a high light yield. LAB has a high flash point (130°C) [27] and low toxicity so it is safe to use. The other important factor to consider it that it is relatively inexpensive compared to other scintillating solvents.

Neodymium can be added to liquid scintillator in the form of a carboxylate. Nd salt ($NdCl_3$) is first purified to reduce the amount of radioactive contaminants such as ^{232}Th. The purified salt is dissolved by 3,5,5-trimethylhexanoic acid (TMHA), a carboxylic acid. The Nd-TMHA solution is mixed with LAB. Liquid-liquid extraction is the transfer of the Nd-TMHA to the organic phase from the aqueous solution. This is controlled by adjusting the pH of the mixture. The organic phase separates from the water by gravity and Nd-loaded scintillator is what is found floating on top [28].

Nd-loaded LAB scintillator is new. The optical properties of this scintillator are thus not well known. Some laboratory measurements of optical properties were performed by previous students and postdocs at Queen's [16]. Most of these measured

values have been put into a Monte Carlo simulation called SNOMAN. SNOMAN was the Monte Carlo code used for the original SNO experiment. Modeling of the scintillation process and the propagation of scintillation light was added to SNOMAN by previous students. The SNO+ collaboration is moving to a new Monte Carlo package, called RAT, and scintillation optical properties and model needed to be verified in the new package.

2.1.1 RAT Construction

RAT stands for Reactor Analysis Tools though this acronym has no meaning any more since the tools it provides do not involve reactors or reactor-based neutrino experiments. RAT is a C++ code that will be used for both the Monte Carlo simulation and the event-based data analysis for the SNO+ experiment. SNOMAN, the primary analysis tool for the SNO experiment, is written in FORTRAN and for several reasons the SNO+ collaboration has decided to move over to RAT. The following is a outline of how the RAT Monte Carlo package, as it applies to SNO+.

Geometry

RAT utilizes GEANT4 (stands for GEometry ANd Tracking), a toolkit developed by CERN for the simulation of particles as well as the tracking of particles in a geometrical description of a complex particle detector. Tables and input files contain the information that RAT passes on to Geant4. The RAT database is a list of tables which stores the information for the detector. For different components of the detector, for example the liquid scintillator, acrylic vessel, PSUP, PMTs, light water and "belly plates" around the middle of the AV, parameters such as position and

dimension are specified in different *GeoFactory* files. Then the entire environment of these pieces of the detector is represented in a geometry file including the shape, position and material of each piece. They are set up to be a complete detector. Also, physical properties such as the density and composition of the materials are specified in a table in the RAT database while optical properties like the index of refraction and absorption length are specified in another table in the RAT database.

Event Producer

The event producer produces events from input files or Monte Carlo simulations. In the Monte Carlo simulation, a generator is used to specify the kind of particle, the number, energy and rate of particles generated, and the position and the time of the production. Decay events like double beta decay, energetic particles like gamma rays, electrons and neutrons, and scintillation photons can be simulated by the generator. In addition, coincidence events can be generated if more than one generator is used.

Physics Processors

After the events have been generated, they are processed by a physical processor which simulates the physical processes during the propagation of the events. There are different physical processes for different generated particles, such as the neutron diffusion, decay and capture processes, the gamma capture process, and the Cherenkov process. The one I examined in detail is the scintillation process which uses the tables of material and optical properties information in the database to simulate the absorption, emission, re-emission and scattering processes of the generated propagating particle (scintillation photon) in the scintillator.

Event Processors

Physical processes are completed when photons tracked in the simulation are detected (captured) by PMTs. Event processors then simulate the processing of real PMT data. The front-end processor identifies events which exceed a threshold that can be set for the PMTs. A trigger processor simulates the data processing trigger; it takes a sum of all the simulated PMT hits (Nhits) and determines if it exceeds a trigger condition. Then the event builder processor simulates the building of events as though this were a real event in the detector. An output processor writes the event information out to a file.

Runtime Macro

A macro file has a list of commands to control RAT during runtime. In the macro file, the geometry of the detector is applied and the database of material and optical properties are loaded. The macro file contains instructions for what events to produce; these are processed in a loop.

2.1.2 Optical Properties Implementation

In RAT, the simulation of the scintillation process is described in GLG4Scint which is inherited from GLG4sim, a package of routines added to Geant4 as a generic simulation of a liquid scintillator neutrino detector [29]. The optical properties of different scintillators are specified in a list of tables in *Optics.ratdb*. The values of an optical property are defined mostly as arrays in the table. Using the values in the table, the physical processes of emission, absorption, re-emission, scattering and quenching can be simulated.

The optical properties of the Nd-loaded scintillator have been already implemented in SNOMAN and their parameters are specified in *scintillator.dat*. It is necessary to better understand the optical properties and their simulation results in SNOMAN so that the optical properties in RAT can be implemented by converting the values from SNOMAN and then verifying that the RAT simulations produce the same results. A macro [30] is used to convert optical constants of Nd-loaded LAB from the SNOMAN format to the RAT format. The macro file is *Optics_SNOMAN_to_RAT.C* which is in the *snocave/sasquatch/dev/tools/optics/* in SNOMAN. The primary optical properties [31] to be implemented in RAT are described below.

Light Yield

Light yield, which is the number of photons emitted by the scintillator per unit of energy lost when an ionizing particle passes through, is the most important optical property. For the LAB mixed with 2 g/L PPO scintillator, the light yield was measured previously to range from 10800 to 13000 photons/MeV [31]. This was a measurement that compared the light yield from this scintillator to reference scintillators for which the light yield has a known value. Nd-loaded scintillator was observed to have a no more than 10% lower light yield than an unloaded scintillator [31]. The reason for the decreased light yield is either quenching, light absorption of Nd or a combination of both. In SNOMAN, the light yield was set to be 12000 photons/MeV for both the raw and the Nd-loaded LAB mixed with PPO. As an initial value, the light yield in RAT was also set to be 12000 photons/MeV. One aspect of my research was the measurement of the light yield using a scintillator test deployment in the SNO detector, described in the next chapters of this thesis. This work gave us an

updated value for the light yield.

PPO Concentration

In SNOMAN, the PPO concentration used in the scintillator model was 1.5 g/L (based upon the PPO concentration used in the Borexino experiment). In SNO+, the desired PPO concentration is 2.0 g/L. Thus in converting SNOMAN input values relevant to PPO to the values coded in RAT, the amounts were scaled up by 1.333.

Index of Refraction

The optical properties of all the materials were specified in *media.dat* in SNOMAN. In SNOMAN, the index of refraction is expressed in three parameters.

$$refraction = p_0 + p_1 e^{p_2 E_\gamma} \tag{2.1}$$

where $p_0 = 1.505, p_1 = 0, p_2 = 0$ for both raw LAB+PPO and Nd-loaded LAB+PPO scintillator. In RAT, the same index of refraction is used. It should be noted that a variable index of refraction versus wavelength (energy) of the photon can be implemented; the initial value used is a constant value of 1.505.

Emission

The light yield determines how many photons to simulate per MeV energy deposit in the scintillator. Those scintillation photons are assigned a wavelength from the emission spectrum of PPO. The emission spectrum of PPO and the LAB+PPO scintillator time constant are well known and were previously measured at Queen's University [32]. The scintillation photons are assigned a wavelength from an exponential distribution with time constant 5.1 ns. Figure 2.1 shows the primary emission of the

scintillator as simulated in SNOMAN, as a cumulative probability distribution.

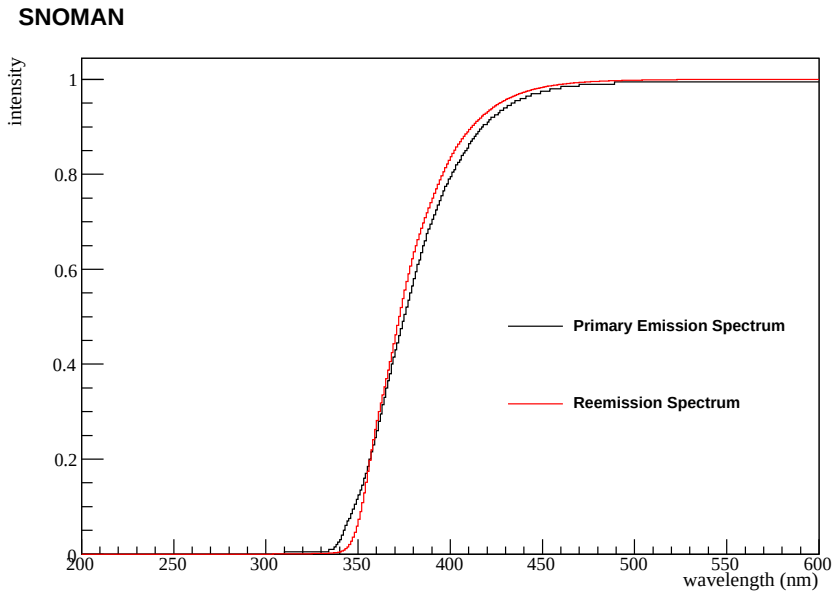

Figure 2.1: The black curve is the primary emission spectrum and the red curve is the reemission spectrum in SNOMAN. In SNOMAN, the primary emission spectrum is expressed in a table of 200 wavelengths. The x-axis shows those 200 wavelengths and the y-axis is the sequence number over the total number of 200 which is a cumulative emission intensity. The PPO reemission spectrum is expressed in a table of 401 values which is a cumulative reemission intensity(y-axis), and the x-axis is the wavelength from 200 nm to 600 nm in 1 nm steps (401 values total). The difference of the two curves is an artifact of the 400 bins selected in the reemission spectrum versus 200 bins in the primary emission spectrum, because the energy of the reemission photons are generated from the reemission spectrum which needs more precision.

In RAT, this spectrum is expressed in a table of 100 values of wavelength from 200 nm to 600 nm in 4 nm steps; however each value is the differential emission intensity at that wavelength as shown in Figure 2.2.

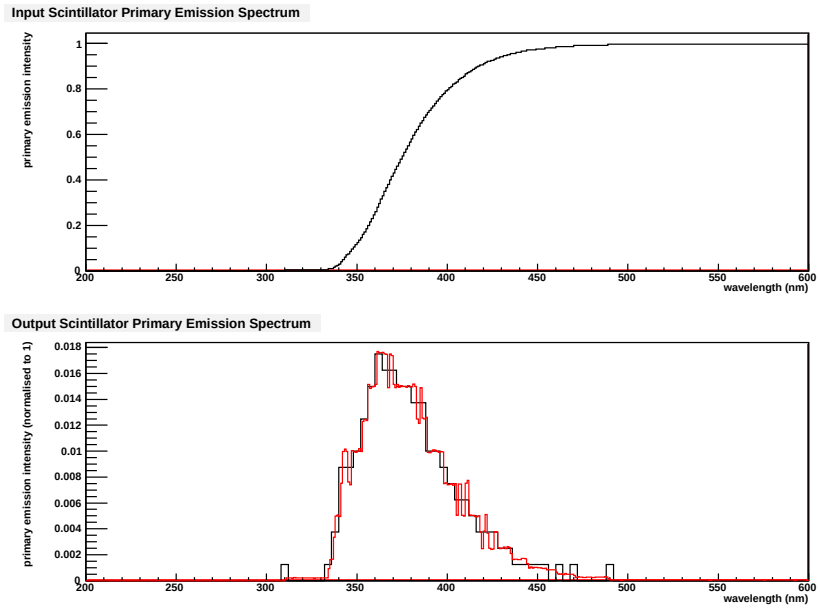

Figure 2.2: The top plot is the cumulative primary emission spectrum in SNOMAN as in Figure 2.1. The bottom plot shows the differential primary emission spectrum in RAT (black line) and the differentiated top spectrum – the value in of the N^{th} bin is the value of the N^{th} bin minus the value of the $(N-1)^{th}$ bin(red line).

Absorption

For 0.1% Nd-loaded LAB + PPO, the attenuation for three components of the scintillator was measured previously at Queen's University [32] and expressed as an absorption coefficient in SNOMAN. In the attenuation equation, $I = I_o 10^{-ax}$, a is the absorption coefficient with a unit of cm^{-1}, where x is the distance in cm and I_0 is the initial photon flux propagating in the scintillator and I is the attenuated photon flux. Figure 2.3 shows the tabulated attenuation spectrum in the SNOMAN Monte Carlo (input values come directly from the measured values). The attenuation of the Nd component of the scintillator was determined by measuring the attenuation spectrum of 0.1% Nd-loaded LAB, and then subtracting the attenuation of pure LAB [31]. For

this curve, measured attenuation in LAB or 0.1% Nd-loaded LAB was dominated by the LAB and subtraction gives large error bars. The absorption of the Nd component was thus assigned a value of 10^{-5} cm^{-1} from 200-330 nm.

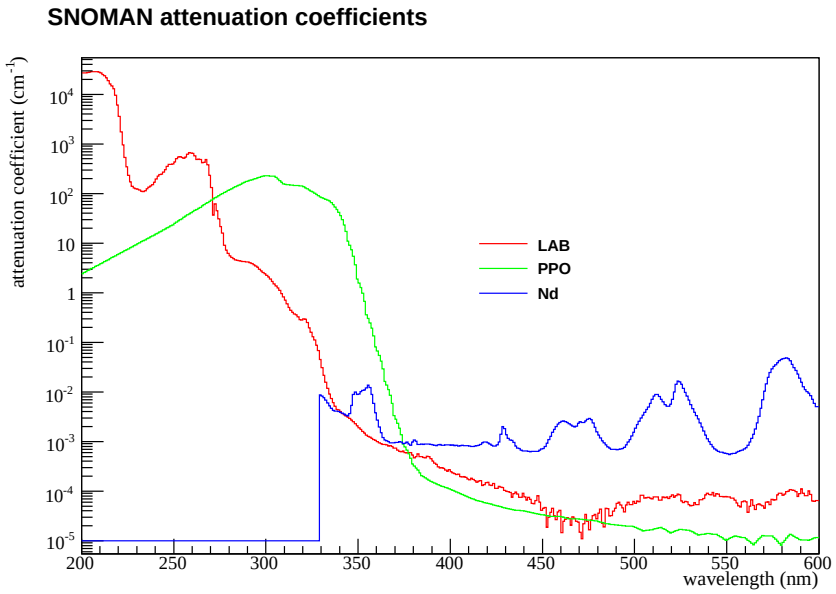

Figure 2.3: The absorption coefficient is expressed in SNOMAN by a table of 401 values which starts from the 200 nm wavelength to 600 nm wavelength in 1 nm steps. Data taken from *scintillator.dat* in SNOMAN

From the attenuation coefficient parameters of the three components, the mean free path (absorption length) of the component i, which is the distance when $I_i = I_{i,o}e^{-1}$, can be calculated using Equation 2.2.

$$A_{i,abs} = \frac{1}{a_{i,abs}R_i ln10} \tag{2.2}$$

where $a_{i,abs}$ is the absorption coefficient of component i, ln10 accounts for the base number 10 used in the attenuation equation in SNOMAN and R_i is the relative contribution of the component i (it is a scaling factor to adjust the concentration

of the components). $A_{i,abs}$ has units of cm and is converted to the default units of mm in RAT. To summarize, SNOMAN used a base 10 absorption coefficient to describe attenuation while RAT uses the 1/e absorption length, and the equation $I = I_0 e^{-x/A_{abs}}$. When photons travel a distance of 1 mm, the probability of absorption for each component is

$$P_{i,abs} = 1 - I/I_0 = 1 - e^{-1/A_{i,abs}} \tag{2.3}$$

$$A_{i,abs} = \frac{1}{ln(1 - P_{i,abs})} \tag{2.4}$$

and the total absorption length of the scintillator is

$$A_{abs} = \frac{1}{\sum_{i}^{n} \frac{1}{A_{i,abs}}} \tag{2.5}$$

where n is the number of components of the scintillator.

Rayleigh Scattering

Rayleigh scattering is the elastic scattering of the photons by molecules smaller than the wavelengths of the photons, when light travels in the liquid scintillator. The mean free path of Rayleigh scattering with a unit of mm is

$$A_{ray} = \frac{1}{ln(1 - P_{ray})} \tag{2.6}$$

where P_{ray} is the probability of Rayleigh scattering. The total extinction length is the combination of the absorption lengths with different component and the Rayleigh scattering length. As both scattering and absorption are very important, a lineal extinction coefficient is defined as a absorption coefficient plus a scattering coefficient, so the extinction length which is combined with the absorption length and the

scattering length is

$$A_{ext} = \frac{1}{\frac{1}{A_{abs}} + \frac{1}{A_{ray}}} \tag{2.7}$$

where A_{ext} is the extinction length with a unit of mm and the probability of extinction is $P_{ext} = 1 - e^{-1/A_{ext}}$.

The absorption spectrum in RAT is expressed in a table of 100 values of total extinction length with a unit of mm from the 200 nm to 600 nm wavelength. Figure 2.4 shows the mean free paths of attenuation for different components, Rayleigh scattering, and the mean free path of total extinction.

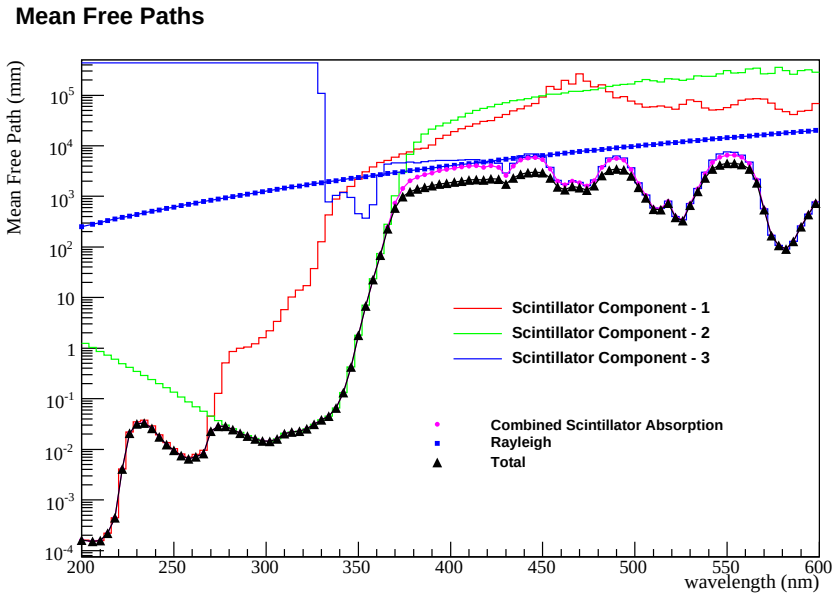

Figure 2.4: The plot shows the absorption length with a unit of mm for three scintillator components, the combined scintillator absorption length after the relative contribution correction, the Rayleigh scattering length and the total extinction length. The x axis shows 401 values which start from the 200 nm wavelength to a 600 nm wavelength in 1 nm steps.

The probability of the Rayleigh scattering is calculated in *rayint_prob.for* in SNOMAN. Equation 2.8 calculates the probability of Rayleigh scattering of a photon per unit length (cm).

$$\begin{aligned} P_{ray} &= CONFAC \times BETAT \times SCALEFAC \times (E_\gamma)^4 \\ &\quad \times (REFSQ - 1.0)^2 \times (REFSQ + 2.0)^2 \end{aligned} \tag{2.8}$$

where CONFAC is the conversion factor of the units, CONFAC = 1.53×10^{26}. SCALEFAC is the Rayleigh scattering scale factor which combined with CONFAC is just the normalization, SCALEFAC = 12.14. E_γ is the energy of the photon in MeV, $E_\gamma = hc/wavelength$ and REFSQ is the refractive index of that photon wavelength. BETAT is the isothermal compressibility of Nd-loaded scintillator, BETAT = $4.92 \times 10^{-10} N^{-1} m^2$. Factors are taken from *media.dat*.

Using this equation, the probability of the Rayleigh scattering per cm at different wavelengths can be calculated and is shown in Figure 2.5.

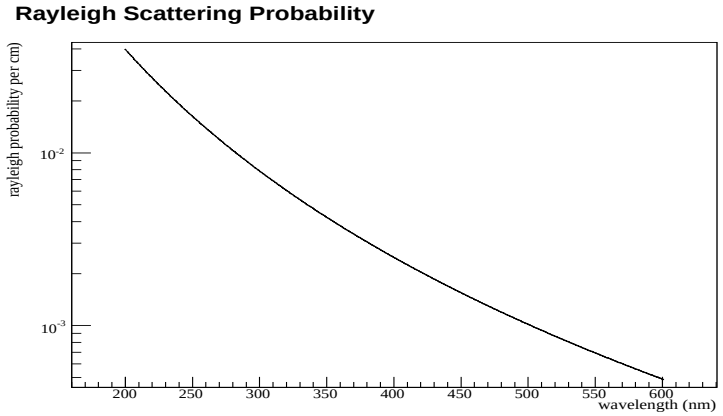

Figure 2.5: The calculated probability of the Rayleigh scattering per cm at different wavelengths. The x-axis shows 100 values of wavelengths from the 200 nm to 600 nm in 1nm steps.

In RAT, scattering is modeled by using optical scattering fractions in an array of 100 values of from 200 nm to 600 nm in 4 nm steps. The optical scattering fraction is the probability of scattering of a photon if it is "absorbed" which includes absorption, scattering and reemission.

$$P_{ext} = 1 - e^{-1/A_{ext}} \tag{2.9}$$

$$P_{opt} = \frac{P_{ray}}{P_{ext}} \tag{2.10}$$

where P_{opt} is the optical scattering fraction.

In Figure 2.6, the bottom right plot shows the fraction of optical scattering and the fraction of combined absorption which is $1 - P_{opt}$.

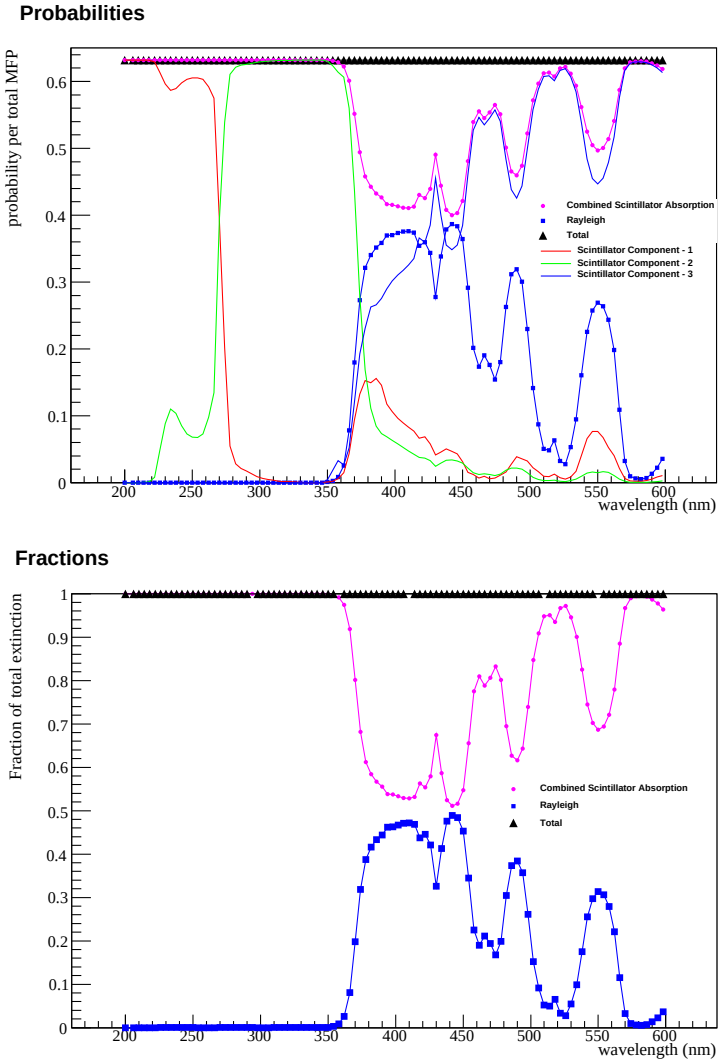

Figure 2.6: The top plot shows the probabilities of absorption for each component, the probability of the combined absorption and the probability of Rayleigh scattering. The bottom plot shows the Rayleigh scattering fraction and the total absorption fraction of the total extinction. The x-axis shows 100 values of wavelengths from the 200 nm to 600 nm in 1 nm steps.

Reemission Probability

When LAB or PPO molecules absorb a photon, the molecule can reemit it. The reemission probability is the the quantum fluorescence yield which is the fraction of times a molecule emits a photon when it de-excites. The quantum yield for PPO is known from references to be 0.8 [31]. The emission probability when LAB is excites (including the transfer efficiency for the excitation energy to PPO) was measured previously at Queen's University to be 0.59 [32]. When Nd absorbs a photon, there is zero reemission probability.

RAT models the propagation of scintillation light for the scintillator mixture as a whole. It does not know which component absorbed the photon. To model reemission, RAT requires, as a function of wavelength, the fraction that any given component absorbs a photon, when a photon is absorbed, multiplied by the remission probability (quantum fluorescence yield). The probability for photons to be absorbed by a component is

$$P_{i,abs} = \frac{\frac{1}{A_{i,abs}}}{\frac{1}{A_{abs}}} \tag{2.11}$$

The total reemission probability is the sum of reemission probabilities of each component.

$$P_{tot} = \sum_i P_{i,tot} = \sum_i P_{i,abs} P_{i,emi} \tag{2.12}$$

where P_{tot} is the total reemission probability, $P_{i,abs}$ and $P_{i,emi}$ is the absorption and reemission probability for each component.

In RAT, the reemission probability spectrum is expressed in an array of 100 values of total reemission probability from 200 nm to 600 nm wavelength in 4 nm steps, shown in Figure 2.7.

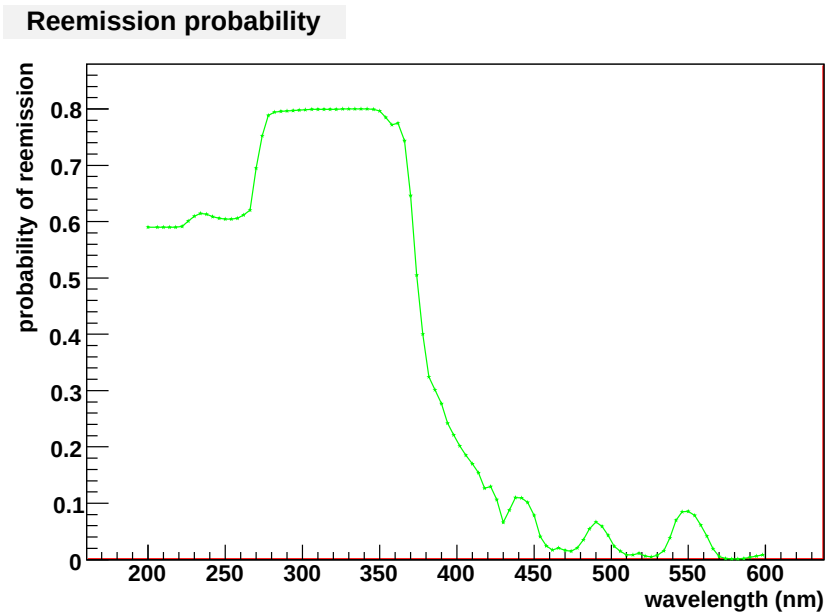

Figure 2.7: The combined reemission probability of the Nd-loaded LAB. If a photon is absorbed by the scintillator, the probability of reemission is the sum over all components of the individual probabilities (for each component) that the photon is absorbed by that component. The x-axis shows 100 values of wavelengths from the 200 nm to 600 nm in 1 nm steps.

Summary

Table 2.1 shows how properties are defined in *OPTICS.ratdb* in RAT. Each property is specified in a pair of arrays. Value1 is the x-value in the spectrum of that property and value2 is the y-value. Figure 2.8 shows the spectrum of optical properties implemented in RAT.

Optical Property	Value
LIGHT_YIELD	Set to be 12000, to be tuned later.
SCINTWAVEFORM	value1=-5.1 value2=1.00, value1 is the decay time of the scintillator with relative contribution 1.00. For alpha particles, the same decay time is used.
RINDEX	value2 is an array of 100 values set to 1.505.
SCINTILLATION	value2 is an array of 100 values of the primary emission intensity.
SCINTILLATION_WLS	value2 is an array of 100 values of the reemission intensity.
ABSLENGTH	value2 is an array of 100 values of the total extinction length.
OPSCATFRAC	value2 is an array of 100 values of the optical scattering fraction.
REEMISSION_PROB	value2 is an array of 100 values of the total reemission probability

Table 2.1: RINDEX_value1, SCINTILLATION_value1, SCINTLLATION_WLS_value1, ABSLENGTH_value1 and OPSCATFRAC_value1, are arrays of wavelengths from 200 nm to 600 nm in 4 nm steps corresponding to the wavelength at which the optical parameter value is for.

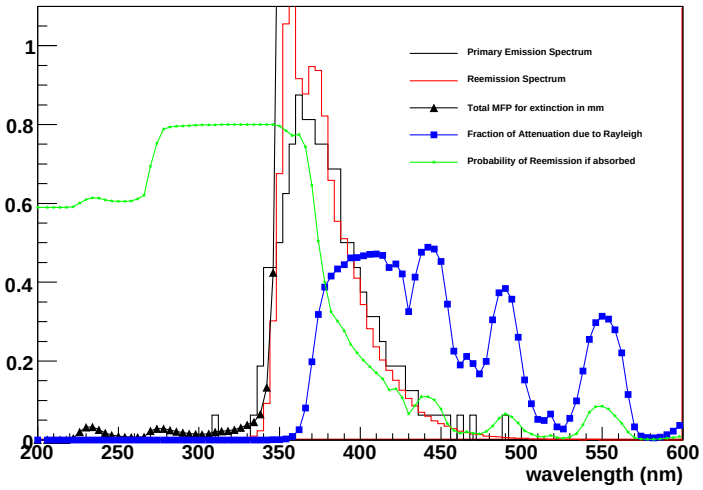

Figure 2.8: This plot shows primary emission spectrum, reemission spectrum, reemission probability for the scintillator mixture as a function of wavelength, mean free path for extinction (sum of all processes) and Rayleigh scattering as a function of wavelength (y-axis units are different for each curve and are arbitrary). Each curve is a graph of a table of optical parameters implemented in RAT.

2.2 Backgrounds in SNO+

The objectives of SNO+ are to search for neutrinoless double beta decay of ^{150}Nd using a Nd-loaded liquid scintillator and to study low energy solar neutrinos. Both physics objectives can only be achieved if backgrounds from radioactivity can be made very low. It is important to understand backgrounds in SNO+ as well as possible. This section introduces backgrounds in SNO+. Not all of these backgrounds are worrisome in SNO+ and not all of these backgrounds will be examined later in this thesis. Nevertheless, this overview places the backgrounds that were studied as part of this thesis research in context.

There are several sources of backgrounds in neutrino experiments. They include:

a) cosmic rays (muons), b) internal and external radioactivities. These sources of background will be discussed below.

2.2.1 Muon Backgrounds

Cosmic ray muon backgrounds are the least worrisome background. Even though the 2 km of rock overburden which is equivalent to roughly 6000 m water [19] shields the experiment from most cosmic rays, a small number of muons do penetrate the rock and reach the detector, also producing secondary particles like neutrons. Muons pass through the detector at a rate of approximately 3 per hour. In SNO, the muon rate was 68.9±1.8(stat) per day and the muon-induced neutron rate was 11.4±0.74 day^{-1} kt^{-1} [33]. But this muon background does not affect the SNO+ experiment because muons are easily identified when the traverse the detector and because both the double beta decay signal and the solar neutrino signal in SNO+ can be easily distinguished from muon backgrounds mostly because of the energy deposited in the detector being different.

2.2.2 Internal and External Radioactivities

In SNO+, the Acrylic Vessel (AV) will be filled with scintillator and the radioactive backgrounds can be separated into two parts: internal radioactive backgrounds from the scintillator and external radioactive backgrounds from the AV, PSUP, ropes and external H_2O.

Internal backgrounds

Backgrounds are considered as internal if they arise due to radioactive impurities in the liquid scintillator. Impurities directly in the scintillator can produce scintillation light in the detector from alpha, beta and gamma decays. The most important decay chains in natural radioactivity are those from ^{238}U and ^{232}Th, and also the decay of ^{40}K.

Figure 2.9 and 2.10 shows the decay chains of ^{238}U and ^{232}Th of background to the double beta decay experiment. In the decay chain of ^{238}U, ^{214}Bi is a direct source. It decays by β emission with a large Q-value of 3.27 MeV which is very close to the 3.37 MeV Q-value of ^{150}Nd neutrinoless double beta decay. In the decay chain of ^{232}Th, ^{208}TI is also a direct source of background. It finally decays to ^{208}Pb and emits a 2614 keV gamma ray. ^{40}K is a naturally occurring isotope of potassium (0.0117%). Approximately 89% of ^{40}K decays occur by beta emission to the stable state of ^{40}Ca with a Q-value of 1.311 MeV while the other 11% of ^{40}K decays occur via electron capture or β^+ emission to the stable ^{40}Ar with the emission of a 1460 keV gamma. Because the liquid scintillator is very sensitive to low energy particles, these two gamma rays are very important candidate backgrounds to understand for the SNO+ experiment.

^{222}Rn with a half-life of 3.8234 days is one of the most important backgrounds in neutrino experiments. As a noble gas in the ^{238}U decay chain, it is present in most environments – existing in ambient air at concentrations of about 10-20 Bq/m^3 [35] and at much larger concentrations (factors>10 higher) underground in mine air. ^{222}Rn decays via several daughter nuclei to ^{210}Pb with a long half-life of 22.2 years that can be a background problem because of the long half-life that allows for this

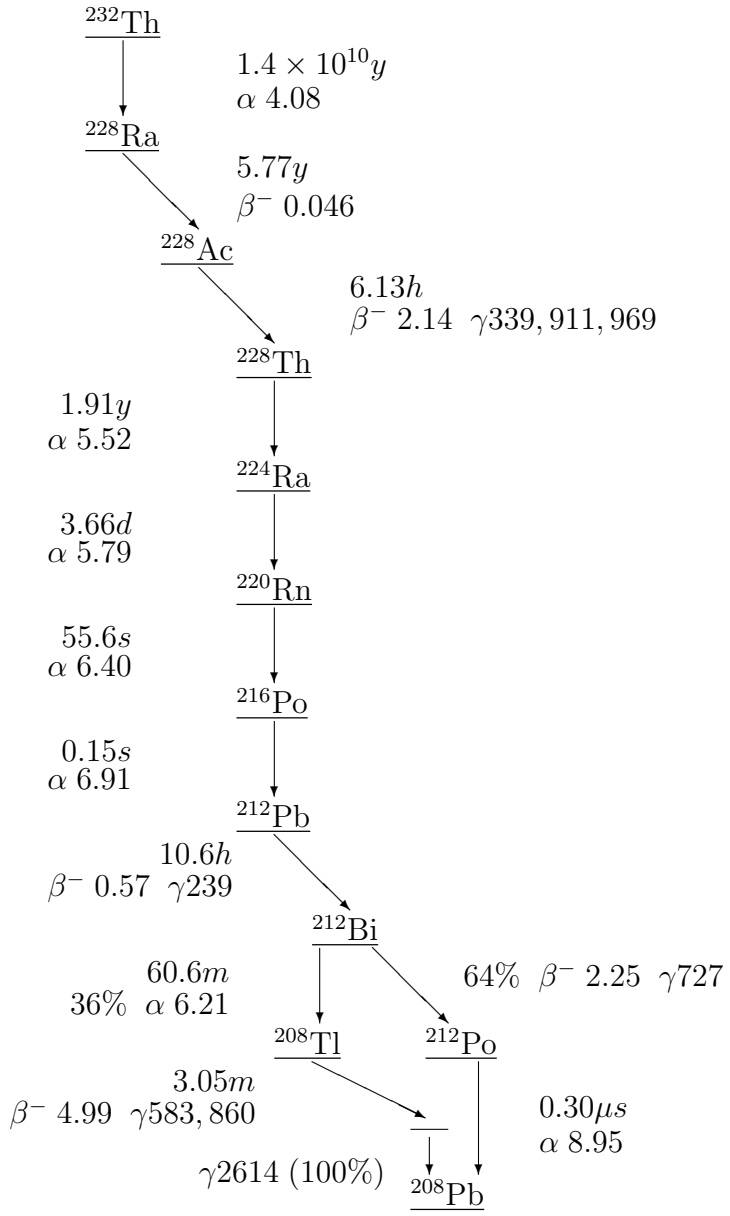

Figure 2.9: The decay chain of ^{232}Th. All half-lives are shown, with the Q-values of beta and alpha decays in MeV, and gamma rays in keV. [34]

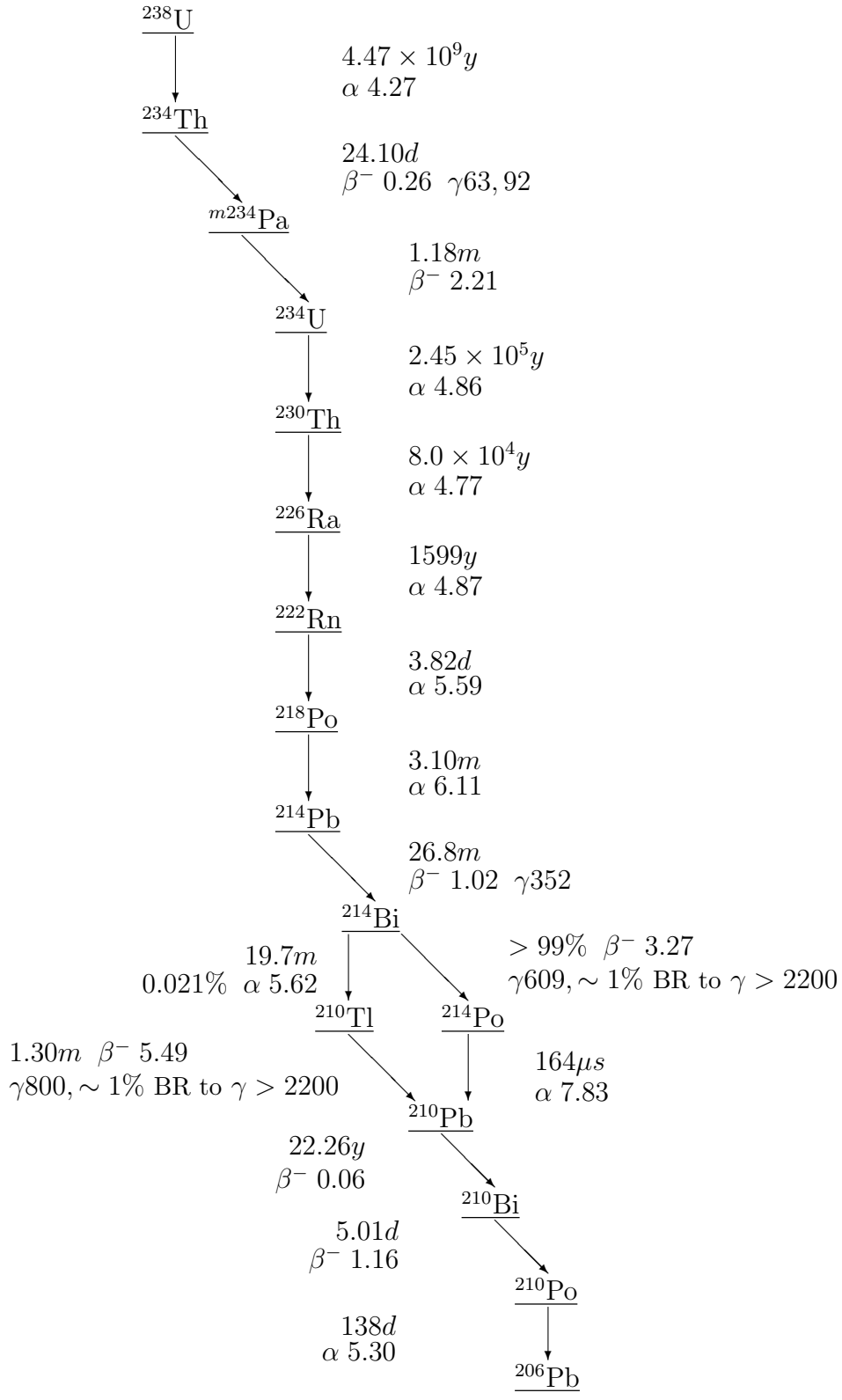

Figure 2.10: The decay chain of ^{238}U. All half-lives are shown, with the Q-values of beta and alpha decays in MeV, and gamma rays in keV.[34]

activity to build up over a long period of radon exposure.

In Figure 2.10, the decay chain of ^{238}U, the decay of Rn daughters ^{214}Bi and ^{214}Po is described. The beta decay of ^{214}Bi (plus gammas) is followed by an alpha decay of ^{214}Po in a very short time (half-life of 164 μs). In Chapter 5, the ^{214}Bi-^{214}Po coincidence analysis will be used to identify radon as a background source in measurements made with a liquid scintillator test deployment.

External Backgrounds

Backgrounds are considered as external if they originate from the detector material and the shielding material around the detector. Gamma rays are the main contributors since alpha and beta particles that originate in the Acrylic Vessel or surrounding water can't penetrate and reach the scintillator.

For the SNO+ experiment, there are target levels of radiopurity that have been set so that internal backgrounds are smaller than neutrino signals (or double beta decay signals). For external backgrounds in SNO+, there is some information that can be deduced from counting rates in SNO (as to the amount of ^{238}U and ^{232}Th in the light water surrounding SNO, and values for U and Th in the Acrylic Vessel). However, the gamma ray from ^{40}K decay has energy 1.46 MeV and this is much below the detection threshold that SNO can study (also so low that it was not an important background to quantify for SNO). On the other hand, this will be a very important background for SNO+. It would be valuable to attempt to quantify the ^{40}K levels in the detector. To obtain that, a scintillator source was deployed at the bottom of the Acrylic Vessel to attempt to measure the external backgrounds (gammas from the AV and surrounding water).

2.3 Summary

This chapter introduces scintillator optical properties and background concerns for the SNO+ experiment. Scintillator optical properties are important to quantify and to implement in the Monte Carlo simulation – having a good physical model of scintillation light will improve simulations, help the design of the SNO+ experiment, and will be required for data analysis. Radioactive backgrounds are always important for neutrino experiments and important backgrounds from Rn and Rn progeny, and from internal and external gamma rays were introduced. The research work to be described next in this thesis is centred on a deployment of a scintillator test source in SNO which enabled measurements of scintillator optical properties and of radioactive backgrounds to be attempted.

Chapter 3

Measurement

3.1 Introduction of the Scintillator Bucket

3.1.1 Objective of the Scintillator Bucket

In Chapter 2, the optical properties of the scintillator in RAT were discussed. To tune the parameters of optical properties in RAT, a scintillator test source known as the scintillator bucket was made to be deployed in the SNO detector filled with water to investigate several important optical properties, including the light yield of the scintillator. At the same time, the model of the scintillator bucket in RAT was simulated. By comparing the data from measurements and simulations, the optical properties in the simulation can be corrected and the model can be improved. To correct the light yield in RAT, the scintillator bucket with a neutron source on its side or top was deployed in the centre of the detector to measure the light output. In addition, the scintillator bucket without the neutron source was deployed in the centre to investigate the internal background or at the bottom to examine the external

background.

3.1.2 Construction of the Scintillator Bucket

An illustration of the scintillator bucket is shown in Figure 3.1. The construction of the bucket is show in Figure 3.2. The major part of the scintillator bucket is an acrylic cylindrical container with an acrylic plate on its top and another acrylic plate on its bottom that can be filled with scintillator. Six copper rods hold all these parts together. The black cylinder at the bottom is the americium-beryllium (AmBe) neutron source with a white teflon source holder. A standard ^{241}AmBe source is a 1.91 cm diameter, 5.08 cm long double sealed stainless steel capsule.

The list below shows the dimensions and materials of the parts of the bucket.

- Cylindrical container: 7.62 cm inner diameter, 10.16 cm outer diameter, 1.27 cm thick, 25.40 cm in height, 1158 cm^3 internal volume (filled with scintillator); made of UVT (UV transmitting) acrylic.
- Top solid cylindrical flange (at the top of the container): 13.02 cm diameter, 15.24 cm in height; made of clean acrylic.
- Bottom solid cylindrical flange (at the bottom of the container): 13.02 cm diameter, 2.54 cm in height; made of clean acrylic.
- Top copper flange (at the top of the top cylindrical flange): 13.02 cm diameter, 1.27 cm in height.
- 6 copper rods (surrounding the container and threading through the flanges): 0.64 cm diameter, 47.63 cm in height.

- copper flat washer and copper nuts (at each end of the copper rods)
- Three teflon O-rings (around the groove between container and top cylindrical flange, between container and bottom cylindrical flange, between top cylindrical flange and top copper flange) to seal the container so that it won't leak.
- Copper rod (threading through the top copper flange) with a stainless steel flange at top. This rod and stainless steel flange enabled the scintillator bucket to be attached to the source manipulator system in the SNO detector.
- 2 stainless steel male connectors (at the top of copper flange) connecting two tunnels in the top acrylic flange.
- Acrylic tube (plugged into the container when the scintillator is filled): 0.95 cm outer diameter, 0.64 cm inner diameter, 25.40 cm in height.

Figure 3.1: A photo of the scintillator bucket with the AmBe neutron source (black cylinder) beside it.

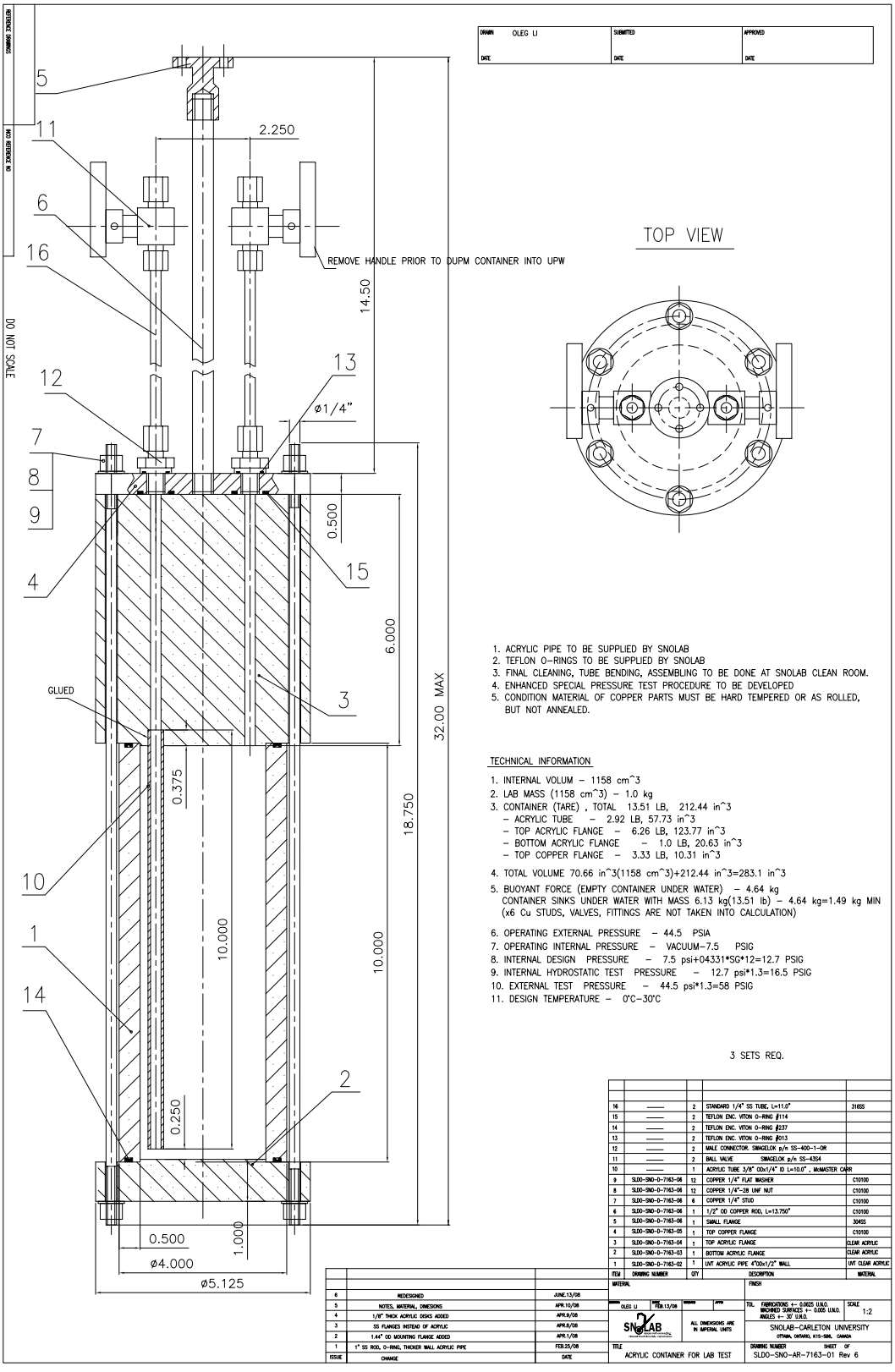

Figure 3.2: The construction design of the scintillator bucket. The unit used is inches for all dimensions.

3.2 Assembly and Pressure Test

Alex Wright[36] did the preparation work for the scintillator bucket. Acrylic parts were ramping for 24 hours to 80 °C and annealed for 4 days at 80 °C. They were ultrasonically cleaned for 36 hours, then immersed in ultra pure water (UPW) for 45 minutes, and rinsed with distilled water. Copper parts and O-rings were ultrasonically cleaned for 45 minutes, and then rinsed with distilled water.

After cleaning, the bucket was assembled by Alex and submerged into water for a pressure test (80 PSI) to make sure that the bucket would not leak [36]. For the leak test, first the empty bucket was submerged in UPW at normal pressure and soaked for 2 hours. No water was observed to enter the source. Then the bucket was sealed in a plastic bag filled with UPW. The whole bag was then submerged in more UPW in a pressure test cylinder. The cylinder was connected to a water supply which brought the pressure in the cylinder up to the 80 PSI for 30 minutes. Again, no water was observed in the source after this test.

3.3 Measurements

During the measurements, the scintillator bucket was filled with three types of scintillator: the raw LAB + 2 g/L PPO, 0.1% Nd-loaded LAB + 2 g/L PPO and distilled LAB + 2 g/L PPO. For each of the three types of scintillator, the bucket was put in different locations in the detector. The acrylic vessel was filled with light water (H_2O) and the scintillator bucket was deployed in the acrylic vessel using the calibration manipulator system described in [19]. On September 29, 2008, the detector was set up and the HV was turned on. The scintillator bucket was filled with raw

scintillator and installed in the detector for a run of several hours to find the correct threshold which can eliminate some of the non-physics events. On September 30, 2008, the scintillator bucket was deployed in the centre of the detector. Each good run lasted about an hour. The schedule of measurements is shown in Table 3.1. The details of each run are shown in Appendix 1.

Run number	Scintillator	Position of Bucket(cm)	AmBe
70281-70314	raw LAB + 2g/L PPO	(0.0, -21.59, -19.92)	N/A
70324-70425	raw LAB + 2g/L PPO	(-0.02, 2.34, -0.02)	on side
70367-70425	raw LAB + 2g/L PPO	(-0.02, 2.12, 0.00)	on top
70430-70446	raw LAB + 2g/L PPO	(-0.00, -21.59, 0.03)	N/A
70476-70505	raw LAB + 2g/L PPO	(0.0, -21.59, -578.90)	N/A
70507-70527	raw LAB + 2g/L PPO	(0.00, -21.59, 0.15)	N/A
70539-70567	Nd-loaded LAB + 2g/L PPO	(-0.00, -21.59, 0.00)	N/A
70566-70595	Nd-loaded LAB + 2g/L PPO	(-0.00, -21.59, 0.00)	on side
70601-70704	Nd-loaded LAB + 2g/L PPO	(-0.00, -21.59, 0.18)	N/A
70709-70728	Nd-loaded LAB + 2g/L PPO	(0.0, -21.59, -579.25)	N/A
70738-70753	distilled LAB + 2g/L PPO	(-0.04, -2.13, -0.15)	on side
70771-70894	distilled LAB + 2g/L PPO	(-0.00, -21.59, -0.10)	N/A
70899-70909	distilled LAB + 2g/L PPO	(0.0, -21.59, -576.32)	N/A
70910-70925	distilled LAB + 2g/L PPO	(-0.00, -21.59, -0.09)	N/A

Table 3.1: Schedule of measurements of the scintillator bucket filled with different kinds of scintillator with or without neutron source. The centre of the acrylic vessel is (0, 0, 0) cm and the scintillator bucket was deployed in the centre of AV or at the bottom of AV.

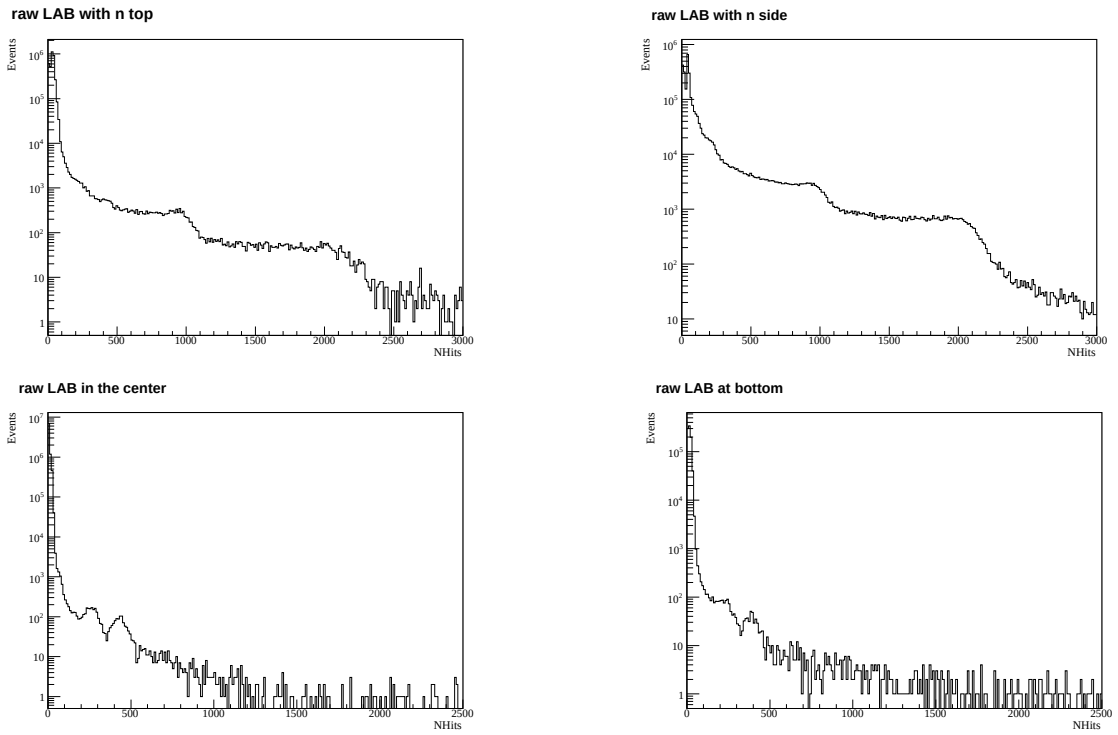

Figure 3.3: The top left plot is the Nhits spectrum for the scintillator bucket with raw scintillator and neutron source on its top, which is the total spectrum of runs 70367-70425. The top right plot is the Nhits spectrum for raw scintillator and neutron source on the side of runs 70324-70425. The bottom left plot is the Nhits spectrum for raw scintillator of all the center runs without neutron source. The bottom right plot is the Nhits spectrum for raw scintillator without neutron source of bottom runs 70476-70505. These spectra have only been corrected for the number of PMTs (see Chapter 4.2.)

Figure 3.3 shows the total Nhits (the number of phototubes hit in a single event) spectrum of different kinds of runs. For the scintillator bucket with a neutron source on its top, the Nhits spectrum had much fewer entries than of the scintillator bucket with the source on its side. Only runs of the scintillator bucket with a neutron source on the side were used to analyze the light yield of the scintillator.

3.4 Modeling of Bucket in RAT

To compare the actual data with the Monte Carlo simulation in RAT, the geometry of the scintillator bucket was coded in RAT and a visualization of this geometry is shown in Figure 3.4. The dimensions, material and position of each piece of the bucket were specified in a *GeoFactory* file and represented in a geometry file which could be included in a macro file to run jobs about the bucket. The geometry of the bucket consists of a copper rod that is used to be attach to the deployment mechanism [19]. The other end of the rod is attached to a copper plate that is coupled to an acrylic top plate. An acrylic cylinder is connected to that acrylic top plate and an acrylic bottom plate. Six copper rods are used to hold these acrylic pieces together. The size of the bucket model in the Monte Carlo is the same as the real scintillator bucket but some details such as the O-rings and copper nuts were omitted because they will not affect the results of simulation. The cylinder was made of ultraviolet transparent (UVT) acrylic, but the top and bottom section were made of the clean but non-UVT (also know as UV absorbing or UVA) acrylic. The UVT formulated acrylic has the same general properties as the clear sheet but provides increased transmission of ultraviolet light in wavelengths between 280 and 360 nm. The bucket geometry in RAT did not differentiate between the UVT and non-UVT acrylic, because this is not enough to significantly affect the results from the simulation.

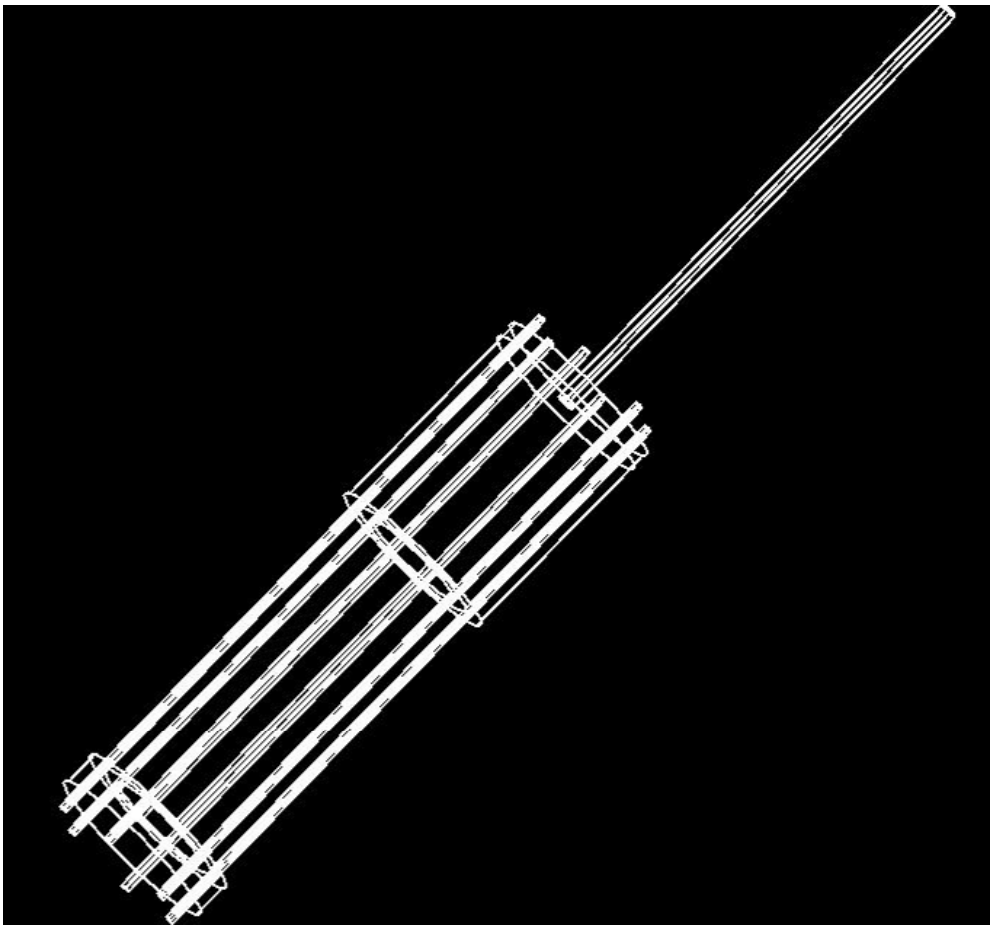

Figure 3.4: The geometry of the scintillator bucket simulated in RAT. The major part is an acrylic cylinder container which can be filled with scintillator. It is fixed by six surrounding copper rods. The inside diameter is 7.62 cm and the acrylic is 2.54 cm thick. It is 25.4 cm in height with a 15.24 cm high solid acrylic cylinder plate on its top and a 5.08 cm high solid acrylic cylinder plate on its bottom. A 1.27 cm high copper plate is coupled to the top acrylic cylinder plate and a long copper rod on top which is used to attach to the deployment mechanism.

Chapter 4

Light Yield Analysis for the Central Runs

A model of the scintillator bucket was coded in RAT and the optical properties of the bucket have also been implemented in RAT, therefore measurements of the bucket deployed in the detector can be simulated in RAT. To tune the optical properties in the Monte Carlo, such as light yield, the central runs of the bucket deployed in the centre of the AV with the neutron source on it side were used as shown in Table 4.1.

Run number	Scintillator	Position (cm)	Period	AmBe
70324-70425	raw LAB + PPO	(-0.02, 2.34, -0.02)	48 h	on side
70566-70595	Nd-loaded LAB + PPO	(-0.00, -21.59, 0.00)	23 h	on side
70738-70753	distilled LAB + PPO	(-0.04, -2.13, -0.15)	15 h	on side

Table 4.1: Details of the runs of the scintillator bucket deployed in the centre of the detector.

4.1 Compton Edge in the Nhits spectrum

The AmBe source produces neutrons which are captured by the hydrogen from H_2O, resulting in a 2.2 MeV gamma. AmBe also emits a direct 4.4 MeV gamma. When gammas pass through the scintillator, Compton scattering is the dominant interaction and the two different gamma energies produce two different Compton edges in the energy spectrum measured by collecting the scintillation light emitted in those interactions. The relation between the energy of the Compton edge and the energy of the gamma is

$$E_{max} = \frac{2E_\gamma^2}{2E_\gamma + m_e c^2} \tag{4.1}$$

where E_{max} is the energy of the Compton edge; E_γ is the energy of the gamma; and $m_e = 0.511$ MeV/c^2 is the rest mass of an electron. Using Equation 4.1 the energy of Compton edge from the 4.4 MeV gamma is 4.16 MeV and from the 2.2 MeV gamma is 1.97 MeV. When the scintillator bucket was deployed in the detector, the number of actuated (hit) PMTs in the array (Nhits) were measured. In Figure 3.3, from the Nhits spectrum for raw scintillator with AmBe source on side, the two Compton edges are clearly seen at about 900 Nhits and 2000 Nhits. The relation of known energy of the Compton edges and the observed Nhits can be used to convert Nhits to MeV allowing the Nhits spectrum to be converted to an energy spectrum.

4.2 Nhits corrections of Data and RAT simulation

To compare with the simulation results, a number of corrections [37] need to be applied to the raw Nhits for each event in all the runs of bucket in the centre with

the neutron source.

First the dark noise from the PMTs needs to be subtracted as the MC simulation does not have that noise. This dark noise observed comes from the Global Trigger in the data acquisition system which is used to the end transfer of PMT data within an event. The Global Trigger is thus periodically issued to read/clear the detector and can sample random dark noise PMT hits. Figure 4.1 shows this coincident noise distribution in a single run. A Gaussian fit (actually the distribution is a Poisson distribution but the mean values of the two distributions are close) was made to get the mean Nhits value of the noise for each run and this value was subtracted for each event in this run [38] .

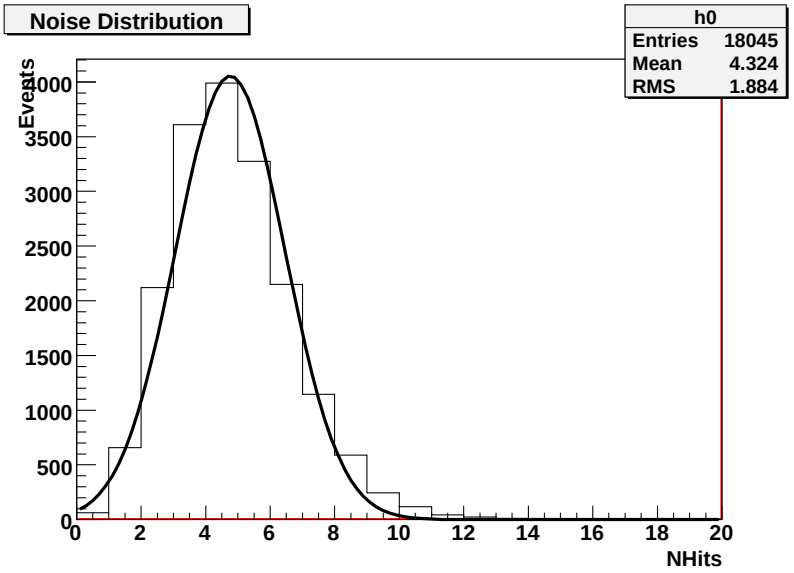

Figure 4.1: Electronic noise distribution in a single run with Gaussian fit. The mean value of Gaussian fit was subtracted from the Nhits of each event.

Second, in each run, the number of working tubes was different, but the Monte Carlo simulation assumes all tubes are working. The data need to be corrected to

account for this and the correction is

$$N_{corr} = 9456\frac{Nhits - Nnoise}{Nworking} \tag{4.2}$$

where Nhits is the number of hits recorded by the PMT, and Nworking is the number of working tubes in each run. 9456 is the total number of tubes in the detector and Nnoise is the mean Nhits value of the noise for each run.

Finally a multi-hit correction needs to be applied to account for PMTs that were hit by more than one photon. The probability of a PMT detecting n photons follows a Poisson distribution [39]

$$P(n) = \frac{x^n e^{-x}}{n!} \tag{4.3}$$

where x is the mean number of photons detected by each tube. Therefore the probability of at least one photon arriving is

$$P(n > 0) = 1 - P(n = 0) = 1 - e^{-x} \tag{4.4}$$

P(n>0) from the number of tubes that did fire

$$\frac{Ncorr}{9456} = 1 - e^{-x} \tag{4.5}$$

Therefore the mean number of photoelectrons $x = -\ln(1 - Ncorr/9456)$, and the total number of photoelectrons Ncor is

$$Ncor = -9456\ln(1 - \frac{Ncorr}{9456}) \tag{4.6}$$

In addition, in the data taken, Cherenkov light contributes to the total detected Nhits. The Monte Carlo can simulate both Cherenkov light and scintillation. The Cherenkov contribution can be simulated precisely and then subtracted from the data, so that the observed scintillation can be compared to the simulated amount of scintillation. The Cherenkov contribution value [39] was from Monte Carlo using

"non-scintillating" LAB with PPO. This was achieved by turning off the function of scintillation in the Monte Carlo and the value is shown in Table 4.2.

Edge	Nhits Correction
First edge 1.97 MeV	-10.7
Second edge 4.16 MeV	-24.6

Table 4.2: Cherenkov Contribution for the two Compton edges.

Monte Carlo simulations in RAT also need the multi-hit correction and to have the Cherenkov contribution subtracted. RAT simulates all 9456 tubes working and does not add noise, so Monte Carlo simulated data does not need these corrections.

4.3 Comparison of Nhits Spectra from Data and Simulation

In this experiment, three kinds of scintillator were used: raw LAB mixed with PPO, Nd-loaded LAB mixed with PPO and distilled LAB mixed with PPO. In Monte Carlo, there are only two kinds of scintillator: LAB mixed with PPO and Nd-loaded LAB mixed with PPO. In RAT simulation, a number of 1 keV neutrons and 4.439 MeV gammas were generated separately on the side of the bucket source at a position of (75.0, 0.0, -101.6) mm. A total of 10,000 gammas and 10,000 neutrons were generated in RAT. Their Nhits spectra were combined together and then compared with the actual data from raw and Nd-loaded scintillator runs. Figure 4.2 shows the Nhits spectra from the actual data and simulations in RAT.

From Figure 4.2, there are two Compton edges in both actual data and simulated Nhits spectrum. But for simulated Nhits spectrum in RAT, the Nhits of the two edges

are higher than those of actual data which means the light yield of the scintillator in RAT is higher. The light yield of both raw and Nd-loaded scintillator were set to be 12,000 photons/MeV in RAT. From comparing the Compton edge in RAT and data, the light yield of the scintillator in simulation should be tuned to be lower.

To tune the light yield in simulation, first, Equation 4.7 to 4.10 were used to fit the Compton edges which was a construction of a step function and a Gaussian [37].

$$stepdown = \frac{p_0}{p_0 + p_1^{x-p_0}} \tag{4.7}$$

$$stepup = \frac{p_0}{p_0 + p_1^{p_0-x}} \tag{4.8}$$

$$gaus = e^{-\frac{(x-p_0)^2}{2p_2^2}} \tag{4.9}$$

$$function = p_3(stepdown + stepup \cdot gaus) \tag{4.10}$$

where p_0 = point of inflexion that is also the mean of the Gaussian, p_1 = the strength of the turnover, p_2 = sigma of Gaussian and p_3 = constant before the slope down which is the overall normalization before the Compton edge goes down. The equation of "stepdown" is to construct a downwards step; the equation of "stepup" is to construct a small upward step at the Gaussian peak and "gaus" is a Gaussian function.

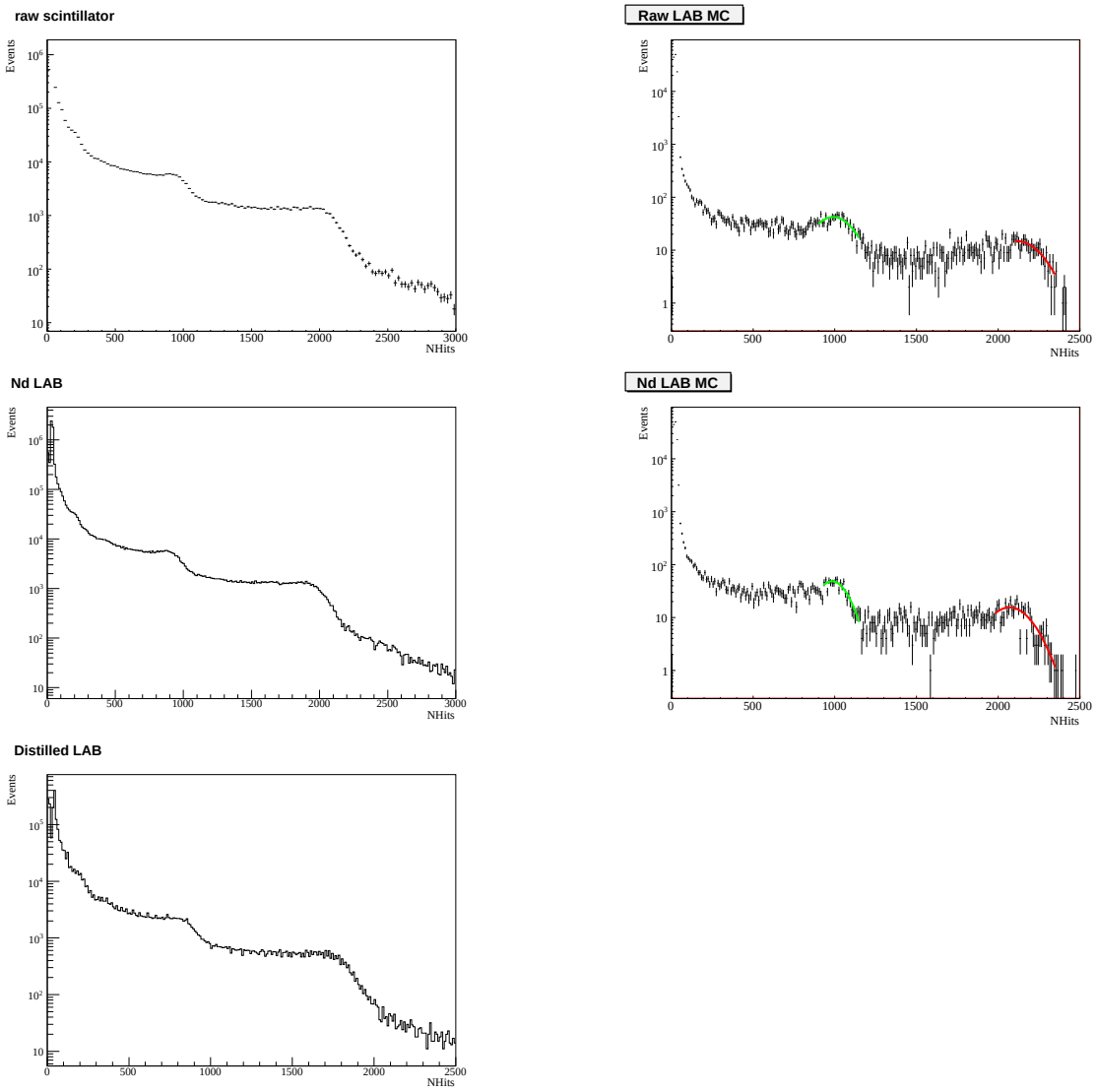

Figure 4.2: From top-left, and reading across and down: the Nhits spectrum from raw LAB data; the Nhits spectrum of LAB scintillator in Monte Carlo; the Nhits spectrum of Nd-loaded scintillator data; the corresponding Nhits specrum of Nd-loaded scintillator in Monte Carlo; the Nhits spectrum of distilled LAB scintillator data. Green and red curves (in the Monte Carlo) show the fit to functions at the Compton edges.

Comparison of the positions of edges in data and Monte Carlo is given in Table 4.3.

Scintillator	Energy(MEV)	Data (Nhits)	MC (Nhits)
Raw LAB	1.97	888 ± 3.7	962.8 ± 5.7
Raw LAB	4.16	1951.4 ± 5.6	2107.4 ± 14.8
Nd LAB	1.97	859.0 ± 2.5	905.3 ± 9.4
Nd LAB	4.16	1839.4 ± 5.6	1917.4 ± 12.5
Distilled LAB	1.97	805.8 ± 4.3	N/A
Distilled LAB	4.16	1664.4 ± 3.1	N/A

Table 4.3: Comparison of corrected Nhits at Compton edges in data and Monte Carlo for the three types of scintillator. The corrected Nhits of the Compton edges in MC are higher than in data.

A linear fit was made to a plot of Energy (MeV) versus Nhits and the fitted slopes and intercepts are given in Table 4.3. The fitted gradient is the light yield in Nhits per MeV. Comparison of the data and MC allowed the tuning factor for the light yield to be calculated for the Monte Carlo. The results are plotted in Figure 4.3.

Scintillator	Slope(Nhits/MeV)	y-intercept(Nhits)
Raw LAB	485.6 ± 3.1	-9.6 ± 12.8
MC Raw LAB	522.6 ± 7.2	-64.2 ± 17.1
Nd LAB	447.7 ± 2.8	-20.7 ± 6.9
MC Nd LAB	462.0 ± 7.1	-2.5 ± 21.1
Distilled LAB	396.3 ± 2.3	-2 ± 5

Table 4.4: The result of a linear fit to the Compton edge positions. The slope thus represents the conversion of Nhits into energy. The negative y-intercept suggests that the scintillator detector behaves as though it has an excitation energy or threshold.

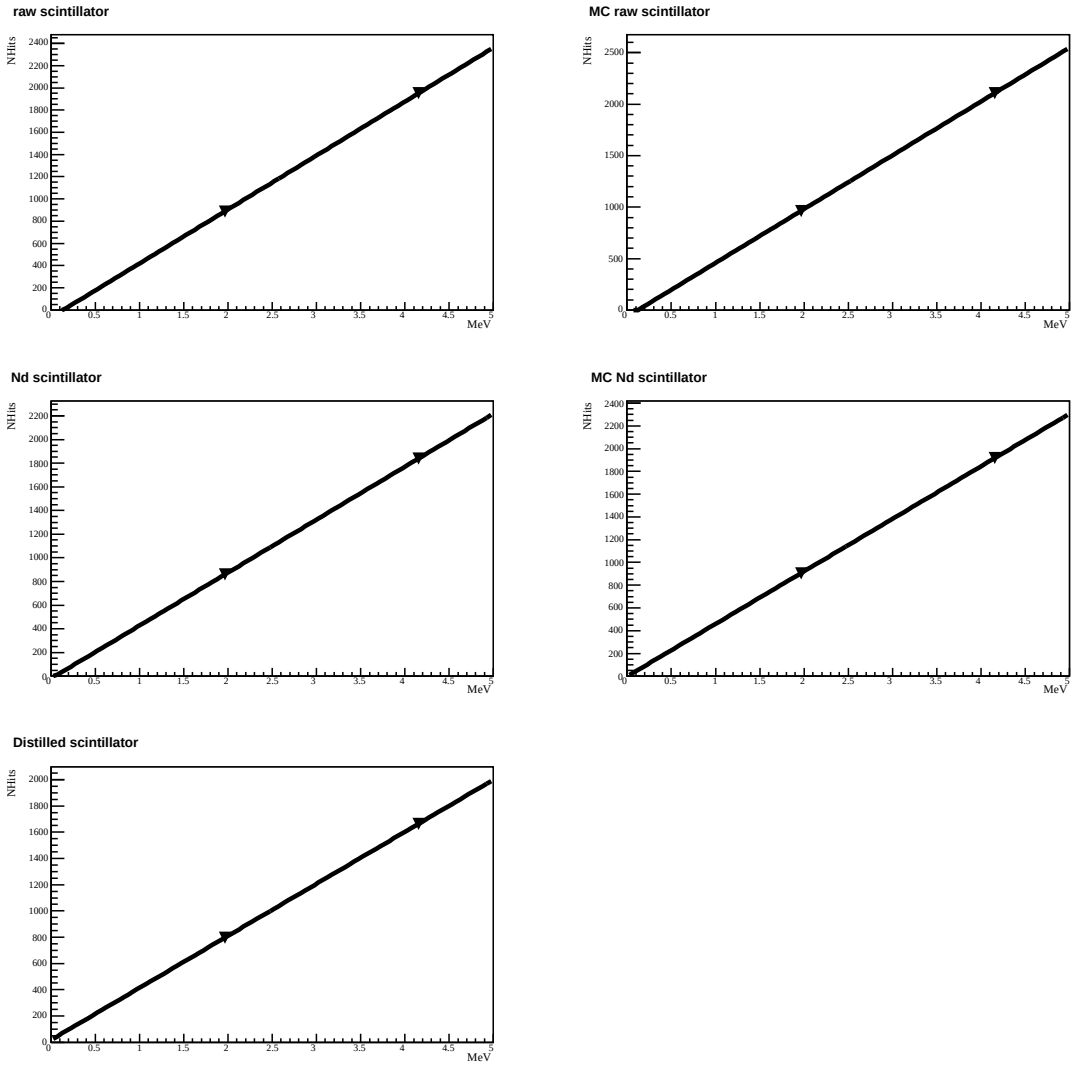

Figure 4.3: These plots show the Compton edge Nhits-MeV linear fits. Data plots are on the left; Monte Carlo plots are on the right. The type of scintillator is given in the labels above the plots.

From Table 4.3, the fitted edges of MC are higher than the data. From Table 4.4, the mean Nhits per MeV is approximately 8% higher in Monte Carlo for raw scintillator, approximately 5% higher in Monte Carlo for Nd-loaded scintillator. The

intrinsic scintillation light yield is proportional to Nhits per MeV observed in the detector. From the analysis described above, it can be concluded that the scintillation light yield in the simulation should be adjusted to 11,111 photons per MeV for raw scintillator and 11,400 photons per MeV for Nd-loaded scintillator, down from 12,000 photons/MeV used in generating the MC plots above.

With the adjusted light yield value, the simulation was repeated and compared again with the data. A comparison of the adjusted RAT simulations of the Compton edges and the data are shown in Figure 4.4. In this figure, it is clear there is a background in the actual data (which is not in the simulation because backgrounds were not simulated). A function (Equation 4.12) was used to fit the data histogram.

$$background = A \cdot e^{B \cdot x} \tag{4.11}$$

$$\text{function} = C \cdot Nneutron + D \cdot Ngamma + background \tag{4.12}$$

where background is a simple exponential fit; Nneutron is the number of simulated neutrons, Ngamma is the number of simulated gammas and C and D are scaling parameters.

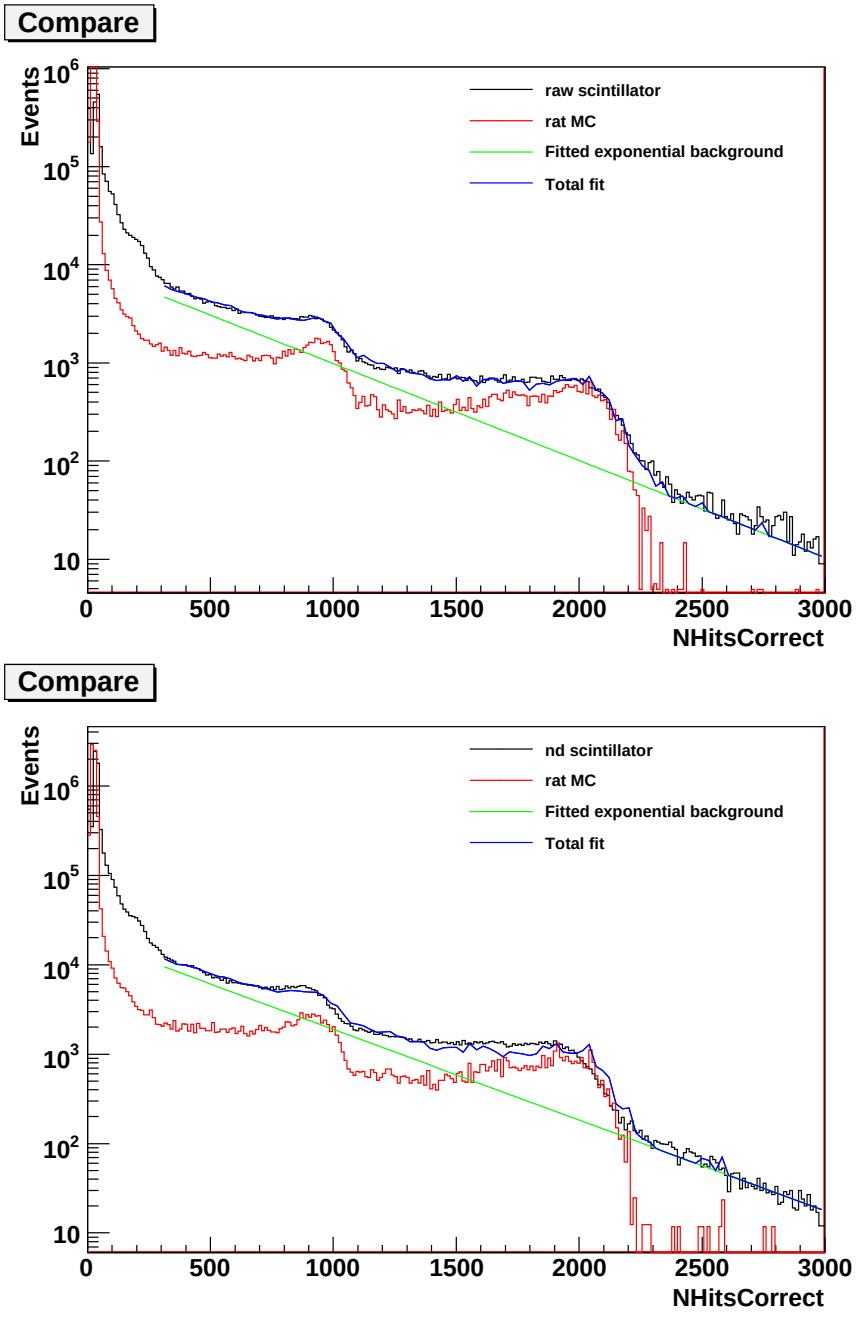

Figure 4.4: The top plot is the comparison of Monte Carlo results with backgrounds added (fitted) to the data for raw LAB with the intrinsic scintillation light yield set to 11,111 in the Monte Carlo. The bottom plot is the comparison of Monte Carlo results with backgrounds added (fitted) to the data for Nd-loaded LAB with the intrinsic scintillation light yield set to 11,400.

The MC histogram with a fitted background added to it match the data histogram reasonably well since the model of a single exponential background is just an approximation and this level of background modeling is sufficient for present purposes.

For the Nd-loaded LAB in Monte Carlo, the tuned light yield 11400 is higher than that of raw scintillator. However, because of the absorption of Nd or quenching, the light yield of Nd-loaded scintillator should be lower than that of raw scintillator. This suggests that optical properties for Nd-loaded scintillator are not adequately described in the Monte Carlo. From Table 4.4, the Nhits per MeV of Nd-loaded scintillator is 7.8% lower than that of raw scintillator in actual data while in simulation the Nhits per MeV of Nd-loaded scintillator is 11.6% lower than that of raw scintillator, which means the attenuation of Nd-loaded scintillator in Monte Carlo seems to be overcorrecting. The optical properties of Nd-loaded scintillator coded in RAT need to be examined and measurements of optical properties of Nd-loaded scintillator also need to be re-examined.

In addition, from Table 4.4 the light yield of distilled scintillator observed is 18.4% lower than that of raw scintillator. The purification of the scintillator is known to increase its transparency and so the light yield of distilled scintillator should be the same as that of raw scintillator, if not better. The possible reasons for the decreased light yield are: the intrinsic light yield from LAB might be harmed during the distillation or there were contaminants in the scintillator during its preparation which quenched the light output. It is now known, for further investigations, that the intrinsic scintillation light yield is not harmed by distillation and the conclusion for the scintillator bucket source is that the distilled sample was contaminated.

4.4 Conclusion

Nd-loaded scintillator was observed to have approximately 7.8% lower light yield than the unloaded scintillator which agrees with the bench top measurements [31] referred to in Chapter 2. This may be due to the absorption of Nd. Distilled scintillator was observed to have 18.4% lower light yield than the undistilled scintillator. Subsequent work has allowed us to uncover that the distilled sample was contaminated during filling of the scintillator bucket. By comparing the corrected Nhits spectra of data and simulation results, the tuned light yield in the simulation for raw scintillator is 11111 and for Nd-loaded scintillator is 11400. The incorrect higher light yield for Nd-loaded scintillator in Monte Carlo is due to the inadequate characterization of the optical properties of this scintillator, as coded in RAT. Future work on the Nd-loaded scintillator properties and Monte Carlo will be needed.

Chapter 5

Background Analysis

Backgrounds from radioactivity in the SNO+ experiment were introduced in Chapter 2. With the scintillator bucket deployed in the SNO detector without the AmBe neutron source, it was possible to examine the quantities of these backgrounds. With the source in the centre of the AV, internal backgrounds to the scintillator could be examined. With the source deployed at the bottom of the AV, there was the possibility that external background gammas could be observed.

5.1 Background Nhits Spectrum

Three kinds of scintillator were filled in the bucket and background runs with the bucket at the centre of the detector and at the bottom were taken. Table 5.1 gives some details of the runs.

Run number	Position	Scintillator	Period(hr)
70281-70314 70430-70446 70507-70527	in the centre	Raw LAB +PPO	29
70539-70567 70601-70704	in the centre	Nd-loaded LAB + PPO	75
70771-70894 70910-70925	in the centre	Distilled LAB + PPO	56
70476-70505	at the bottom	Raw LAB + PPO	18
70709-70728	at the bottom	Nd-loaded LAB + PPO	19
70899-70909	at the bottom	Distilled LAB + PPO	9

Table 5.1: Summary of the runs of the bucket used to study backgrounds.

For the background analysis, a "DAMN" mask (00B17FE5 for bottom runs and 00F16FE1 for central runs) was used to exclude instrumental and electronic backgrounds. Each event has a series of cuts applied to test whether the event was a real one or the result of instrumental or electronic problems. For example, the distribution of hits in the event can be examined for "crate isotropy" (too many hits in just one electronics crate) which could signal a false event from electronics noise pickup. The pass-fail result of all such cuts are stored as a series of bits for each event in a DAMN bank. Then, the DAMN mask is the correct value of those bits that indicates it is a good event and the DAMN mask is applied as a bit-for-bit logical AND with the DAMN bank value for each event.

Corrections to Nhits, described in Chapter 4 for the light yield analysis, are also used for the background analysis. These are: subtraction of dark noise hits, correcting for the number of working PMTs and the multi-hit correction. (Note: the multi-hit correction as described in Chapter 4 assumes the same average number of detected photoelectrons in all PMTs which is correct for the bucket deployed in the centre but not 100% correct for the bucket deployed at the bottom, since the probability of a PMT hit is related to its distance from the scintillator bucket. The multi-hit

correction is not large and the same calculation was also used for bottom runs).

Figure 5.1 shows the Ncor spectrum of central and bottom runs for raw, Nd-loaded and distilled scintillators. All of the spectra are similar with two peaks clearly seen at about 200 Nhits and 400 Nhits with the only exception being the raw scintillator data from bottom runs for which there might be the lower peak at reduced intensity only. This might be because the raw scintillator was filled in the scintillator bucket a longer period of time before the bottom runs (compared to the other two scintillators) and that these peaks were from radioactivity that decayed. Studies of ^{222}Rn in the scintillator, discussed in the next section, support this idea.

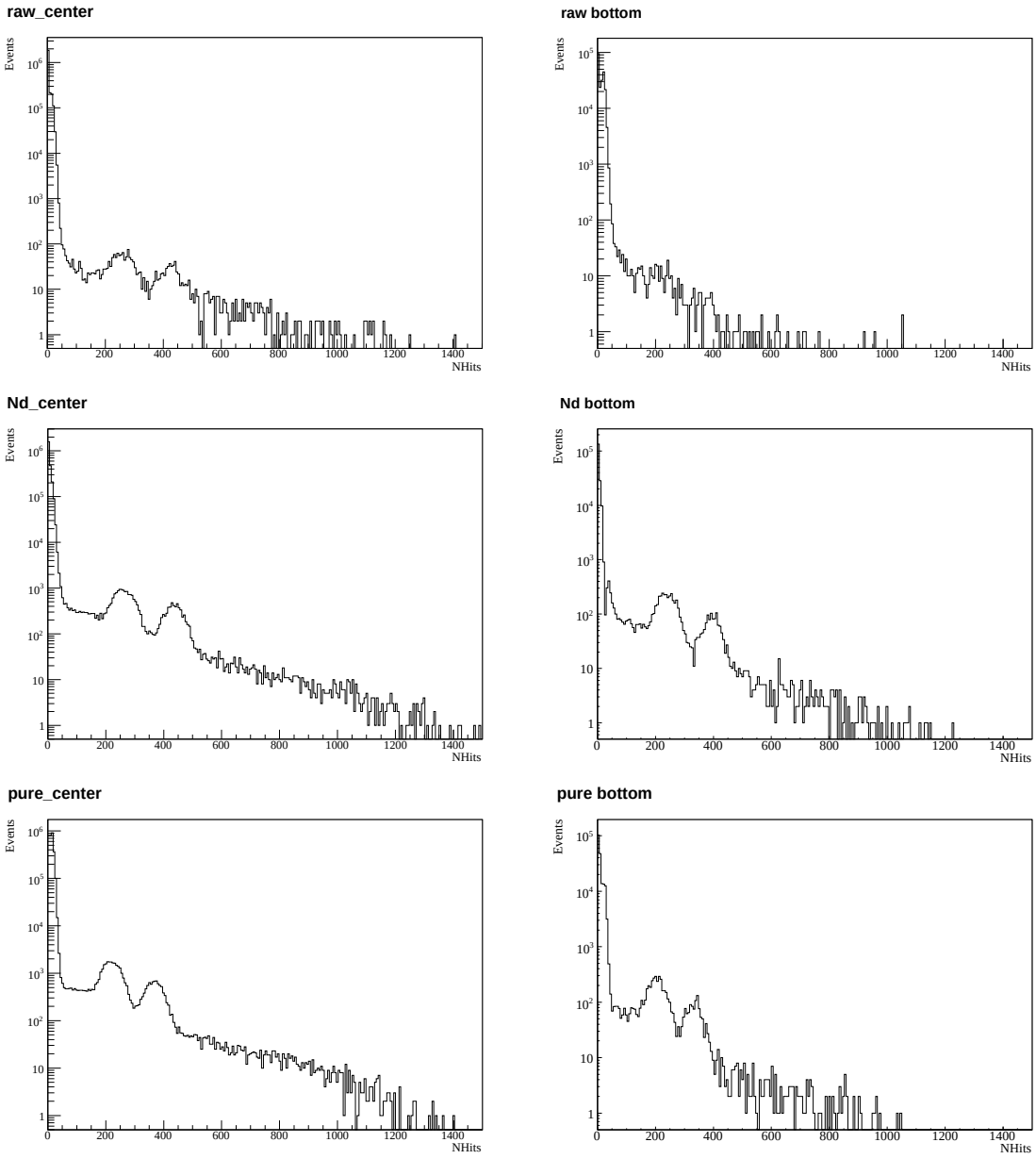

Figure 5.1: Ncor background spectrum for raw, Nd-loaded and distilled (pure) scintillators. The left column shows central runs and the right column shows bottom runs.

5.2 Backgrounds from ^{222}Rn

The most likely cause of these two peaks was ^{222}Rn gas that had been dissolved in the scintillator samples during their preparation. The lower energy alpha peak (first peak) could be caused by alpha quenching of ^{222}Rn (Q = 5.59 MeV) decays and ^{218}Po (Q = 6.11 MeV) decays in the scintillator and the higher energy peak (second peak) could be caused by alpha quenching of ^{214}Po (Q = 7.83 MeV) decays. A coincidence analysis of ^{214}Bi-^{214}Po was performed to demonstrate that the second peak is due to decays of ^{214}Po, the daughter of ^{222}Rn. In addition, the positions of all the events after an energy cut were reconstructed to show that all the coincidence events were from the scintillator bucket. A separate analysis of backgrounds in central runs was performed [38] and my work was focused on the background analysis for the bottom runs.

5.2.1 Beta-Alpha Coincidence Analysis

The daughter nucleus of ^{222}Rn, ^{214}Bi decays by β emission to ^{214}Po. This 3.27 MeV (Q-value) β is followed by a 7.83 MeV (Q-value) α with a half-life of 164 μs. The 7.83 MeV α is likely to cause the second peak. The second peak at about 400 Nhits is roughly 1 MeV using the Nhits-MeV conversion from Chapter 4. That means α particles were quenched in the scintillator. Observation of the β-α coincidence can show if the background peaks were caused by ^{222}Rn contamination.

All good coincidences events were selected in a way that an event with Ncor>50 was followed by another event with Ncor>50, within 660 microseconds of each other. The time window of 660 μs is approximatively four ^{214}Po half lives and the 50 Ncor

cut excludes PMT hits from Cherenkov. Figure 5.2 shows the spectra of the first event (beta) and the second event (alpha) in coincidence together with the Ncor spectra for three scintillator samples. A exponential fit was made to the plot of the time between β and α events, and this is shown in Figure 5.2. The number of coincidence events and fitted results are given in Table 5.2.

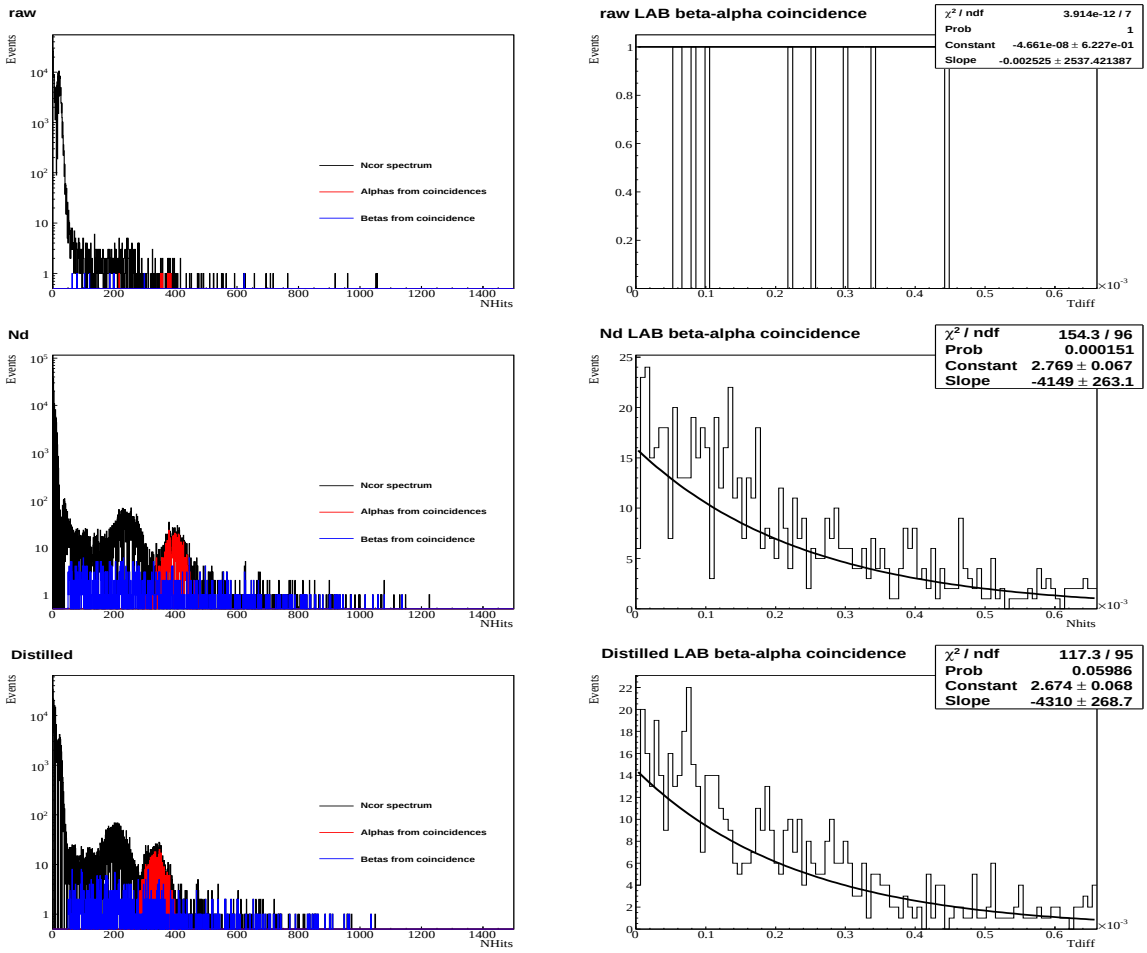

Figure 5.2: The left column plots show alpha and beta events in coincidence together with the Ncor spectra for three scintillator types. The right column plots are spectra of the number of β-α coincidences versus the time difference between them for three scintillator types.

Scintillator	Fitted half-life (μs)	Number of coincidences
Raw scintillator	N/A	9
Nd-loaded scintillator	167 ± 11	696
Distilled scintillator	161 ± 10	592

Table 5.2: The fitted results of the number of β-α coincidences versus the β-α time difference for three kinds of scintillator and the number of β-α coincidences for three kinds of scintillator

As Figure 5.2 shows that for Nd-loaded and distilled scintillator samples, all alpha events fall in the range of the second peak. And the fitted half-life values agree with the 164 μs half-life of ^{214}Po which indicates that these were genuine $\beta-\alpha$ coincidences from Rn daughters. For the raw scintillator, the coincidence rate was very low and it was impossible to fit the half-life, but almost all the alpha events still fall in the range of 300 to 400 Nhits where the second peak should be. So, the assumption that the second peak was caused by the 7.83 MeV α decay of ^{214}Po is proved. The low coincidence rate for the raw scintillator is consistent with the fact that the raw scintillator was prepared so early that Rn and its daughters already decayed before the bottom runs were taken.

5.2.2 Comparison of half-life

The coincidence analysis above shows the second peak originates from ^{222}Rn daughters. Adding an energy cut of alpha events within $\pm 2\sigma$ of the mean of the second peak will tighten the coincidence analysis. A Gaussian fit to the second peak energy is shown in Figure 5.3 with parameters given in Table 5.3.

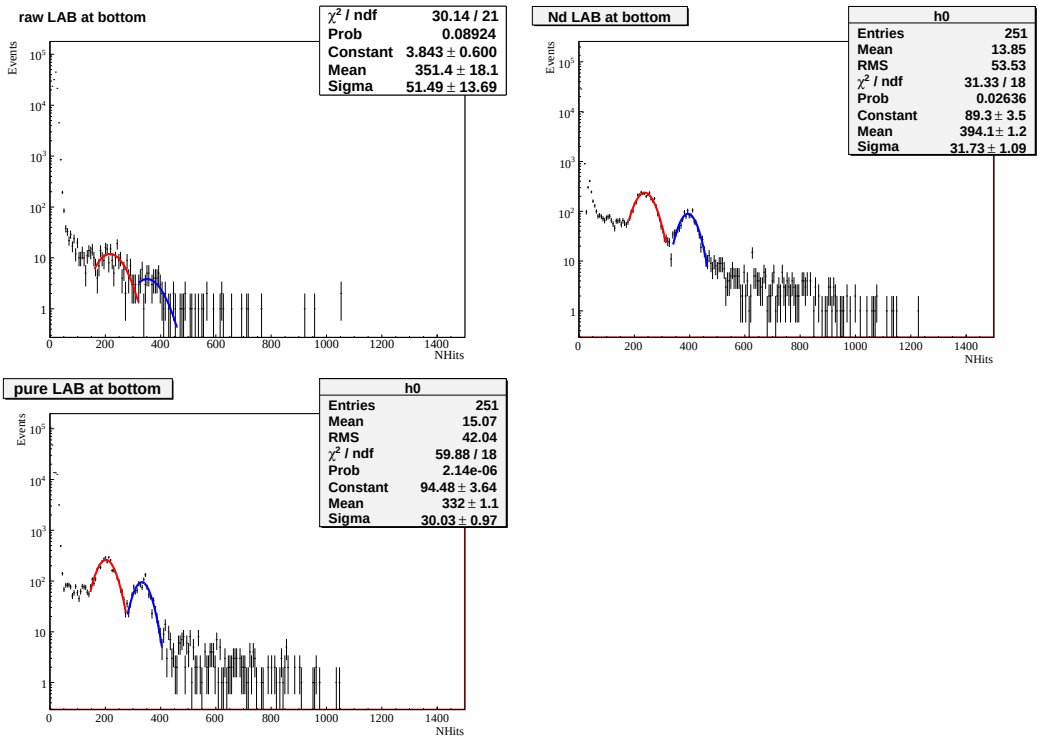

Figure 5.3: Gaussian fits to the two peaks for scintillator samples.

Scintillator	Peak	Mean(Nhits)	Sigma(Nhits)
Raw scintillator	First peak	217.5 ± 5.5	48.8 ± 5.4
	Second peak	351.4 ± 18.1	51.5 ± 13.7
Nd-loaded scintillator	First peak	237.6 ± 0.8	35.6 ± 0.7
	Second peak	394.1 ± 1.2	31.7 ± 1.1
Distill scintillator	First peak	203.7 ± 0.7	31.6 ± 0.7
	Second peak	332.0 ± 1.1	30.0 ± 1.0

Table 5.3: Mean value and sigma of the peaks in the Ncor spectrum for three scintillator samples.

If the peaks were caused by ^{222}Rn, the rate of coincidences as a function of time since the start, should agree with the 3.82 day half-life of ^{222}Rn. The rate of coincidences versus the time since the first run was plotted and is shown in Figure 5.4. An

exponential fit was made and the results are in Table 5.4.

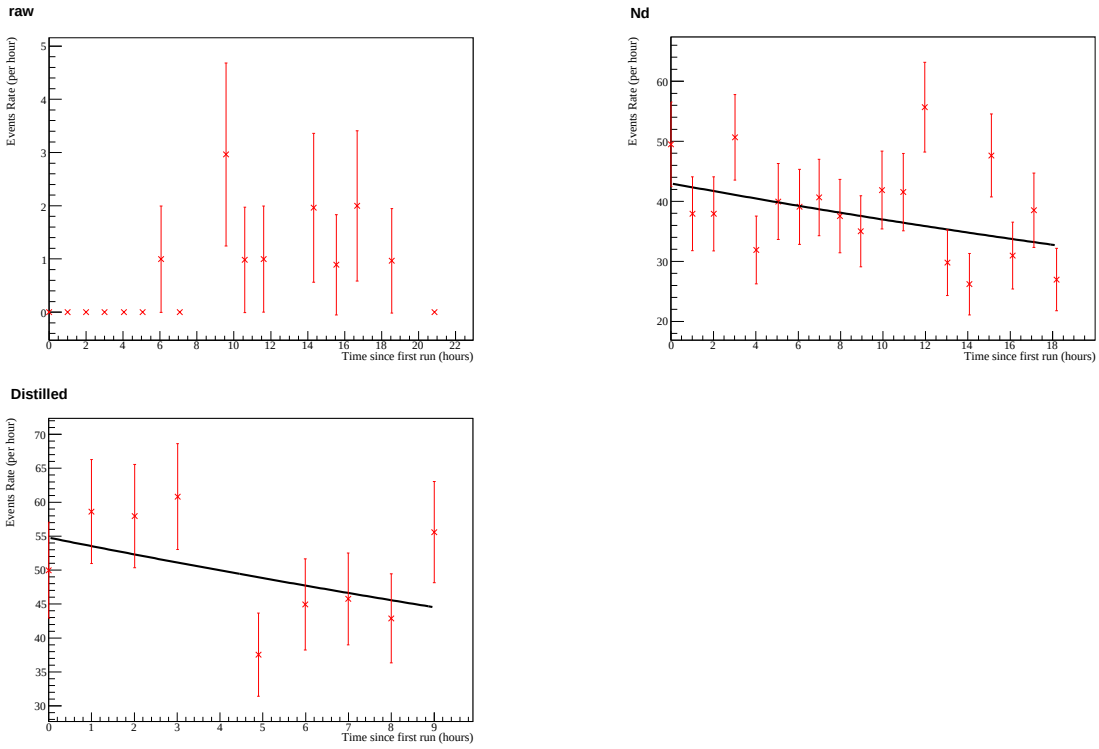

Figure 5.4: Spectrum of coincidence rate versus the time since the first run.

Scintillator	Fitted half-life
Nd-loaded scintillator	1.91 ± 0.85 d
Distilled scintillator	1.26 ± 0.89 d

Table 5.4: The fitted results of β-α coincidence rate versus the β-α time difference for the Nd and distilled scintillator.

Considering that the total running time is short compared with the ^{222}Rn half-life, the fitted half-life has large statistical errors. Again it is impossible to fit the half-life for raw scintillator because of the very low coincidence rate. For the Nd-loaded and distilled scintillator samples, the agreement of results support the assumption that

the peaks came from α decays of ^{222}Rn and its daughters.

5.2.3 Random Coincidence

During the coincidence analysis of a lot of events, there is a possibility that two events selected by the coincidence cut were not part of the real coincidence events. They might fall in the chosen time window by accident. So random coincidences should be taken into account. But because the time window used in the coincidence analysis is 660 μs, the random coincidence rate should be very small.

The random rate of coincidences Γ_a can be calculated with Equation 5.1.

$$\Gamma_a = \Gamma_s^2 \cdot t_c \tag{5.1}$$

Where Γ_s = single event rate, which is the number of all events that pass all the energy cut (like the 50 Nhits cut , DAMN mask and Ncor within $\pm 2\sigma$ of the mean value) over the total live time of all the runs. t_c is a time window of 660 μs.

After all the cuts (except the time cut) were applied to the data, the number of random coincidences N_a can be calculated and shown in Table 5.5.

$$N_a = \Gamma_a \cdot t_L \tag{5.2}$$

Where Γ_a = random rate, t_L = Total live time of all the runs.

Scintillator	Number of random coincidences
Raw scintillator	3.3×10^{-6}
Nd scintillator	0.0054
Distilled scintillator	0.0075

Table 5.5: The expected number of random coincidences for three kinds of scintillator.

The number of random coincidences is very small compared with the number of

β-α coincidence, and therefore did not affect the results of the coincidence analysis.

5.2.4 Position Fit

A reconstructed position of each event was obtained from one of the SNO event fitters. The position of each event is reconstructed using the arrival time of photons observed by the PMTs. The position of reconstructed events for each scintillator type are shown in Figure 5.5, 5.6 and 5.7. An Nhits cut of 100 was applied to select only scintillation events. With such a cut, almost all the events were concentrated where the scintillator bucket was.

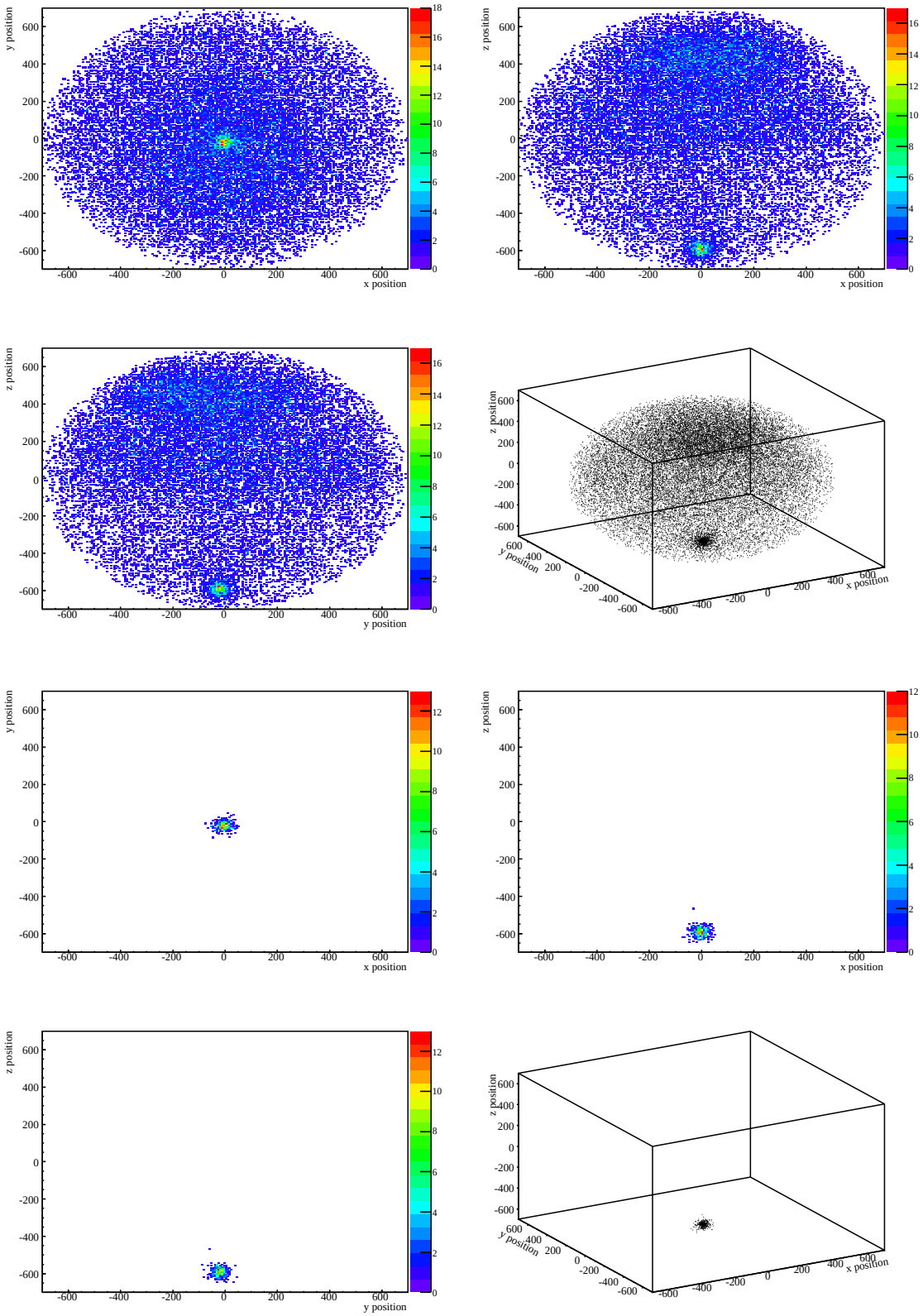

Figure 5.5: The top four plots show the reconstructed positions of all the events before the 100 Nhits cut. The bottom four plots show the reconstructed positions of the events after 100 Nhits energy cut. All are for raw scintillator.

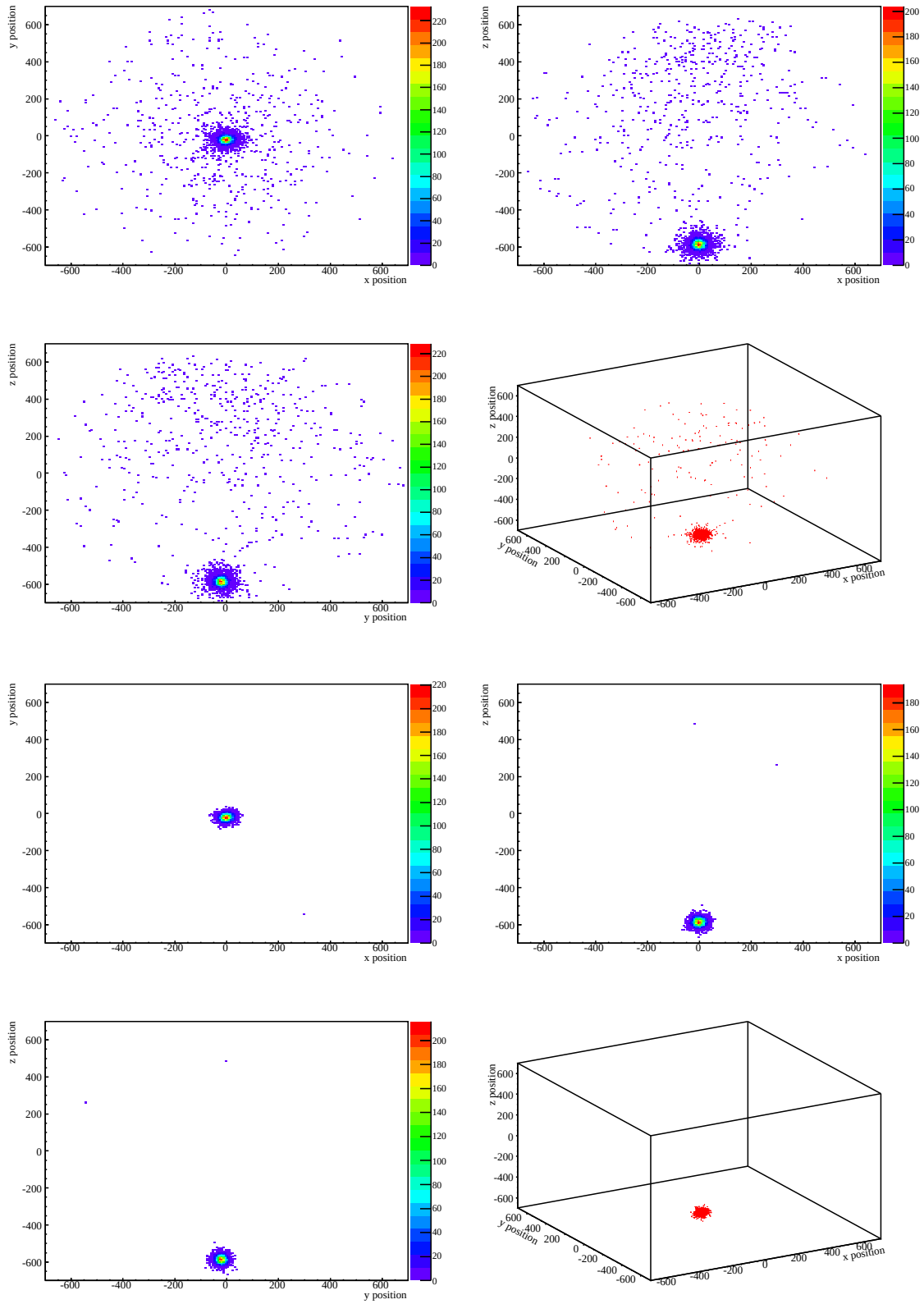

Figure 5.6: The top four plots show the reconstructed positions of all the events before the 100 Nhits cut. The bottom four plots show the reconstructed positions of the events after 100 Nhits energy cut. All are for Nd-loaded scintillator.

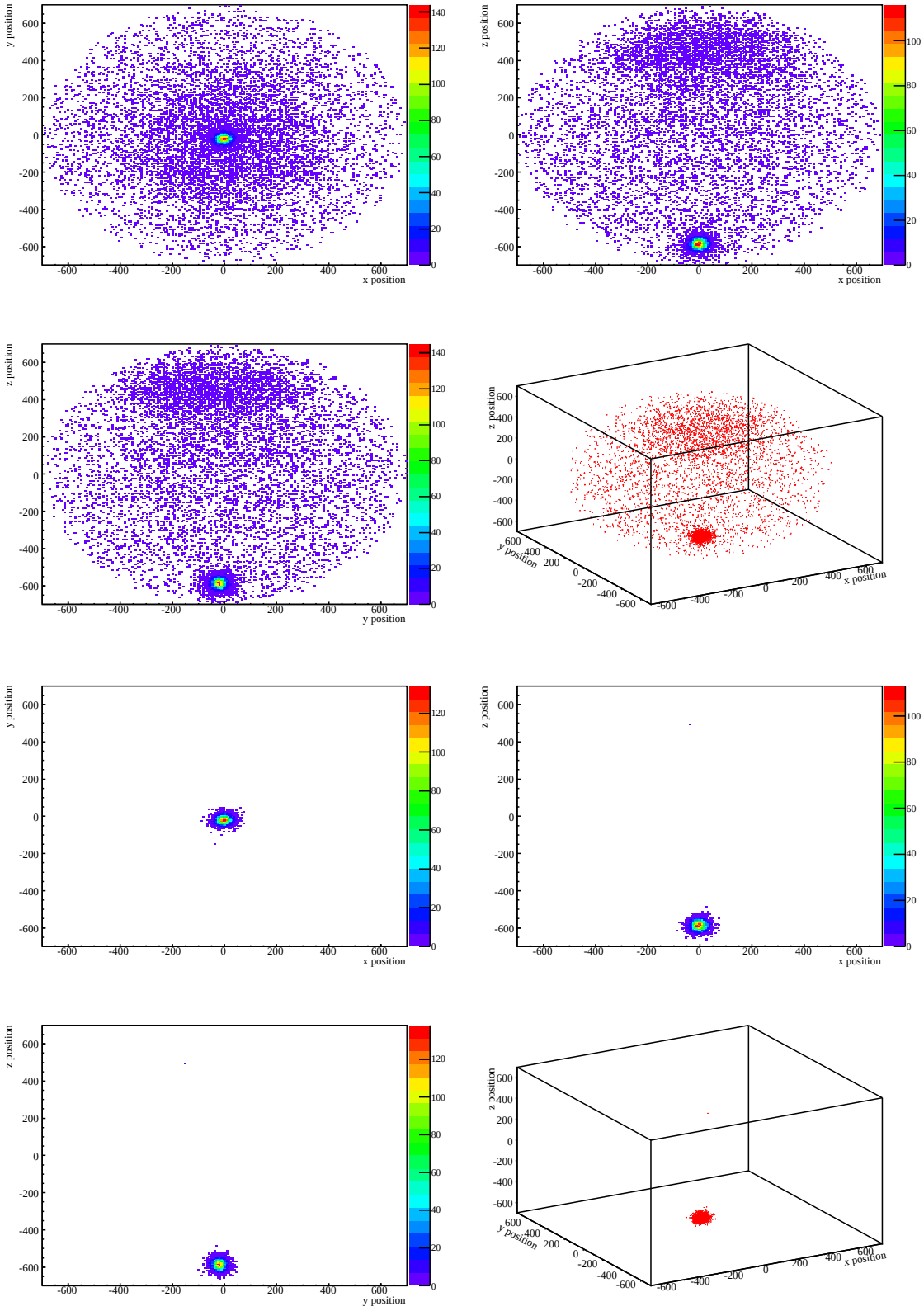

Figure 5.7: The top four plots show the reconstructed positions of all the events before the 100 Nhits cut. The bottom four plots show the reconstructed positions of the events after 100 Nhits energy cut. All are for distilled scintillator.

5.3 Backgrounds from ^{210}Po

As discussed in Chapter 2, the alpha emission from ^{238}U decay chain and ^{232}Th decay chain is another source of radioactive backgrounds. It is useful to explore whether the alpha emission with energy of 5.30 MeV and 138 days half-life from the decay of ^{210}Po in the ^{238}U decay chain is present in the Ncor spectrum of bottom runs.

5.3.1 Background Cut for Alphas from ^{210}Po

To try to distinguish alpha events from ^{210}Po, alpha events from ^{222}Rn decays need to be eliminated from the Ncor spectrum. Also, the beta events in the beta-alpha coincidence can be subtracted. A number of subtractions were applied to the Ncor spectrum of the background in Figure 5.1.

First, alpha events of the beta-alpha coincidence in the second peak need to be subtracted from the Ncor spectrum. They were demonstrated to be emitted by ^{214}Po, the daughter nuclear of ^{222}Rn. To subtract more alpha events from ^{222}Rn decays in the second peak, a larger time window of 1640 μs which is 10 ^{214}Po half live was used to select β-α coincidences. Alpha events above 50 Nhits and with corrected Nhits within 4σ of the mean value of the fitted second peak were subtracted for Nd-loaded and distilled scintillators, shown in Figure 5.8.

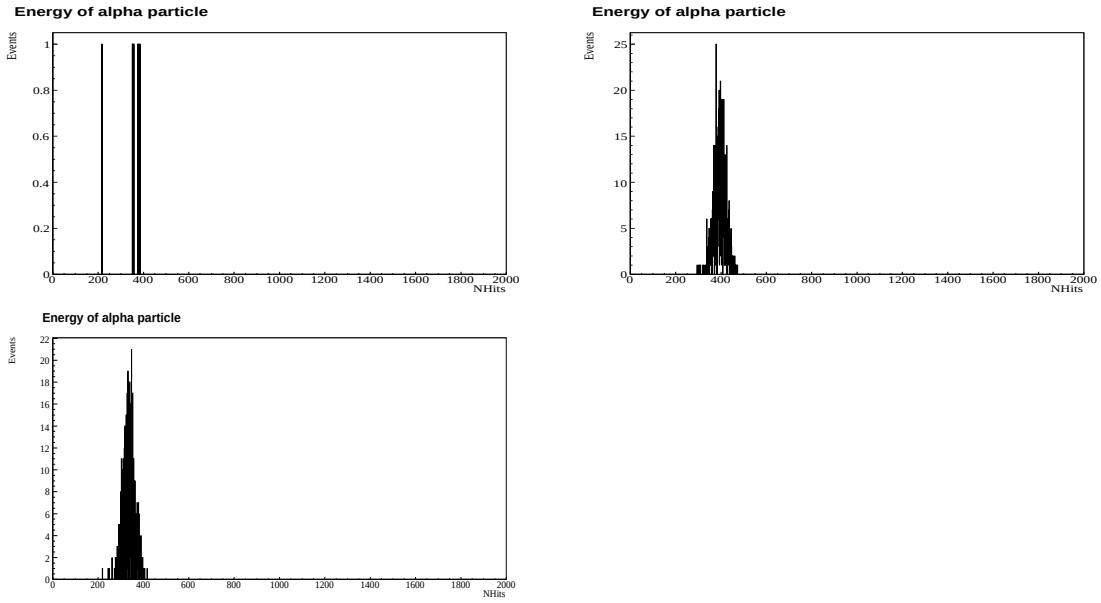

Figure 5.8: This plot shows alpha events from the beta-alpha coincidence for raw, Nd-loaded and distilled scintillators from top left.

Second, alpha events from decays of ^{222}Rn which are a cause of the first peak need to be subtracted. They are the 5.59 MeV alphas from the direct decay ^{222}Rn with a half-life of 3.8 days and the 6.11 MeV alphas from the decay of ^{218}Po with a half-life of 3.10 minutes. After Rn exposure, in the scintillator, ^{222}Rn, ^{218}Po, ^{214}Pb, ^{214}Bi will be in equilibrium but it takes about 3 hours to establish, if there was anything that started out of equilibrium. The concentration of ^{222}Rn and ^{218}Po is approximately twice as much as that of ^{214}Bi, if ^{222}Rn, ^{218}Po, ^{214}Pb, ^{214}Bi are in equilibrium. Thus, the number of 5.59 MeV alphas from the decay of ^{222}Rn and 6.11 MeV alphas from the decay of ^{218}Po which caused the first peak should be twice of the number of 7.83 MeV alphas from the decay of ^{214}Po which caused the second peak. The number of alpha events with corrected Nhits within 4σ of the mean value of the fitted second peak was counted and shown in Table 5.6. A Gaussian peak with the same mean value and

Scintillator	Number of coincidences
Raw	9
Nd	741
Distilled	616

Table 5.6: Alpha events from from ^{214}Bi-^{214}Po coincidences for three kinds of scintillator.

sigma as the first peak was simulated, whose integration is equal to twice the number of coincidences. This Gaussian peak then was subtracted from the Ncor spectrum. Figure 5.9 shows the simulated alpha Gaussian peak for different scintillators.

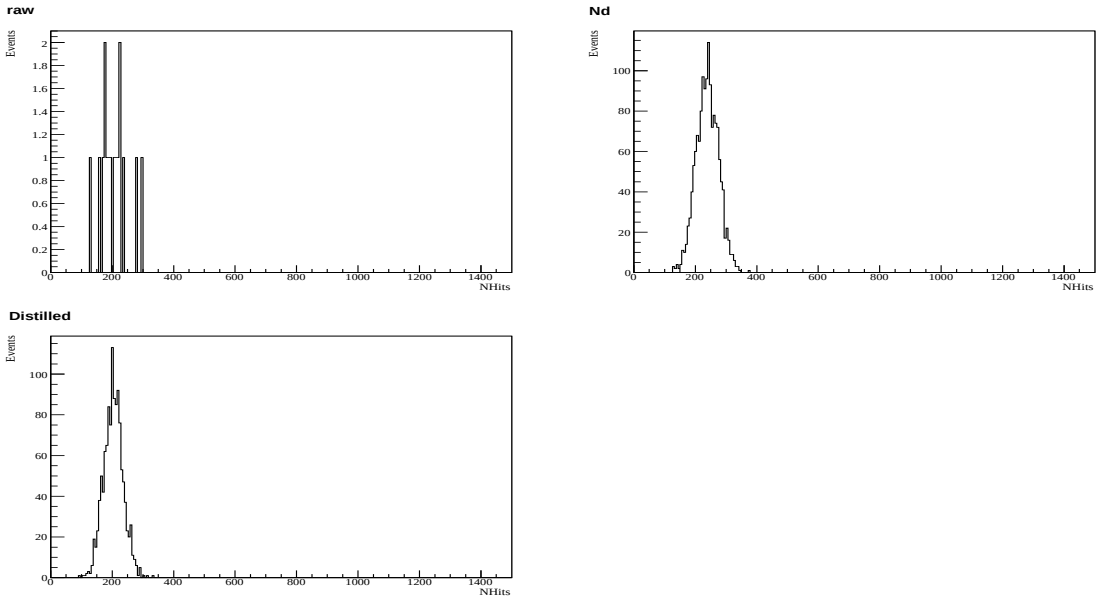

Figure 5.9: These plots show the simulated Gaussian peaks for the raw scintillator with the values of mean and sigma of the first peak in Table 5.3, whose integration is equal to twice the number of coincidences.

Third, the beta spectrum was subtracted from the total Ncor spectrum. A time window of 1640 μs was used to select more β events in the beta-alpha coincidences which had energies above 50 Nhits. The beta spectrum is shown in Figure 5.10.

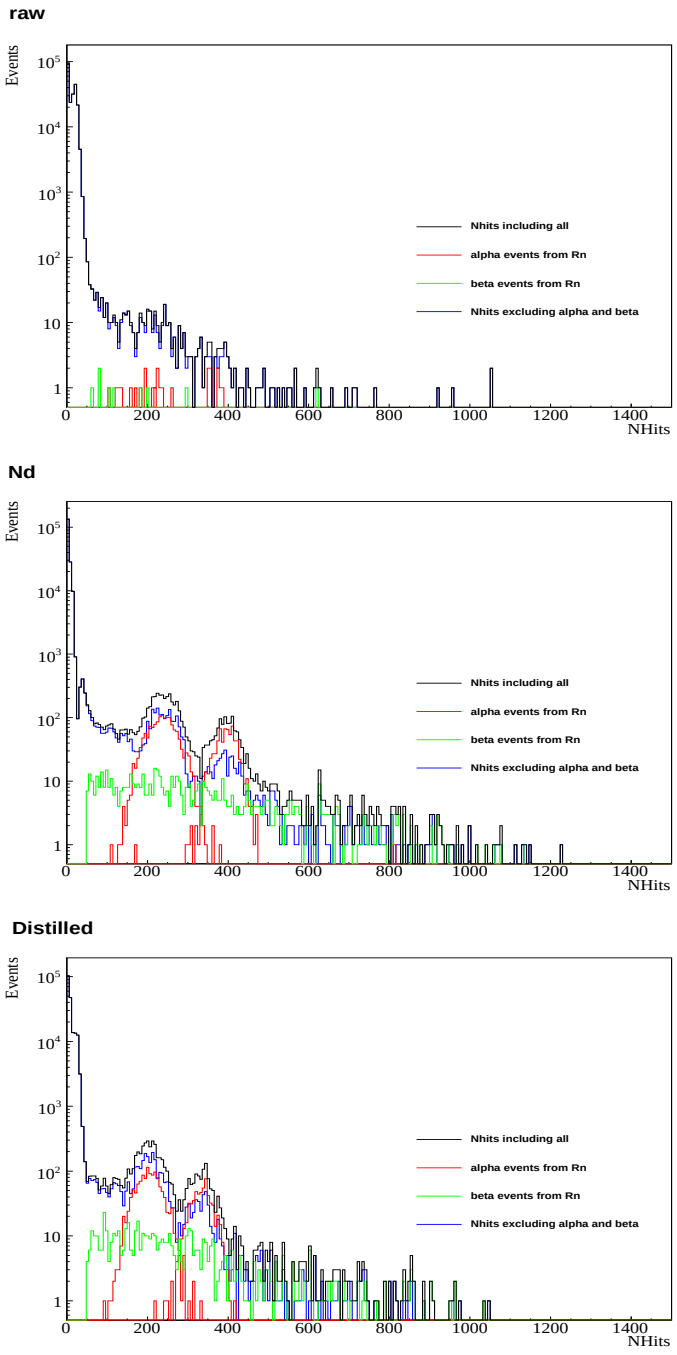

Figure 5.10: Top: raw scintillator; middle: Nd-loaded scintillator; bottom: distilled scintillator. The black curves are the original Ncorrected spectra. Red curves are alpha events from coincidences and calculated for the first peak. Green curves are beta events from coincidences. Blue curves have alpha and beta contributions subtracted.

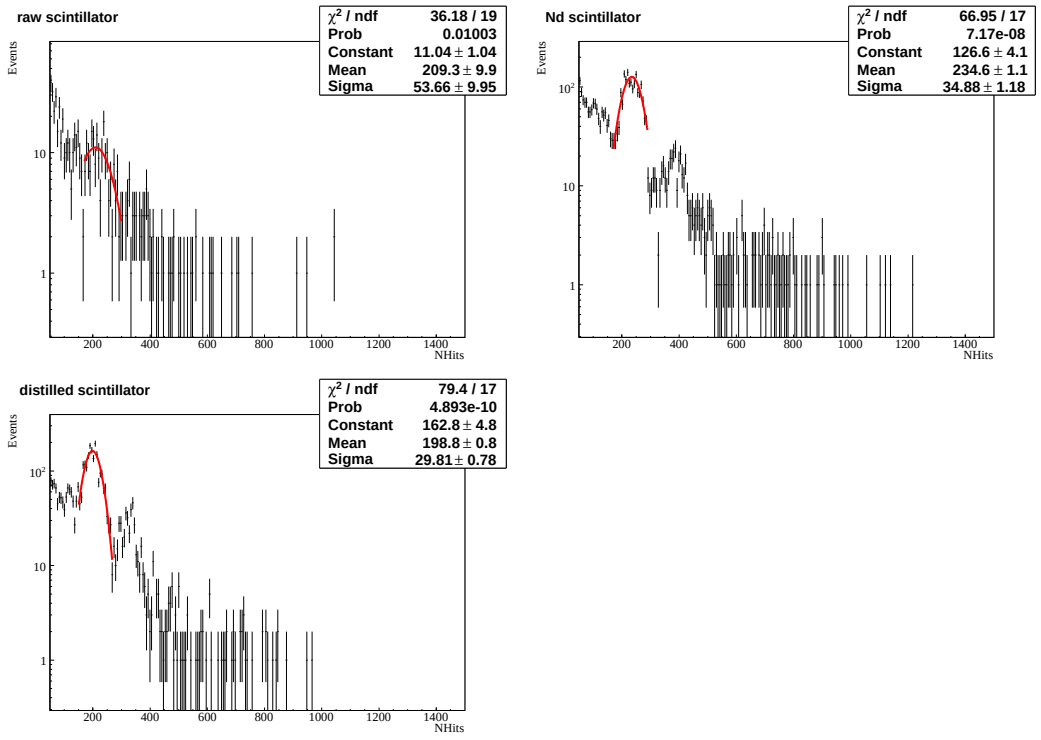

Figure 5.11: These plots show the background-subtracted events for raw, Nd-loaded and distilled scintillators. A Gaussian fit was made to the first peak.

Figure 5.11 shows the events after backgrounds from the decays of ^{222}Rn and Cherenkov events have been subtracted. A Gaussian fit was made to the first peak and the values shown in Table 5.7.

Scintillator	Peak	Mean(Nhits)	Sigma(Nhits)
Raw scintillator	First peak	209.3 ± 9.9	53.7 ± 10.0
Nd-loaded scintillator	First peak	234.6 ± 1.1	34.9 ± 1.2
Distill scintillator	First peak	198.8 ± 0.8	29.8 ± 0.8

Table 5.7: Mean value and sigma of the first peaks in the background spectrum excluding beta and alpha events from decays of ^{222}Rn.

From Figure 5.11, there are still small second peaks in the plots. It is difficult to exclude all of the beta and alpha events from the decays of ^{222}Rn because the

identification cuts are not 100% efficient. If good coincidences were mistakenly cut by the DAMN mask (the SNO detector data acquisition was less stable during the scintillator bucket runs compared to the normal running of SNO), then coincidences might be missed.

The finite inefficiency of the time window cut can be calculated. Though the 10 half-life window is long, the SNO data acquisition cannot separate events closer than the 400 ns trigger window. Then, ^{214}Po alpha events happening earlier than 400 ns will be combined with ^{214}Bi beta events. These will not produce an event in the second peak but will produce events with the sum of the alpha and beta energies (and in any case, the coincidence will be missed). This inefficiency can be calculated by integrating events from 0 to 0.4 μs in the decay spectrum of ^{214}Po:

$$1 - exp(-0.4(ln2/164)) = 0.17\%. \tag{5.3}$$

The largest part of the inefficiency comes from beta events with energy lower than the Nhits > 50 threshold. These will not pass the coincidence analysis and the later alpha decays will show up in the second peak. An estimate of the number of beta events below 50 Nhits was done by summing up the number of beta events from 50 to 200 Nhits and then dividing the sum by 3. The fraction of this number divided by the total number of identified beta events is an estimate of the inefficiency, which is 7.4% for raw LAB, 10.9% for Nd-loaded LAB and 13.6% for distilled LAB.

Scintillator	Total inefficiency	Corrected number of coincidences
Raw LAB	7.6%	10
Nd-loaded LAB	11.1%	834
Distill LAB	13.8%	715

Table 5.8: Total inefficiency by combining the inefficiency from 50 Nhits cut with inefficiency from time window cut and the corrected number of coincidences.

After applying the total inefficiency, the number of coincidences can be corrected, shown in Table 5.8. The two simulated alpha peaks using the corrected number of coincidences were subtracted together with the subtraction of beta events, shown in Figure 5.12.

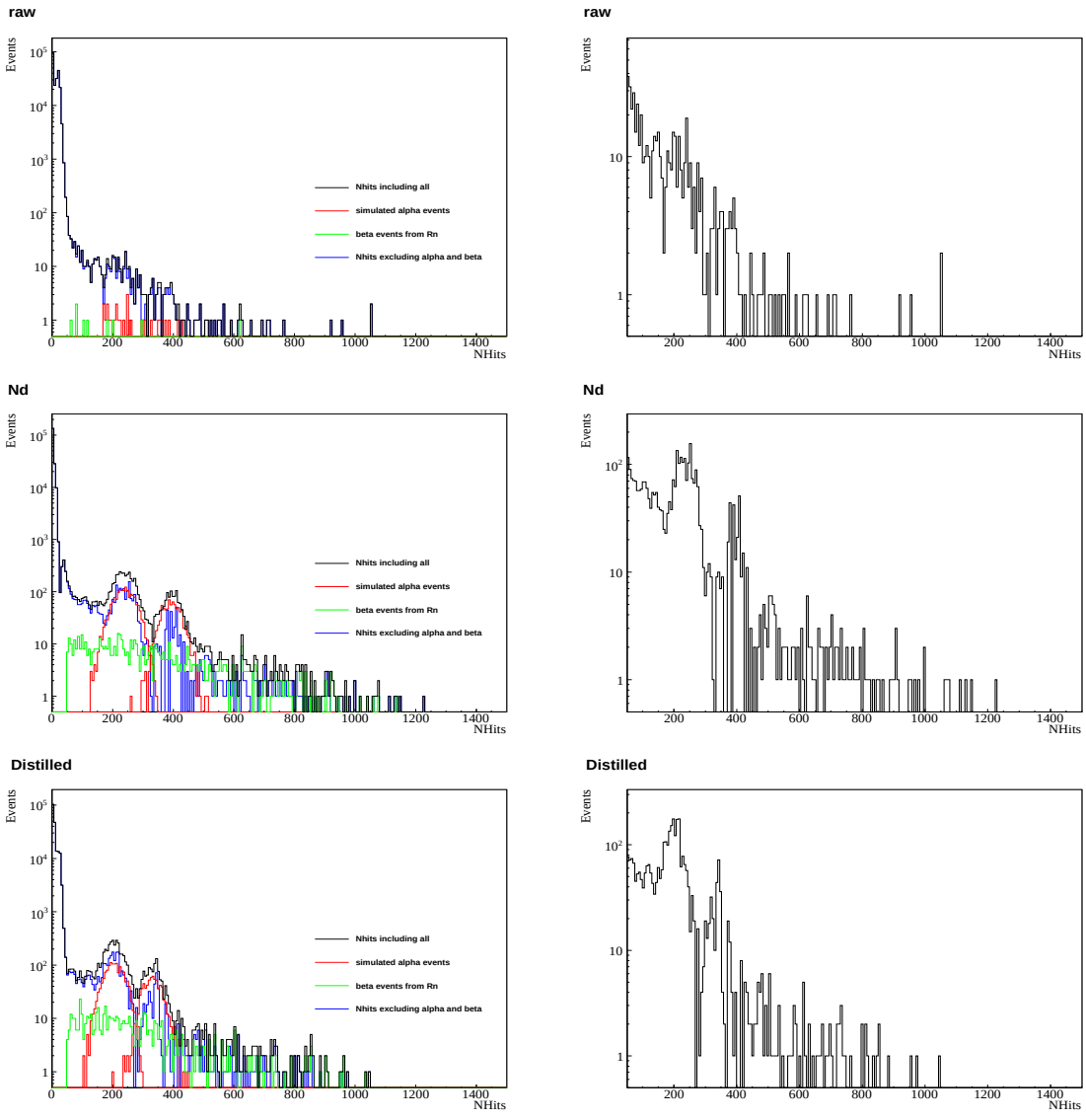

Figure 5.12: These plots show the background-subtracted events for raw, Nd-loaded and distilled scintillators using the corrected number of coincidences.

After estimating the correction of inefficiency, more coincidences from Rn were subtracted. It is difficult to subtract all the events from Rn. Using values from Table 5.7, the number of alphas left over in the first peak can be obtained by summing up events within $\pm 2\sigma$ of the mean value of the first peak and then dividing by the total running time (the half-life of ^{210}Po is much larger than the running time) to get the alpha rate. This is an estimate of the upper limit on the amount of ^{210}Po alphas in the scintillator bucket data, shown in Table 5.9.

Scintillator	Activity (mBq)
Raw scintillator	<9.0
Nd-loaded scintillator	<17.8
Distilled scintillator	<24.9

Table 5.9: The upper limit on the activities of ^{210}Po in the scintillators.

5.4 Backgrounds from Gamma Rays

5.4.1 Compton Edge of Gamma Rays

As discussed in Chapter 2, backgrounds from gamma rays needs to be identified in neutrino experiments. Common and important gamma backgrounds in SNO+ are the 2614 keV gamma from the decay of ^{208}TI and the 1460 keV gamma from the decay of ^{40}K. When these gammas pass through a small volume of scintillator (like the scintillator bucket) they can be observed by their Compton edges. The energy of those Compton edges are listed in Table 5.10.

Gamma rays	Compton Edge
^{40}K 1460keV	1.24 MeV
^{208}TI 2614keV	2.41 MeV

Table 5.10: The energy of Compton edges for important gamma rays from natural radioactivity.

5.4.2 Spectrum of Gamma Backgrounds in the Scintillator Bucket

When the scintillator bucket was deployed in the centre of the AV, gamma backgrounds originating from the scintillator, the bucket source hardware, and the water inside the AV will produce events. When the scintillator bucket was deployed at the bottom of the AV, there might be increased sensitivity to external gamma backgrounds from radioactivity in the AV and the outside water. Analysis of central runs were carried out using the same subtractions of alpha and beta events from decays of ^{222}Rn described in Section 5.3. The subtraction of Rn backgrounds is shown in Figure 5.13.

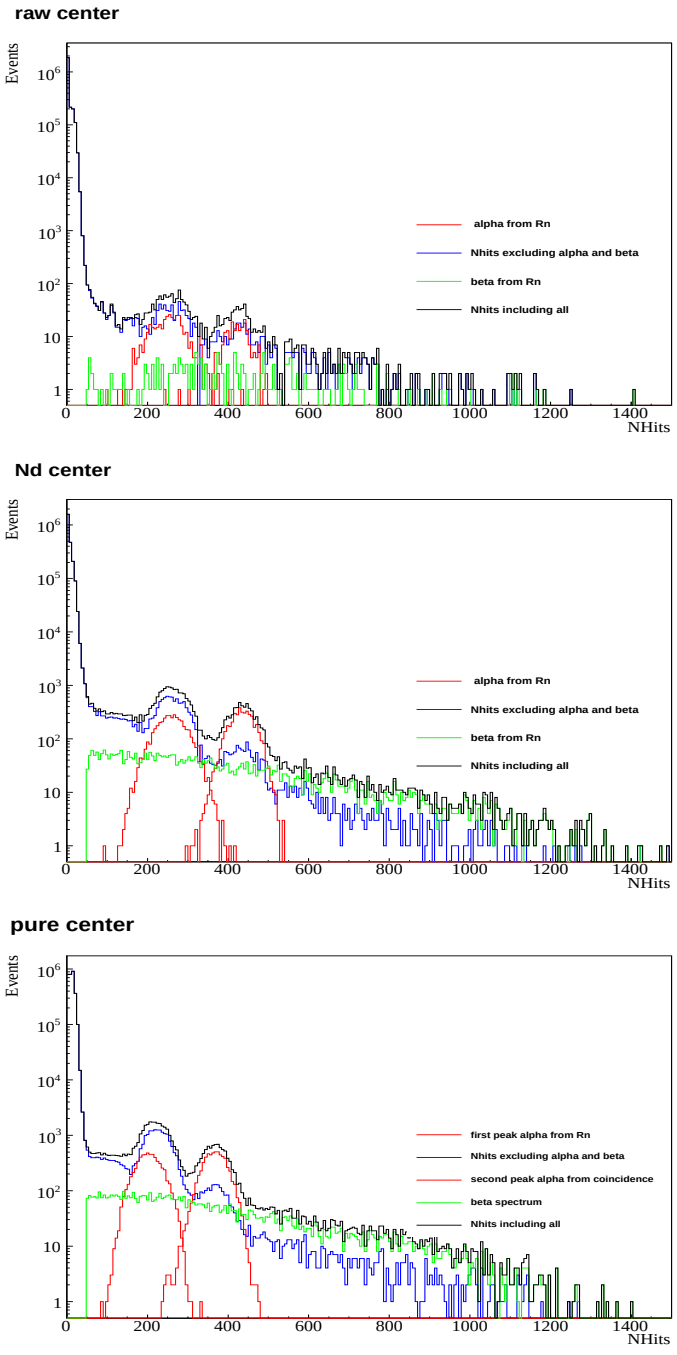

Figure 5.13: Top: raw scintillator; middle: Nd-loaded scintillator; bottom: distilled scintillator, all deployed in the centre of the AV. Black curves are data, red curves backgrounds from alphas, green curves backgrounds from betas, and blue curves with those backgrounds subtracted.

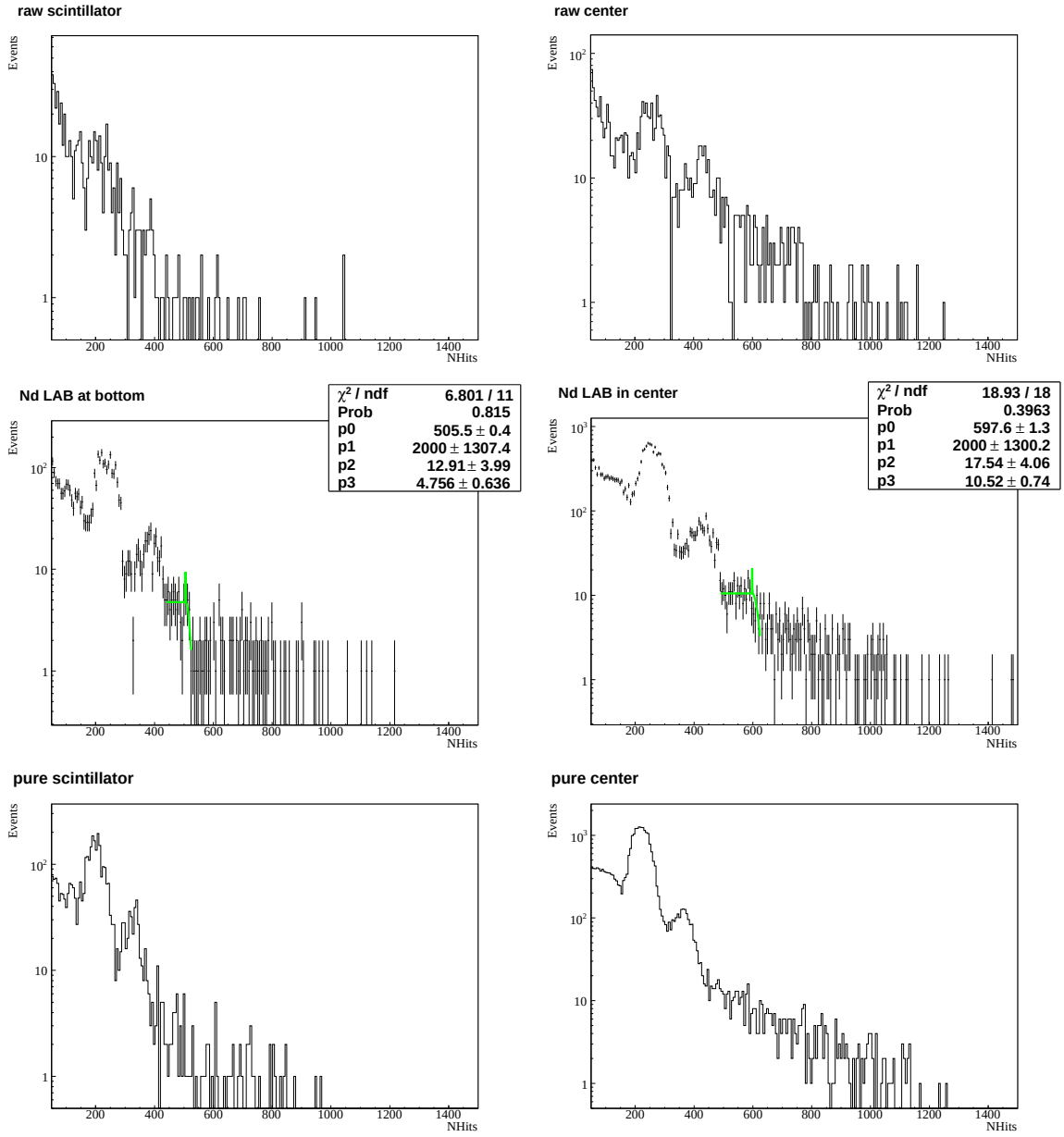

Figure 5.14: Background-subtracted spectra for bottom runs of the scintillator bucket (left) and central runs (right). An attempt to fit a Compton edge for Nd-loaded scintillator in both bottom and central runs is shown in green.

From Figure 5.14, a small Compton edge can be seen at about 500 Nhits in the

spectrum of Nd-loaded scintillator in bottom runs and at about 600 Nhits in the spectrum of Nd-loaded scintillator in central runs. But no clear edge can be seen for raw scintillator and distilled scintillator. The same Equation 4.10 which is a construction of a step function and a Gaussian was used to fit the Compton edge. The Nhits of the fitted edge is shown in Table 5.11.

Position	Fitted edge(Nhits)	Conversion(Nhits/MeV)	Compton edge(MeV)
Bottom	505.5 ± 0.4	388.6 ± 2.1	1.30 ± 0.01
centre	597.6 ± 1.3	447.7 ± 2.8	1.33 ± 0.01

Table 5.11: The comparison of fitted edges in the Nd-loaded LAB background spectrum and the calculated energy of fitted Compton edges in both central and bottom runs.

As shown in Table 4.4, when the scintillator bucket was deployed in the centre, the conversion of Nhits and energy for Nd-loaded scintillator is (447.7 ± 2.8) Nhits/MeV. By comparing the mean values of the second peak of bottom and central background spectra, the Nhits/MeV in the bottom runs is 13.2% lower than in the centre for Nd scintillator [40]. After applying the corrected conversion, the energy of the Compton edge is shown in Table 5.11. From Table 5.11, the energy of fitted Compton edges for Nd-loaded scintillator in both central and bottom background spectrum roughly agree with the energy of the theoretical Compton edge of the 1460 keV gamma ray from ^{40}K. However, from the background spectrum, the other Compton edge of 2613 keV gamma ray from ^{208}TI cannot be identified.

5.4.3 Simulations of Gamma Backgrounds

To compare with the actual backgrounds of gamma rays, Monte Carlo simulations in RAT with corrected light yield were performed. The scintillator bucket was set to

different positions as shown in Table 5.1 at the bottom or in the centre of the acrylic vessel for raw and Nd-loaded scintillator. 1.46 MeV gamma rays were generated from different positions to simulate the internal and external backgrounds.

Gamma Rays Generated in the Scintillator

To simulate the internal backgrounds from gamma rays, 5000 photons with a energy of 1.46 MeV were generated in the centre of the scintillator bucket. The simulation of gamma rays of ^{40}K for different kinds of scintillator is shown in Figure 5.15.

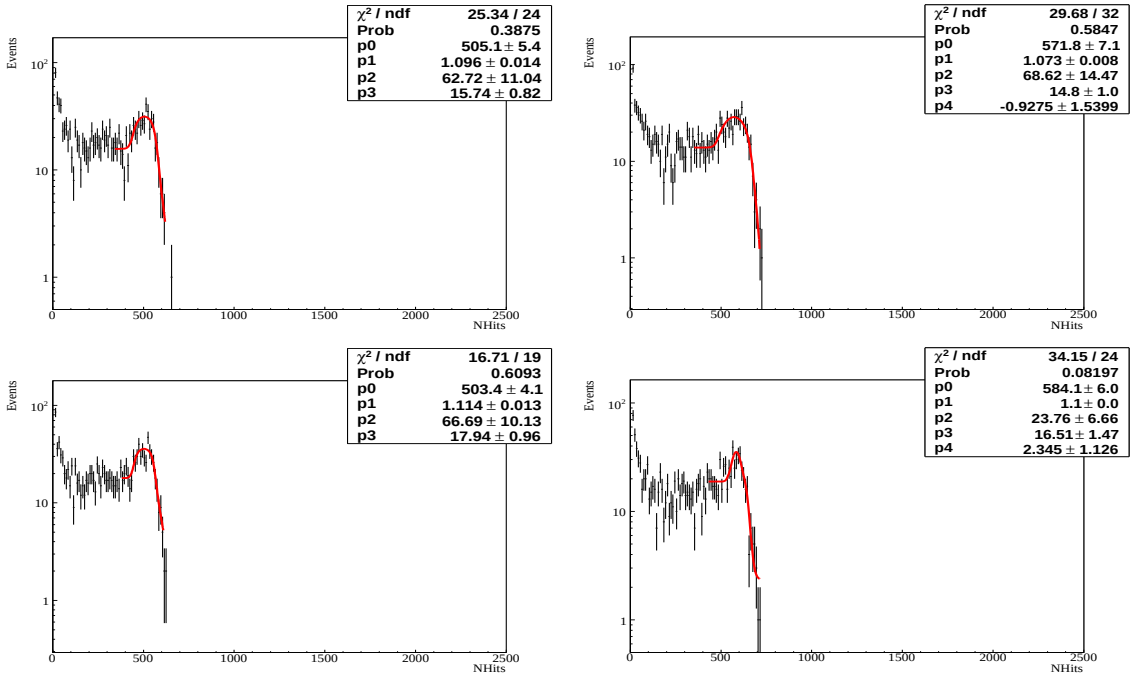

Figure 5.15: The simulation and the edge fit of 5000 1.46 MeV gamma in the centre of scintillator bucket which was set in the centre or at the bottom. Top left: bucket at the bottom with raw LAB; top right: bucket in the centre with raw LAB; bottom left: bucket at the bottom with Nd-loaded LAB; bottom right: bucket in the centre with Nd-loaded LAB.

From these simulated spectra for 1.46 MeV gammas, Compton edges at about

500 Nhits can be seen. The same step-fit was applied to the simulated spectrum and the fitted results of the Compton edges are shown in Table 5.12. For raw scintillator, there was no obvious step in the spectra, so the comparison is between Monte Carlo and scintillator bucket data is more relevant for the Nd-loaded scintillator.

	Raw LAB	Nd-loaded LAB
Fitted edge in data(Nhits)	N/A	505.5 ± 0.4
Fitted edge in MC(Nhits)	505.1 ± 5.4	503.4 ± 4.1
Constant before the slope down in data	N/A	4.8 ± 0.6
Constant before the slope down in MC	15.7 ± 0.82	17.9 ± 0.96

Table 5.12: The comparison of the energy of fitted Compton edges in the background spectrum and the energy of Compton edges in MC, and the comparison of the number of gammas before the slope down in data and MC for bottom runs.

	Raw LAB	Nd-loaded LAB
Fitted edge in data(Nhits)	N/A	597.6 ± 1.3
Fitted edge in MC(Nhits)	571.8 ± 7.1	584.1 ± 6.0
Constant before the slope down in data	N/A	10.5 ± 0.7
Constant before the slope down in MC	14.8 ± 1.0	16.5 ± 1.5

Table 5.13: The comparison of the energy of fitted edge in the background spectrum and the energy of Compton edge in MC and the comparison of the number of gamma before the slope down in data and MC for central runs.

From Table 5.12 and 5.13, The fitted Compton edges in MC agree with the fitted Compton edges in the gamma background for Nd-loaded scintillator in both central and bottom runs. These observations suggest the contribution of the decay of ^{40}K to the backgrounds measured by the scintillator bucket.

For central runs, from the comparison of the step normalization before the slope down in MC and data for the Nd-loaded scintillator, the number of gammas produced

by gammas in the scintillator in the real background is (63.6±0.16%)% of the gammas produced in MC. Because 5000 initial gammas were generated in MC, (3186 ± 508) gammas are calculated to be produced from the decay of ^{40}K. 75 good central runs were analyzed for Nd-loaded scintillator and each run lasted about one hour. So the rate of gammas when the bucket was deployed in the centre was $(42.5 \pm 6.8)/hr$.

If the internal gammas were all from the scintillator in the bucket, the activity and concentration of ^{40}K in the scintillator could be obtained. Table 5.14 shows the gamma activity of the Nd-loaded scintillator samples measured by the SNOLAB Ge detector [41].

Sample	Mass(g)	Activity(mBq/kg)	Concentration(ppm)
Ge detector	880.1	< 7.01	< 0.22
Bucket	876	13.5 ± 2.2	0.44 ± 0.07

Table 5.14: The comparison of the activity of ^{40}K and concentration of K in the Nd-loaded scintillator as measured by the SNOLAB Ge detector [41] and in the bucket deployed in the centre (1 Bq ^{40}K/kg = 32300 ppb K).

With this calculation, the activity of gammas in the scintillator bucket is more than twice that in Nd-loaded scintillator counted in the SNOLAB Ge detector which indicates some contribution to this signal from hardware components of the bucket source and/or the internal water surrounding the bucket.

For bottom runs, (1475 ± 394) gammas are calculated to be from the decay of ^{40}K, by comparing with 5000 initial gammas generated in the MC. 19 good bottom runs were analyzed for the Nd-loaded scintillator and each run lasted about one hour. So data from the scintillator bucket at the bottom suggest a rate of $(77.6 \pm 20.7)/hr$. The gamma rate at the bottom is about 80% higher than in the centre, which means there were gammas from ^{40}K contained in the acrylic vessel and external water that

contributed to the backgrounds measured with the bucket deployed at the bottom.

Gamma Rays Generated in the Acrylic Vessel

To examine the external backgrounds of gamma rays from the acrylic vessel, another MC simulation in RAT was performed. The scintillator bucket was set to the same position at the bottom as shown in Table 5.1. 50000 1.46 MeV gammas were generated in RAT at the position of (0, 22.49, -603.38) cm which was inside the material of the Acrylic Vessel. The simulation of gamma rays of ^{40}K for the raw and Nd-loaded scintillator is shown in Figure 5.16.

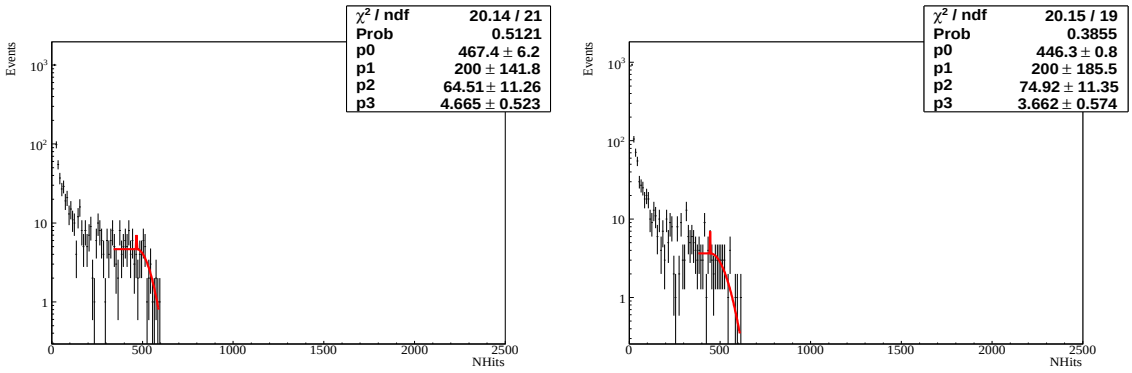

Figure 5.16: The simulation and the edge fit of 50000 1.46 MeV gamma generated in the Acrylic Vessel. The left plot is for raw scintillator and the right plot is for Nd-loaded scintillator in RAT

Scintillator	Gamma position	Fitted edge(Nhits)	Slope constant in MC
Raw	in the AV	467.4 ± 6.2	4.7 ± 0.5
Raw	in the scintillator	505.1 ± 5.4	15.7 ± 0.8
Nd-loaded	in the AV	446.3 ± 0.8	3.7 ± 0.6
Nd-loaded	in the scintillator	503.4 ± 4.1	17.9 ± 1.0

Table 5.15: The fitted results of simulated 50000 1.46 MeV gammas emitted from inside of the Acrylic Vessel compared with 5000 gammas simulated in the centre of the scintillator bucket for raw and Nd-loaded scintillator.

From Table 5.15, for the raw scintillator, the generated gammas in the Acrylic Vessel had 7.5% less visible energy compared to the gammas generated from the internal. For the Nd-loaded scintillator, the generated gammas in the acrylic vessel had 11.3% less visible energy compared to the gammas generated from the internal. From comparison of the constant of the slope, gammas emitted from the Acrylic Vessel are only approximately 2% as likely to be detected in this analysis compared to gammas originating from the scintillator.

Gamma Rays Generated in the External Water

Gamma rays were also generated for activity in the external water outside the AV. A Monte Carlo simulation of 50,000 1.46 MeV gammas was run. In these simulations, there were virtually no events simulated that registered energy deposit in the scintillator bucket. This is because many millions of events would need to be simulated in the water in order to have enough that would hit the scintillator bucket. Without going further with this study, these were neglected and then comparison of bottom runs with central runs become just an estimate of gamma activity in the Acrylic Vessel.

For Nd-loaded scintillator, the gamma rate in the bottom runs is calculated to be $(77.6 \pm 20.7)/hr$ and the gamma rate in the central runs is calculated to be $(42.5 \pm 6.8)/hr$. The difference in rate is supposed to be a contribution from the Acrylic Vessel. From the Monte Carlo simulation, ^{40}K gammas from the AV are approximately 2% as likely to be detected compared with gammas from the scintillator. Thus the activity level in the AV near where the scintillator bucket was deployed can be estimated to be (487 ± 209) mBq.

5.5 Summary

In this chapter, the quantities of radioactive backgrounds for SNO+ experiment were studied by using background spectra from the scintillator bucket deployed in the centre and at the bottom of the Acrylic Vessel. From the ^{214}Bi-^{214}Po coincidence analysis which are daughter nuclei of ^{222}Rn, beta and alpha rays from decays of ^{222}Rn in the scintillator were shown to be the primary cause the radioactive backgrounds seen in the scintillator bucket runs. ^{210}Po, a daughter of ^{238}U was searched for and the amount constrained. By comparing simulations and background data from the scintillator bucket, ^{40}K was identified in the Nd-loaded liquid scintillator. The contribution of ^{40}K in the scintillator and from ^{40}K activity in the Acrylic Vessel were estimated.

Chapter 6

Conclusions

These are the conclusions from my studies with the scintillator bucket measurements and comparison to simulations:

1) Nd-loaded scintillator was observed to have 7.8% lower light yield than unloaded scintillator.

2) Distilled scintillator was measured to have 18.4% lower light yield than the undistilled scintillator however its light yield should have been at least the same as the undistilled. Subsequent investigations (not part of my work) determined the distilled scintillator sample was contaminated during preparation/filling and that quenched the light output.

3) By comparing to a model of the scintillator bucket in RAT with data from the scintillator bucket, the light yield value in the simulation was adjusted from 12,000 photons/MeV to 11,111 photons/MeV for the raw scintillator and 11,400 for Nd-loaded scintillator. The incorrect higher light yield for Nd-loaded scintillator in Monte Carlo is due to the inadequate characterization of the optical properties of this scintillator, as coded in RAT which need to be re-examined.

4) Internal radioactivities during the scintillator bucket deployments were analyzed. Radon was observed to be the main background in the scintillator bucket data. This was demonstrated by ^{214}Bi-^{214}Po coincidence analysis.

5) Using the coincidence analysis to estimate the amount of radon, it can be subtracted from the background spectra. Then, upper limits on the amount of ^{210}Po alpha events were 9.0 mBq for the raw scintillator, 17.8 mBq for the Nd-loaded scintillator and 24.9 mBq for the distilled scintillator.

6) Again, with radon backgrounds subtracted, the spectra for the Nd-loaded scintillator shows a possible Compton edge from the ^{40}K gamma ray of 1.46 MeV. An estimate of the rate of this gamma ray if it came from the Nd-loaded scintillator was 13.5 ± 2.2 mBq/kg. Comparing this to measurements of the ^{40}K from Ge counting at SNOLAB shows that there was likely some contribution to this signal from hardware components of the bucket source and/or the internal water surrounding the bucket.

7) By comparing background spectra with the bucket deployed at the centre with the bucket deployed at the bottom, a limit on the amount of ^{40}K in the Acrylic Vessel near where the scintillator bucket was deployed of (487 ± 209) mBq was obtained.

Bibliography

[1] C.L. Cowan Jr. and F. Reines. Detection of the Free Neutrino: A Confirmation. *Science*, 124:103, 1956.

[2] V. Gribov and B. Pontecorvo. Neutrino Astronomy and Lepton Charge. *Phys. Lett. B*, 28:493, 1969.

[3] S. Eidelman et al. (Particle Data Group). The Review of Particle Physics. *Phys. Lett. B*, 592:1, 2004.

[4] N. Okamura M. Honda, Y. Kao and T. Takeuchi. A Simple Parameterization of Matter Effects on Neutrino Oscillations. *arXiv:hep-ph/0602115*, 2006.

[5] Q. R. Ahmad et al. (SNO Collaboration). Measurement of Day and Night Neutrino Energy Spectra at SNO and Constraints on Neutrino Mixing Parameters. *Phys. Rev. Lett.*, 89:011302, 2002.

[6] S.N. Ahmed et al. (SNO Collaboration). Measurement of the Total Active ^{8}B Solar Neutrino Flux at the Sudbury Neutrino Observatory with Enhanced Neutral Current Sensitivity. *Phys. Rev. Lett.*, 92:181301, 2004.

[7] K. Eguchi et al. (KamLAND Collaboration). First Results from KamLAND:

Evidence for Reactor Antineutrino Disappearance. *Phys. Rev. Lett.*, 90:021802, 2003.

[8] Y. Fukuda et al. (The Super-Kamiokande Collaboration). Evidence for Oscillation of Atmospheric Neutrinos. *Phys. Rev. Lett.*, 81:1562–1567, 1998.

[9] M.H. Ahn et al. (The K2K Collaboration). Measurement of Neutrino Oscillation by the K2K Experiment. *Phys. Rev. D*, 74:072003, 2006.

[10] P. Adamson et al. (The MINOS Collaboration). Measurement of Neutrino Oscillations with the MINOS Detectors in the NuMI Beam. *Phys. Rev. Lett.*, 101:131802, 2008.

[11] M. Apollonio et al. Limits on Neutrino Oscillations from the CHOOZ Experiment. *Phys. Lett. B*, 466:415–430, 1999.

[12] B. Aharmim et al. (The SNO Collaboration). Low-energy-threshold Analysis of the Phase I and Phase II Data Sets of the Sudbury Neutrino Observatory. *Phys. Rev. C*, 81:055504, 2010.

[13] C. Currat. Measuring Cosmic Ray and Atmospheric Neutrinos in the Sudbury Neutrino Observatory. The American Physical Society's 2004 Meeting of the Division of Particles and Fields, August 2004. Available online at http://sno.phy.queensu.ca/talks/2004.html.

[14] H. Bethe. Energy Production in Stars. *Phys. Rev.*, 55:103(L), 1939.

[15] J.N. Bahcall. Neutrinos from the Sun. *Scientific American*, 221:28–37, 1969.

[16] A.J. Wright. *Robust Signal Extraction Methods and Monte Carlo Sensitivity Studies for the Sudbury Neutrino Observatory and SNO+ Experiments.* PhD thesis, Queen's Unversity, 2009.

[17] R. Davis et al. Search for Neutrinos from the Sun. *Phys. Rev. Lett.*, 20:1205–1209, 1968.

[18] S. Fukuda et al. Determination of Solar Neutrino Oscillation Parameters Using 1496 Days of Super-Kamiokande-I Data. *Phys. Lett. B*, 539:179–187, 2002.

[19] J. Boger et al. (SNO Collaboration). The Sudbury Neutrino Observatory. *Nucl. Inst. Meth.*, A449:172, 2000.

[20] H.H. Chen. Direct Approach to Resolve the Solar-Neutrino Problem. *Phys. Rev. Lett.*, 55:1534–1536, 1985.

[21] S.P. Mikheyev and A.Y. Smirnov. Resonant Amplification of ν Oscillations in Matter and Solar-Neutrino Spectroscopy. *Nuovo Cimento*, 9C:17, 1986.

[22] E. Majorana. *Nuovo Cimento*, 14:171–184, 1937.

[23] J. Schechter and J.W.F. Valle. Neutrinoless Double-β Decay in SU(2) $\times$ U(1) Theories. *Phys. Rev. D*, 25:2951–2954, 1982.

[24] C. Giunti and C.W. Kim. *Fundamentals of Neutrino Physics and Astrophysics.* Oxford, 2007.

[25] J. Heise. Rope Status. SNO+ Internal Document 181-v1, August 2008.

[26] J. Argyriades et al. (The NEMO Collaboration). Measurement of the Double Beta Decay Half-life of ^{150}Nd and Search for Neutrinoless Decay Modes with the NEMO-3 Detector. *Phys. Rev. C*, 80:032501, 2009.

[27] M. Chen. LAB Scintillator. SNO+ Internal Document 11-v1, May 2007.

[28] S. Hans and M. Yeh. SNO+ Neodymium-loaded LAB. SNO+ Internal Document 475-v1, May 2010.

[29] G. Horton-Smith. Introduction to GLG4sim. Available online at http://neutrino.phys.ksu.edu/∼GLG4sim/, May 2006.

[30] J.R. Wilson. Implementing Optics Constants in RAT. SNO+ Internal Document 269-v1, March 2009.

[31] A. Wright. The Scintillation and Optical Properties of Linear Alkylbenzene. SNO+ Internal Document 219-v1, September 2008.

[32] X. Dai V. Novikov and A. Wright. private communication.

[33] Q.R. Ahmad. *Muon Correlated Background at The Sudbury Neutrino Observatory.* PhD thesis, Brown University, 2002.

[34] H.M. OKeeffe. *Low Energy Background in the NCD phase of the Sudbury Neutrino Observatory.* PhD thesis, University of Oxford, 2008.

[35] M. Chen. private communication.

[36] A. Wright. private communication.

[37] J.R. Wilson and H.M. O'Keeffe. private communication.

[38] H.M. O'Keeffe. private communication.

[39] J.R. Wilson. private communication.

[40] H.M. O'Keeffe. Analysis of the Scintillator Bucket Data. SNO+ Internal Document 306-v1, April 2009.

[41] B.T. Cleveland. private communication.

Appendix A

Run List

Run #	Date	Start Time	Live Time [s]	working PMTs #
70281	9/30/2008	2:29:49	3667	7031
70282	9/30/2008	3:30:57	3689	7031
70283	9/30/2008	4:32:27	3617	7031
70284	9/30/2008	5:32:45	3833	7031
70285	9/30/2008	6:36:38	3897	7031
70286	9/30/2008	7:41:35	3693	7031
70287	9/30/2008	8:43:09	3665	7031
70288	9/30/2008	9:44:14	3611	7031
70289	9/30/2008	10:44:26	3606	7031
70307	9/30/2008	13:41:32	1803	7001
70314	9/30/2008	14:21:37	2029	7001
70324	9/30/2008	19:12:35	3610	6949
70330	9/30/2008	22:13:24	3694	6919
70334	10/01/2008	0:28:01	3604	6892
70335	10/01/2008	1:28:06	3603	6892
70341	10/01/2008	4:06:09	3787	6824
70342	10/01/2008	5:09:47	3638	6824
70343	10/01/2008	6:10:56	3710	6824
70344	10/01/2008	7:13:16	3804	6824
70345	10/01/2008	8:17:11	3933	6824

continued on next page

continued from previous page

Run #	Date	Start Time	Live Time[s]	working PMTs #
70346	10/01/2008	9:23:14	3873	6824
70347	10/01/2008	10:28:18	3680	6824
70348	10/01/2008	11:30:08	3618	6824
70349	10/01/2008	12:30:57	3606	6824
70351	10/01/2008	13:37:37	3606	6817
70358	10/01/2008	14:59:01	3294	6817
70360	10/01/2008	16:03:59	3607	6809
70362	10/01/2008	17:15:21	3722	6861
70363	10/01/2008	18:17:25	2974	6861
70365	10/01/2008	19:09:12	2998	6861
70367	10/01/2008	21:11:48	3648	6861
70372	10/01/2008	23:18:08	3743	6855
70373	10/02/2008	0:20:33	3648	6855
70374	10/02/2008	1:21:21	3806	6855
70375	10/02/2008	2:24:48	3614	6855
70376	10/02/2008	3:25:03	3604	6855
70377	10/02/2008	4:25:09	3604	6855
70378	10/02/2008	5:25:14	3664	6855
70379	10/02/2008	6:26:19	3701	6855
70380	10/02/2008	7:28:01	3607	6855
70383	10/02/2008	10:06:56	3608	6823
70384	10/02/2008	11:07:06	3606	6823
70385	10/02/2008	12:07:13	3614	6823
70386	10/02/2008	13:07:28	3604	6823
70388	10/02/2008	14:22:42	3614	6823
70389	10/02/2008	15:22:58	3610	6823
70391	10/02/2008	16:27:32	4447	6823
70392	10/02/2008	17:41:40	3609	6823
70393	10/02/2008	18:41:50	3651	6823
70394	10/02/2008	19:42:43	3750	6823
70395	10/02/2008	20:45:13	3690	6823
70396	10/02/2008	21:46:44	3722	6823
70397	10/02/2008	22:48:48	3605	6823
70398	10/02/2008	23:48:53	3602	6823
70402	10/03/2008	1:43:52	3653	6816

continued on next page

continued from previous page

Run #	Date	Start Time	Live Time[s]	working PMTs #
70408	10/03/2008	3:23:48	3606	6809
70409	10/03/2008	4:23:55	3622	6809
70424	10/03/2008	7:12:24	3607	6698
70425	10/03/2008	8:12:32	4108	6698
70430	10/03/2008	11:37:56	92	6698
70437	10/03/2008	11:54:42	3619	6698
70438	10/03/2008	12:55:03	6072	6698
70440	10/03/2008	15:06:19	3602	6678
70443	10/03/2008	17:11:58	3603	6628
70445	10/03/2008	19:28:40	3677	6628
70446	10/03/2008	20:29:59	3626	6628
70476	10/06/2008	0:52:33	3607	6499
70477	10/06/2008	1:52:42	3603	6499
70478	10/06/2008	2:52:46	3602	6499
70479	10/06/2008	3:52:50	3780	6499
70480	10/06/2008	4:55:52	3603	6499
70481	10/06/2008	5:55:57	3619	6499
70482	10/06/2008	6:56:18	3615	6499
70483	10/06/2008	7:56:35	3615	6499
70484	10/06/2008	8:56:52	3776	6499
70488	10/06/2008	10:27:17	3645	6472
70489	10/06/2008	11:28:03	3663	6472
70490	10/06/2008	12:29:09	3610	6472
70497	10/06/2008	15:11:51	3670	6449
70499	10/06/2008	16:25:21	4044	6442
70500	10/06/2008	17:32:46	3605	6442
70503	10/06/2008	19:25:24	3729	6411
70504	10/06/2008	20:27:36	4588	6411
70505	10/06/2008	21:44:07	1355	6411
70507	10/06/2008	22:12:19	2351	6411
70511	10/07/2008	0:49:50	3402	6381
70512	10/07/2008	1:46:34	3989	6381
70513	10/07/2008	2:53:05	3915	6381
70514	10/07/2008	3:58:23	3402	6381
70515	10/07/2008	4:55:06	3396	6381

continued on next page

continued from previous page

Run #	Date	Start Time	Live Time[s]	working PMTs #
70516	10/07/2008	5:51:44	3430	6381
70517	10/07/2008	6:48:57	3635	6381
70520	10/07/2008	8:18:20	3635	6381
70526	10/07/2008	11:10:16	3604	6373
70527	10/07/2008	12:10:22	3374	6373
70539	10/07/2008	15:47:21	3416	6373
70541	10/07/2008	16:50:35	3664	6373
70543	10/07/2008	17:58:09	3963	6373
70548	10/07/2008	21:03:37	3674	6373
70549	10/07/2008	22:04:53	3740	6373
70550	10/07/2008	23:07:13	3661	6373
70551	10/08/2008	0:08:15	3648	6373
70552	10/08/2008	1:09:04	3722	6373
70553	10/08/2008	2:11:07	3614	6373
70557	10/08/2008	5:07:49	3642	6365
70558	10/08/2008	6:08:32	3609	6365
70559	10/08/2008	7:08:41	3663	6365
70560	10/08/2008	8:09:45	4594	6365
70561	10/08/2008	9:26:20	3759	6365
70562	10/08/2008	10:29:00	3794	6365
70563	10/08/2008	11:32:14	3604	6365
70564	10/08/2008	12:32:20	2135	6365
70566	10/08/2008	13:13:09	3767	6365
70568	10/08/2008	14:19:44	3630	6365
70570	10/08/2008	15:23:49	3733	6365
70574	10/08/2008	17:12:55	3603	6336
70576	10/08/2008	18:18:05	3616	6336
70578	10/08/2008	19:22:26	3875	6336
70579	10/08/2008	20:27:02	3636	6336
70580	10/08/2008	21:27:39	3604	6336
70581	10/08/2008	22:27:43	3604	6336
70582	10/08/2008	23:27:48	3738	6336
70583	10/09/2008	0:30:07	3617	6336
70584	10/09/2008	1:30:25	4268	6336
70585	10/09/2008	2:41:34	3761	6336

continued on next page

continued from previous page

Run #	Date	Start Time	Live Time[s]	working PMTs #
70586	10/09/2008	3:44:16	3845	6336
70587	10/09/2008	4:48:22	4033	6336
70588	10/09/2008	5:55:36	3604	6336
70589	10/09/2008	6:55:41	3643	6336
70590	10/09/2008	7:56:25	3610	6336
70591	10/09/2008	8:56:36	3650	6336
70592	10/09/2008	9:57:27	3616	6336
70593	10/09/2008	10:57:43	3608	6336
70594	10/09/2008	11:57:53	3648	6336
70595	10/09/2008	12:58:41	814	6336
70601	10/09/2008	15:14:19	2571	6309
70605	10/09/2008	16:17:43	2850	6309
70608	10/09/2008	17:21:04	3608	6309
70609	10/09/2008	18:21:14	3971	6309
70610	10/09/2008	19:27:27	3605	6309
70611	10/09/2008	20:27:34	3601	6309
70612	10/09/2008	21:27:37	3602	6309
70631	10/10/2008	2:47:35	3601	6309
70632	10/10/2008	3:47:38	3437	6309
70634	10/10/2008	5:47:40	3589	6309
70635	10/10/2008	6:47:31	3472	6309
70636	10/10/2008	7:48:17	3510	6309
70637	10/10/2008	8:46:49	3556	6309
70639	10/10/2008	10:44:11	3554	6309
70640	10/10/2008	11:43:28	3442	6309
70641	10/10/2008	12:40:52	1485	6309
70648	10/10/2008	13:46:41	4450	6309
70649	10/10/2008	15:01:43	4091	6309
70650	10/10/2008	16:10:43	3657	6309
70651	10/10/2008	17:12:29	3741	6309
70652	10/10/2008	18:16:02	3649	6309
70656	10/10/2008	21:02:35	3952	6309
70657	10/10/2008	22:08:58	3535	6309
70659	10/10/2008	23:20:40	5234	6309
70660	10/11/2008	0:54:07	8546	6309

continued on next page

continued from previous page

Run #	Date	Start Time	Live Time[s]	working PMTs #
70661	10/11/2008	3:16:35	2692	6309
70665	10/11/2008	4:46:59	3401	6309
70666	10/11/2008	5:43:42	3425	6309
70667	10/11/2008	6:40:49	3739	6309
70668	10/11/2008	7:43:10	3511	6309
70669	10/11/2008	8:41:43	3622	6309
70670	10/11/2008	9:42:08	3430	6309
70671	10/11/2008	10:39:20	3490	6309
70672	10/11/2008	11:37:33	3464	6309
70673	10/11/2008	12:35:19	3712	6309
70674	10/11/2008	13:37:14	3618	6309
70675	10/11/2008	14:37:35	3644	6309
70676	10/11/2008	15:38:21	3608	6309
70679	10/11/2008	17:20:28	3606	6295
70680	10/11/2008	18:20:37	3903	6295
70681	10/11/2008	19:26:36	3603	6295
70682	10/11/2008	20:26:41	3889	6295
70683	10/11/2008	21:31:33	3323	6295
70688	10/12/2008	1:18:32	4331	6289
70689	10/12/2008	2:30:46	3508	6289
70690	10/12/2008	3:29:16	3506	6289
70691	10/12/2008	4:27:45	3511	6289
70692	10/12/2008	5:26:19	3405	6289
70693	10/12/2008	6:23:06	3460	6289
70694	10/12/2008	7:20:49	4159	6289
70695	10/12/2008	8:30:10	3615	6289
70696	10/12/2008	9:30:27	3558	6289
70697	10/12/2008	10:29:47	3533	6289
70698	10/12/2008	11:28:43	3502	6289
70699	10/12/2008	12:27:08	2876	6289
70701	10/12/2008	13:32:05	3602	6283
70702	10/12/2008	14:32:09	3669	6283
70704	10/12/2008	16:33:27	3615	6283
70709	10/12/2008	17:59:55	3636	6283
70710	10/12/2008	19:00:34	3607	6283

continued on next page

continued from previous page

Run #	Date	Start Time	Live Time[s]	working PMTs #
70711	10/12/2008	20:00:43	3608	6283
70712	10/12/2008	21:00:54	3624	6283
70713	10/12/2008	22:01:20	3723	6283
70714	10/12/2008	23:03:26	3602	6283
70715	10/13/2008	0:03:30	3315	6283
70716	10/13/2008	0:58:47	3543	6283
70717	10/13/2008	1:57:53	3548	6283
70718	10/13/2008	2:57:03	3599	6283
70719	10/13/2008	3:57:04	3610	6283
70720	10/13/2008	4:57:16	3640	6283
70721	10/13/2008	5:57:58	2586	6283
70723	10/13/2008	7:01:56	3747	6278
70724	10/13/2008	8:04:25	3708	6278
70725	10/13/2008	9:06:16	3627	6278
70726	10/13/2008	10:06:44	3604	6278
70727	10/13/2008	11:06:51	3832	6278
70728	10/13/2008	12:10:45	3605	6278
70738	10/13/2008	18:06:54	3827	6258
70739	10/13/2008	19:11:11	3769	6258
70740	10/13/2008	20:14:02	3610	6258
70741	10/13/2008	21:14:13	3733	6258
70743	10/13/2008	22:52:23	3650	6258
70744	10/13/2008	23:53:15	1002	6258
70745	10/14/2008	0:12:18	3748	6258
70746	10/14/2008	1:14:47	3683	6258
70747	10/14/2008	2:16:11	3746	6258
70748	10/14/2008	3:18:39	3610	6258
70749	10/14/2008	4:18:50	3604	6258
70750	10/14/2008	5:18:55	3712	6258
70751	10/14/2008	6:20:48	3605	6258
70752	10/14/2008	7:20:54	4271	6258
70753	10/14/2008	8:32:07	3676	6258
70771	10/14/2008	16:39:20	3669	6227
70772	10/14/2008	17:40:32	3608	6227
70773	10/14/2008	18:40:42	3665	6227

continued on next page

continued from previous page

Run #	Date	Start Time	Live Time[s]	working PMTs #
70774	10/14/2008	19:41:50	3618	6227
70775	10/14/2008	20:42:10	3616	6227
70776	10/14/2008	21:42:28	3698	6227
70777	10/14/2008	22:44:08	3614	6227
70778	10/14/2008	23:44:24	3647	6227
70779	10/15/2008	0:45:13	3637	6227
70780	10/15/2008	1:45:52	3623	6227
70821	10/15/2008	19:40:49	3628	6163
70822	10/15/2008	20:41:19	4831	6163
70826	10/15/2008	23:02:21	2587	6163
70834	10/16/2008	3:32:09	3691	6120
70835	10/16/2008	4:33:42	3634	6120
70836	10/16/2008	5:34:17	3852	6120
70837	10/16/2008	6:38:32	2180	6120
70839	10/16/2008	7:25:49	3714	6112
70840	10/16/2008	8:27:46	3703	6112
70841	10/16/2008	9:29:31	3660	6112
70842	10/16/2008	10:30:33	3703	6112
70843	10/16/2008	11:32:18	3726	6112
70844	10/16/2008	12:34:26	3639	6112
70845	10/16/2008	13:35:07	1025	6112
70864	10/16/2008	19:50:27	3608	6089
70865	10/16/2008	20:50:36	4079	6089
70866	10/16/2008	21:58:36	3795	6089
70867	10/16/2008	23:01:53	3431	6089
70868	10/16/2008	23:59:05	4267	6089
70869	10/17/2008	1:10:13	4113	6089
70871	10/17/2008	3:30:30	3604	6089
70872	10/17/2008	4:30:36	3614	6089
70873	10/17/2008	5:30:51	3605	6089
70874	10/17/2008	6:30:58	3604	6089
70877	10/17/2008	8:31:44	3606	6059
70878	10/17/2008	9:31:52	3605	6059
70879	10/17/2008	10:32:00	3611	6059
70883	10/17/2008	12:47:20	3612	6033

continued on next page

continued from previous page

Run #	Date	Start Time	Live Time[s]	working PMTs #
70884	10/17/2008	13:47:34	3691	6033
70885	10/17/2008	14:49:07	3607	6033
70886	10/17/2008	15:49:16	4274	6033
70893	10/17/2008	18:17:15	3630	6018
70894	10/17/2008	19:17:48	3742	6018
70899	10/18/2008	12:15:06	3601	6018
70900	10/18/2008	13:15:08	3623	6018
70901	10/18/2008	14:15:33	3603	6018
70902	10/18/2008	15:15:39	3670	6018
70905	10/18/2008	17:08:59	3930	6018
70906	10/18/2008	18:14:31	3604	6018
70907	10/18/2008	19:14:37	3619	6018
70908	10/18/2008	20:14:58	3609	6018
70909	10/18/2008	21:15:10	3626	6018
70910	10/18/2008	22:28:04	4259	6018
70914	10/19/2008	0:26:40	4561	6001
70915	10/19/2008	1:43:13	3658	6001
70916	10/19/2008	2:44:13	2962	6001
70917	10/19/2008	3:41:56	3565	6001
70918	10/19/2008	4:41:23	3523	6001
70919	10/19/2008	5:40:08	3521	6001
70920	10/19/2008	6:38:52	3683	6001
70921	10/19/2008	7:40:18	3472	6001
70922	10/19/2008	8:38:12	4034	6001
70923	10/19/2008	9:45:29	3365	6001
70924	10/19/2008	10:41:36	3463	6001
70925	10/19/2008	11:39:21	3564	6001

Table A.1: The start date, time (UTC time), real running time (live time) and the number of working PMTs for each run.

Appendix B

List of Acronyms

AV: Acrylic Vessel

DAMN: Data Analysis Mask Number, SNO data cleaning cuts

LAB: Linear Alkylbenzene, the solvent of the liquid scintillator

MC: Monte Carlo simulated

Ncor: Nhits after corrections

Nhits: Number of phototubes hit in a single event

PMNS: Pontecorvo−Maki−Nakagawa−Sakata matrix

PPO: 2,5-diphenyloxazole, the fluor of the liquid scintillator

PGT: Pulsed Global Trigger

PMT: Photomultiplier tube

PSUP: PMT support structure

RAT: Reactor Analysis Tools, SNO+ Monte Carlo and analysis code

SNO: The Sudbury Neutrino Observatory

SNO+: Follow-up experiment to SNO

SNOMAN: SNO Monte Carlo and Analysis Code